ELECTRON BRAGG REFLECTOR LASERS

Electron Bragg Reflectors for Improved Temperature Stability of InGaAsP Quantum Well Lasers

by

David Michael Adams, B. Sc.

A Thesis Submitted to the School of Graduate Studies

In Partial Fulfillment of the Requirements for the Degree

Master of Engineering

McMaster University

Master of Engineering (1993)   McMaster University
Engineering Physics   Hamilton, Ontario

TITLE: Electron Bragg Reflectors for Improved Temperature Stability
            of InGaAsP Quantum Well Lasers.

AUTHOR: David Michael Adams, B. Sc. (University of Waterloo).

SUPERVISOR: Professor John G. Simmons

NUMBER OF PAGES: xiv, 115

Abstract

This thesis describes the incorporation within a semiconductor laser of a multiple quantum well InGaAsP/InP Electron Bragg Reflector (EBR). The EBR is intended to improve laser performance by inhibiting the escape of hot electrons from the laser active region by quantum mechanical Bragg reflection. To the author's knowledge, this investigation represents the first attempt to realize an EBR in the InGaAsP/InP material system.

Computer models based on a transfer matrix method for the solution of Schrödinger's equation were written to obtain the EBR design. The transfer matrix method is described. Extensions to the transfer matrix method for optics are presented and are demonstrated to provide more than an order of magnitude improvement in computational efficiency for the calculation of the complex TE-mode propagation constant for planar graded-index waveguides with absorption or gain.

The EBR designed for this work incorporates several new features. Deleterious band bending in the vicinity of the EBR is minimized by exploiting material strain to reduce the density of hole states in the EBR quantum wells. To maximize reflection bandwidth and relax fabrication tolerances, the EBR design used well widths that decreased with increasing depth into the p-type InP cladding. By the placement of the EBR adjacent to the separate confinement region, a return path was provided for electrons that scattered inelastically within the EBR. Moreover, the EBR structure

was designed to support no bound electron states, so that the recombination of electrons with holes in the EBR would be minimal. To the author's knowledge, the EBR-equipped laser fabricated for this work represents the first attempt to exploit electron state exclusion.

To explore the effectiveness of EBRs in the InGaAsP/InP material system, two nearly identical ridge waveguide lasers (one with an EBR, and one without) were designed, fabricated, and tested. The EBR-equipped lasers exhibited an anomalous threshold current temperature dependence which featured a "negative-T_0" regime (in which the threshold current *decreases* with increasing temperature), attaining a minimum in threshold current between T=150 K and T=200 K. These lasers had a threshold current temperature stability superior to that of standard lasers within a ~70 K window around the minimum threshold temperature.

Experimental evidence suggests that the improved stability is not due to quantum mechanical Bragg reflection provided by the EBR, but is attributable to the temperature-dependent rate of hole escape from the EBR quantum wells into the separate confinement region. The proposed mechanism is described in detail and is supported by theoretical and experimental evidence. The results have implications for device design, because the mechanism by which the superior temperature stability is achieved does not rely on the electron coherence effects; the mathematical model suggests that the mechanism can be exploited to provide superior temperature stability in semiconductor lasers at 300 K or above.

Acknowledgments

Table of Contents

List of Figures

List of Tables

Chapter 1: Introduction

1.1 Background

Remotely deployed repeater stations and customer access nodes for terrestrial fiber-optic telecommunication networks require light sources that operate efficiently and reliably in ambients ranging from -40°C to +85°C [Bellcore Technical Note, 1991; Anderson, 1993]. Over this operational temperature range, the InGaAsP/InP lasers developed to exploit fiber dispersion or attenuation minima exhibit a large variation of the threshold current, emission wavelength, and radiative efficiency [Agrawal *et al.*, p. 128, 1986]. The temperature sensitivity of these laser characteristics incurs performance limitations and imposes costly demands on both the driving circuitry for the laser and the compensating electronics in the detection process.

In conventional double-heterostructure (DH) lasers, the temperature sensitivity has been primarily attributed to non-radiative Auger recombination [Haug, 1985], to optical intervalence band absorption losses [Asada *et al.*, 1983], and to the leakage of electrons or holes from the active region to the surrounding (cladding) regions. The leakage is typically dominated by thermionic emission [Chiu *et al.*, 1983] and the diffusion of Auger-recombination-induced energetic carriers [Chik, 1988].

Reductions in temperature sensitivity have been predicted and confirmed for semiconductor lasers in which the band structure of the active region is modified through quantum confinement [Rezek et al., 1977] or strain [Evans et al., 1992; Thijs et al., 1990]. However, there have been few device architectures explicitly proposed to achieve superior temperature stability by reducing leakage currents.

Anthony et al. [1983] observed an enhanced temperature stability for standard DH AlGaAs/GaAs lasers which they attributed to a thermally assisted electron diffusion from the p-n junction, which was accidentally located ~1000 Å into the n-type cladding region. Macieko et al. [1991] proposed and successfully demonstrated [Beckett et al., 1992] a double active region InGaAsP/InP type laser structure in which the second active region recovered leakage current from the first. Recently, improvements in temperature stability achieved by Itaya et al. [1993] for a laser with a GaAs active region clad by wide band gap $In_{.5}(Ga_{.3}Al_{.7})_{.5}P$ layers were attributed to a reduction in electron leakage.

K. Iga suggested [1986] and later confirmed [Takagi et al, 1991] that leakage could be inhibited using quantum mechanical reflection by the incorporation of an electron Bragg reflector (EBR) adjacent to the active region. EBR's have been included in orange-red InGaAlP-based laser diodes, where the problem of electron leakage is exacerbated by relatively shallow heterojunction conduction band discontinuities. Recent comparative studies reveal that visible lasers with an EBR can attain a higher maximum operating temperature [Hamada et al., 1993; Shono et al., 1993; Rennie et al., 1993], and show a reduction in the magnitude [Rennie et al., 1993; Kishino et al., 1991] and temperature dependence [Rennie et al., 1992] of the threshold current.

1.2 Electron Bragg Reflectors

The EBR proposed by Iga operates by the principle of quantum mechanical reflection. An electron in the active region which is traveling toward a homogeneous cladding region with kinetic energy *exceeding* the potential barrier has finite probability of being reflected. This phenomenon is analogous to the partial reflection of light upon encountering a step in the refractive index. Now, the reflectivity is greatly enhanced when light encounters a Bragg mirror, which consists of a stack of alternating high and low index quarter-wavelength dielectric layers. Similarly, the probability of reflection of an *electron* will be greatly enhanced if it strikes an electron Bragg reflector comprising a stack of quantum wells and barriers with thicknesses equal to $\lambda_b/4$, where λ_b is the wavelength of the electron wavefunction envelope. The EBR can be highly reflective (R>95%) for electrons incident within a broad (100+ meV) range of energies. The operating principle of an EBR is compared to that of an optical Bragg mirror in Fig. 1.1.

The EBR belongs to an emerging class of exploratory devices which exploit the wave nature of conduction electrons. These devices are generally based on optical components, and correspondingly they aim to reflect, refract, diffract, transmit, interfere, or guide electrons in a manner analogous to optical waves. Examples of proposed electron-wave devices based on existing optical components include waveguides [Wang *et al.*, 1991; Gaylord *et al.*, 1989], narrow pass filters [Glytsis *et al.*, 1989], anti-reflection coatings [Gaylord *et al.*, 1990], directional couplers [Del Alamo *et al.*, 1990], and Fabry-Perot interferometers [Potter *et al.*, 1988]. Experiments are typically conducted at, or between, liquid helium and liquid nitrogen

a) Optical Bragg reflector

λ

ΔλΔ

photon

R

$\lambda/(4\,n_{high})$ ⟶ ⟵ $\lambda/(4\,n_{low})$

b) Electron Bragg reflector

E

ΔE

electron

V

Conduction Band

Laser active area

Electron Bragg reflector

Cladding region
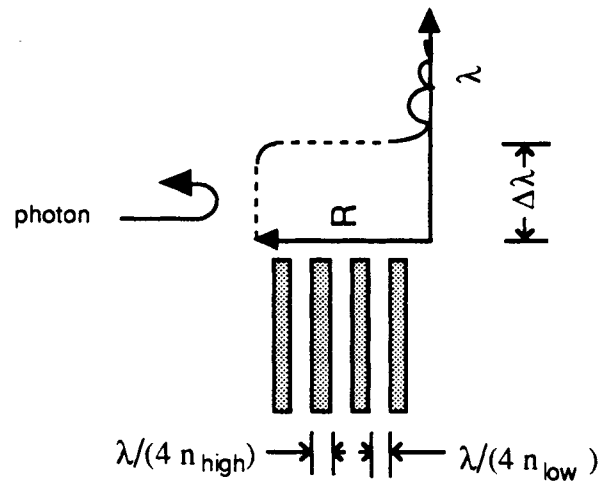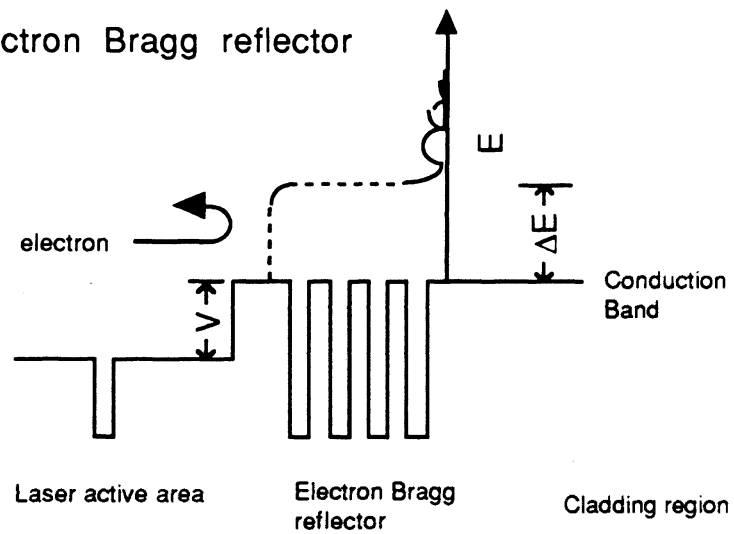
Figure 1.1: Comparison of (a) an optical Bragg reflector and (b) electron Bragg reflector. Both devices consist of a grating of quarter-wave-thick layers. The EBR reflects hot electrons which would normally escape from the active region whose energy lies between V and V+ΔE, where ΔE is the EBR bandwidth.

temperatures [e.g. Tsubaki *et al.*, 1988; Hayes *et al.*, 1988, Levi *et al.*, 1985], where phonon freeze-out enables a measurable fraction of the electron current to interact coherently[1] with the structure. Even at low temperatures, the theoretical performance of most electron-wave devices is very sensitive uncertainties among the key material parameters (e.g. band offsets and effective masses).

In contrast, the EBR is a broadband mirror whose bandwidth and peak reflectivity are tolerant to systematic and random fabrication errors and uncertainties (see § 4.4). The tolerance to fabrication flaws suggests that EBR reflection properties may also be tolerant to *intrinsic* structural perturbations, such as band deformations accompanying the passage of acoustic phonons [Wang, p. 217, 1989]. The robustness of EBRs is supported by compelling evidence confirming their effectiveness at room temperature [Capasso *et al.*, 1992], which is independent of the observed improvements in the performance of visible lasers noted in § 1.1.

Capasso *et al.* [*ibid.*] demonstrated room temperature operation of EBRs with the $InGa_{.47}As_{.53}/Al_{.48}In_{.52}As$ structure illustrated in Fig. 1.2(b). The central 32 Å n-doped (10^{18} cm^3) InGaAs well supports only a single bound mode. However, the reflection provided by the six-period Bragg mirror (each period consisting of 16 Å InGaAs well/39 Å AlInAs barrier) on both sides of the 32 Å well was sufficient to establish a confined electron state at an energy *above* the cladding band edge. The existence of the state was confirmed by room temperature optical absorption experiments. The width, ΔE, of the absorption energy resonance corresponding to the transition from the bound to the suspended state was 17.5 meV, which is

---

[1] Coherent electron transport occurs in the absence of inelastic (i.e. wavelength altering) collisions

a) Conventional intraband absorption

Absorption

ΔE_1

E_1

E_1

Photon
Energy
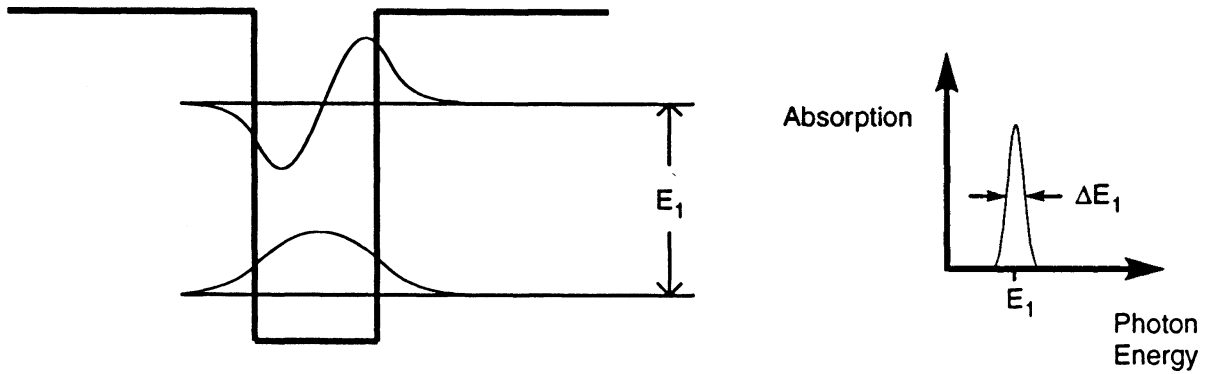
b) Intraband absorption from a confined state to a suspended state

E_2

Absorption

ΔE_2

E_2

Photon
Energy

E

x
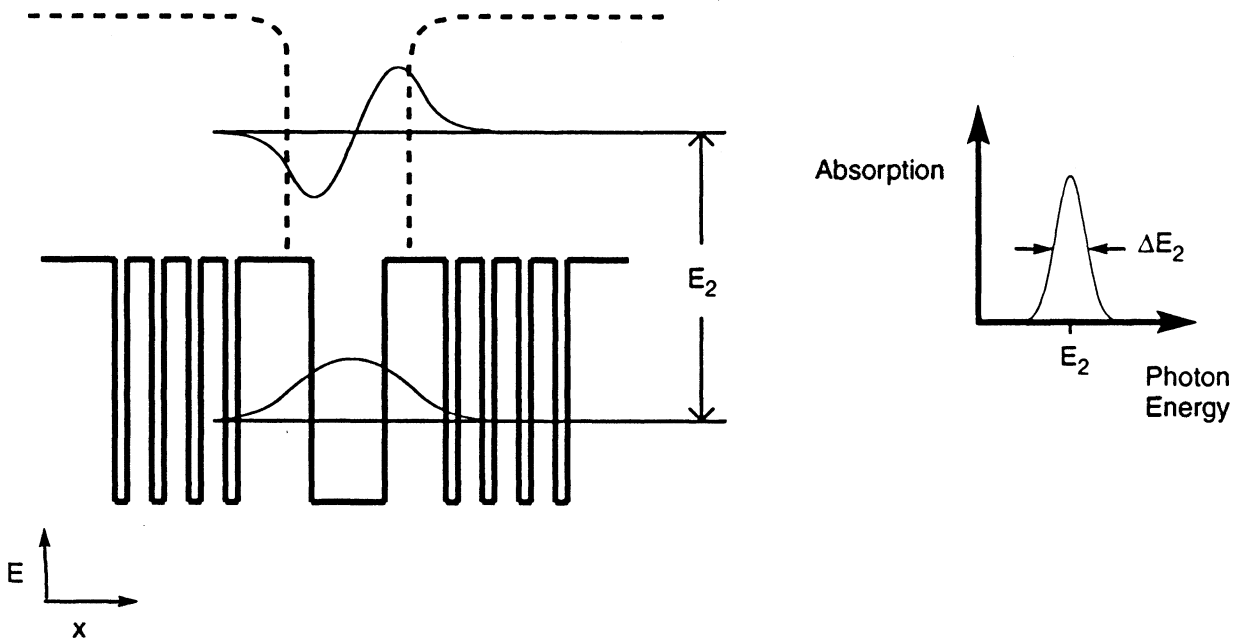
Figure 1.2: Detection of "suspended" electron state by optical absorption measurement. (a) Conventional intraband absorption transition and corresponding spectrum. (b) Absorption transition to a state lying beyond the cladding band edge. The absorption spectra are nearly identical; however, for case (b) the width of the energy resonance is broadened slightly due to the finite lifetime for *lateral* ($\pm x$) escape of the electron.

virtually identical to the width of bound-state to bound-state transitions in a comparably doped 55 Å well [*ibid.*]. The comparable ΔE value suggests there is very little broadening of the absorption resonance due to electron escape from the Bragg confined state, confirming that electron Bragg reflectors can be effective at room temperature.

The success of Bragg reflector structures in AlGaAs/GaAs, and InGaAlP material systems would be expected to motivate research into other alloy systems. Despite the troublesome temperature sensitivity of 1.31 and 1.55 μm wavelength lasers, an experimental investigation of an EBR in the InGaAsP/InP material system has not yet been reported.

1.3 Thesis Objective and Outline

This thesis describes the design and experimental verification of a novel InGaAsP/InP superlattice EBR which is intended to improve laser performance (e.g. though a reduction in threshold current, increased efficiency, and increased maximum temperature of operation) by inhibiting the escape of hot electrons from the active region. To explore the advantages afforded by an EBR, two single quantum-well ridge-waveguide lasers (one with an EBR, and one without) were designed, fabricated, and tested. The goal is to establish the usefulness of EBR's in this material system, and to identify design parameters and any novel features which may be expected to yield optimal current confinement.

In Chapter 2, the dominant physical processes accounting for the temperature dependence of the leakage current in typical InGaAsP/InP semiconductor lasers are identified, and the link between leakage and the temperature dependence of laser performance is established.

In Chapter 3, two versatile transfer matrix methods (TMM) are developed for the analysis of i) optical and, ii) electronic waves in planar layered media. Transfer matrices are derived for application of the optical TMM to lossless or absorbing graded index waveguides which are described by piece-wise linear, parabolic, or exponential variations in the dielectric constant. The TMM for electron waves is used to design the novel InGaAsP/InP EBR which is described in detail in Chapter 4.

Chapter 5 outlines the fabrication of the EBR-equipped and the normal (control group) single quantum well lasers. The experimental apparatus and procedures employed to test these lasers are described in Chapter 6.

The experiments revealed an anomalous threshold current temperature dependence for EBR-equipped lasers, which included a 70 K window where the threshold current temperature stability was superior to that of the control lasers. The experiments also revealed an unusual evolution of the differential quantum efficiency with injection current for EBR-equipped lasers at low temperatures. In Chapter 7, the experimental results are collectively interpreted with a new theoretical model.

Chapter 8 contains a summary and conclusions.

Chapter 2: Current Leakage and the Temperature Dependence of InGaAsP Lasers

2.1 Introduction

This chapter identifies the link between current leakage and the temperature dependence of the performance of InGaAsP/InP semiconductor lasers. The leakage is assumed to be dominated by the diffusion of Auger recombination induced energetic carriers (§ 2.3) and thermionic emission (§ 2.4). Implications relevant to the design of the EBR are stated.

2.2 Electronic Operation of a Quantum Well laser

The electronic operation of a basic single quantum well laser is summarized in Fig. 2.1, which shows a 1-D band diagram of the active area under forward bias. Electrons and holes are injected from the n- and p-doped cladding regions into a separate confinement region, where they can eventually relax into the active region and recombine by stimulated emission. Although charge neutrality is satisfied overall, the carriers exceed their equilibrium densities. As a result, their distributions are determined by individual electron and hole quasi-Fermi levels situated near the conduction and valence band edges, respectively. Ideally, all of the injected (excess) carriers would remain within the separate confinement or active region;

however, leakage into the cladding regions can occur when carriers possess kinetic energies exceeding the heterojunction potential barriers.

There are two main processes by which a carrier can acquire kinetic energy sufficient for leakage, namely: phonon absorption, which drives thermionic emission; and Auger recombination, by which a carrier acquires energy released by the recombination of an electron-hole pair.
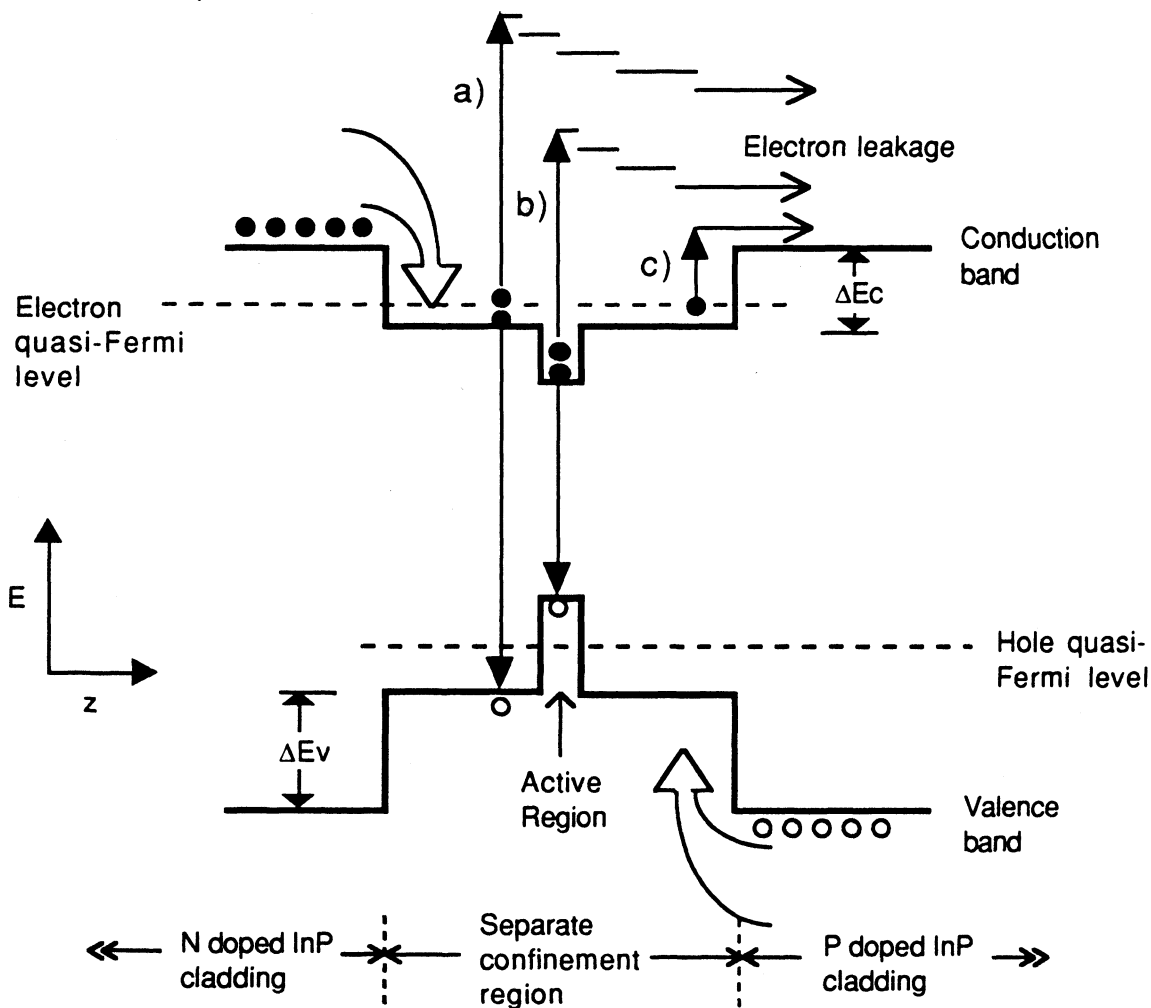
Figure 2.1: Basic operation of a single quantum well laser, showing the leakage into the p-doped cladding region of energetic carriers generated by Auger recombination in (a) the separate confinement region and (b) the active region. Leakage is also attributable to (c) thermionic emission.

Electrons (holes) which leak into the p-doped (n-doped) cladding region are minority carriers there. Although a fraction of these carriers diffuse back into the confinement region, the remainder are lost due to recombination with majority carriers as they diffuse into the cladding toward the carrier sink at the metal contact.

2.3 Auger-Recombination-Induced Carrier Leakages

In an Auger recombination process, the energy released by the non-radiative recombination of an electron with a hole is transferred to a third particle, which is itself either an electron or a hole. The initial state of each particle involved may be in a band or in a localized state lying near a band edge [e.g. see Pankove, p. 161, 1971]. As an example, Figure 2.2(a) represents a three-particle Auger process in which the recombination of a conduction band electron with a heavy hole results in excitation of a second conduction band electron. Both energy and momentum are conserved. Figure 2.2(b) illustrates an example of phonon-assisted Auger recombination. Phonon-assisted Auger processes include phonon absorption or emission from one of the particles to satisfy momentum conservation. However, the interaction with a fourth particle results in a substantial reduction in the probability of occurrence for this process when compared to three-particle Auger processes.

A carrier excited by an Auger recombination acquires an excess kinetic energy which is comparable to the band-gap energy. It is expected to expend most of its excess energy by the emission of longitudinal optical (LO) phonons [Takeda *et al.*, 1982]. The rate at which an energetic carrier relaxes by LO phonon emission in InGaAsP of a given composition can be estimated from the appropriate weighted average of the rates in the constituent binaries.

a)

Conduction
Band

Δk_1

Energetic
Electron

ΔE_1

ΔE_2

Heavy
Hole
Band

Δk_2

E

k

Light
Hole
Band

$\Delta k_1 = \Delta k_2$
$\Delta E_1 = \Delta E_2$

b)

Conduction
Band

Δk_1

Energetic
Electron

ΔE_1

ΔE_2

Heavy
Hole
Band

ΔE_3

Δk_3 Δk_2

E

k

Light
Hole
Band

$\Delta k_1 = \Delta k_2 + \Delta k_3$
$\Delta E_1 = \Delta E_2 + \Delta E_3$
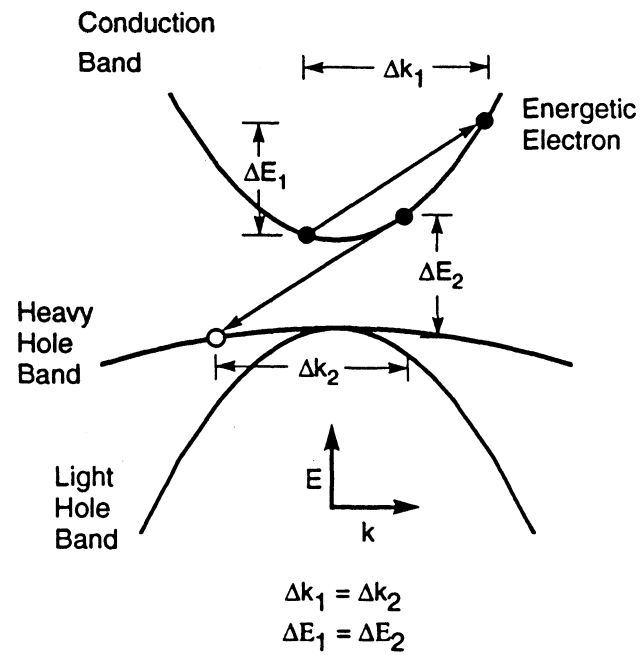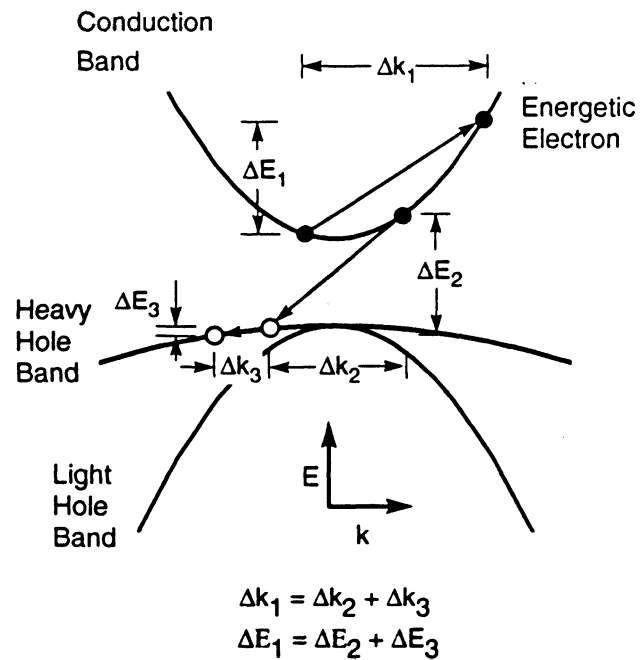
Figure 2.2: E vs. k representation of (a) direct and (b) phonon-assisted Auger recombination processes. Note that the phonon in (b) serves to satisfy both energy and momentum conservation. (In these diagrams, the split-off band has been omitted for simplicity).

In Chik's investigation of Auger-recombination-induced energetic carrier leakage, the excited carrier is ascribed an effective lifetime, τ_{ex}, which corresponds to the time during which its energy is sufficient for escape into the cladding. Only those excited carriers situated within an effective diffusion length, $L_{ex} = \sqrt{D\,\tau_{ex}}$, of the cladding are expected to leak out. Under the assumption that the leakage of energetic carriers is accomplished entirely by diffusion (i.e. neglecting any drift component), the net Auger induced leakage current density from a layer of width d is given by [Chik, 1988]:

$$J_{Auger} = \frac{q\,D\,\tau_{ex}\,L_{ex}\,tanh[\;d/L_{ex}\;]\,(\;C\;+C_{ph})\;(\;n\;+\;n_d)^{\alpha}\,p^{\,\beta}}{D\,\tau_{ex}\;+\;L_{ex}\,tanh[\;d/L_{ex}\;]\,L\,tanh[\;W/L\;]} \qquad (2.1)$$

In Eq. (2.1): q is the electronic charge; W is the distance from the heterojunction interface to the metal contact layer; D, L, and m^* are the minority carrier diffusivity, diffusion length, and effective mass in the cladding; C and C_{ph} are the coefficients for the dominant direct and phonon assisted Auger processes, and n, p, and n_d are the densities of excess electrons and holes, and uncompensated donors, respectively. This expression describes hot electron leakage when $\alpha=2$ and $\beta=1$ and hot hole leakage when $\alpha=1$ and $\beta=2$. The height of the confining potential barrier is accounted for in the effective lifetime, τ_{ex}, of the excited carrier.

Equation (2.1) corresponds to Auger-induced leakage from conventional (DH) lasers. The expression will be more elaborate for a quantum well laser, since the structure is more complicated and because energetic carriers due to Auger recombinations will be generated in both the quantum well active region(s) and the separate confinement region. Nevertheless, Eq. (2.1) correctly describes the basic features of the leakage current which are relevant to this discussion.

In InGaAsP lasers, the rate of energetic hole leakage from the active and confinement regions is expected to be a small fraction of the energetic electron leakage for two reasons. First, the energetic hole lifetime is shorter than the energetic electron lifetime because the heterojunction barrier is approximately 50% larger in the valence band. Secondly, the comparatively small hole diffusion coefficient for InGaAsP implies that fewer energetic holes will be within one diffusion length of the cladding.

Equation (2.1) also indicates that Auger-induced leakage will increase with increasing carrier density. Auger-induced energetic carrier leakage will also increase with temperature, since the coefficients for the dominant direct and phonon-assisted Auger processes both increase with temperature [Agrawal *et al.*, p. 115, 1986].

2.4 Leakage by Thermionic Emission

Thermionic emission is a thermally assisted carrier escape process. For thermionic emission over a potential barrier, carriers must acquire sufficient thermal energy from the crystal to promote them to states with a kinetic energy exceeding the given barrier energy. The distribution of thermally populated electron and hole states is accurately described by Fermi-Dirac statistics when the excess carrier populations attain a steady state within the laser active region [Henry *et al.*, 1983]. From a knowledge of the density of states and their probability of occupation, the net thermionic leakage current can be estimated. The discussion will be limited to thermionic emission from the separate confinement region into the cladding, as shown in Fig. 2.1(c).

Under the simplifying assumption of a constant quasi-Fermi level across the interface between the separate confinement region and the InP

cladding, the net diffusion limited leakage current density flowing into the InP due to thermionic emission can be expressed as [Casey et al., 1978]

$$J_{therm} = \frac{q D \rho}{L \tanh [W/L]} \qquad (2.2)$$

where D, L, and W are as defined as in Eq. (2.1) and ρ represents the carrier density just inside the InP cladding. For parabolic bands and a non-degenerate carrier population in the cladding (i.e., such that Boltzmann statistics are valid), ρ is expressed as

$$\rho = 2 \left(\frac{2\pi m^* k T}{h^2} \right)^{3/2} e^{-(\Delta V - E_{qf})/kT} \qquad (2.3)$$

where k is Boltzmann's constant, h is Planck's constant, ΔV is the height of the energy barrier, T is the temperature, and E_{qf} and m^* are the minority carrier quasi-Fermi level and effective mass in cladding region, respectively.

From Eqs. (2.2) and (2.3) it can be surmised that thermionic hole leakage will be a small fraction of thermionic electron leakage in the InGaAsP/InP-based devices, due to the smaller hole diffusion coefficient and the larger heterojunction discontinuity in the valence band. From these equations, it also follows that thermionic leakage currents will increase with temperature and with the carrier density.

2.5 Leakage and the Temperature Dependence of Laser Performance

In semiconductors, the stimulated and spontaneous emission probabilities are interrelated and they are both proportional to the product of the density of populated upper level states (conduction electrons) and the

density of vacant states (holes) to which optical transitions are allowed [Pankove, p. 213, 1971].

Expressions for the rate of spontaneous emission have been derived for both bulk and quantum well active regions [e.g. see Takasaki 1992 and references therein]. For the simple case of parabolic bands and non-degenerate electron and hole populations, the radiative recombination rate in a quantum well is proportional to np, the product of the excess electron and hole densities, and inversely proportional to temperature. Although the temperature dependence is more complicated for degenerate carrier populations, the trend remains that increases in temperature result in a decrease in radiative efficiency. This signifies that the required steady-state electron and hole densities at threshold must increase with temperature.

The combination of higher temperatures and the concomitant requirement for larger steady state carrier densities at threshold will result in more thermionic and Auger-induced energetic carrier leakage. Therefore, these leakage currents may significantly affect the temperature dependence of the laser threshold current and radiative efficiency, and could limit the maximum temperature of operation.

Although it has been widely acknowledged that leakage currents increase with temperature, the correlation between electron leakage and the temperature dependence of semiconductor lasers has been debated for several years. Asada [1983] deemed the magnitude of leakage currents in 1.3-1.55μm DH InGaAsP/InP lasers to be negligible over their operational temperature range; Chik *et al.* [1990] measured 12% current leakage at threshold for 5 μm wide stripe-contact DH InGaAsP/InP lasers at room temperature. Larger (10%-35%) leakage currents were measured directly in a combined DH laser/bi-polar transistor structure investigated by Chen *et al.* [1983].

Recently, Evans [1993] has analyzed the internal quantum efficiency of three (five) quantum well InGaAsP/InP ridge waveguide lasers, and has estimated that leakage losses account for up to 37% (11%) of the threshold current. Ultimately, the temperature sensitivity of laser performance due to the temperature dependence of leakage will depend on the laser structure, including the active region volume, the composition and quality of the active region material, the mirror reflectivities, and the band offsets between the separate confinement and cladding regions.

The sensitivity of the laser threshold current with respect to changes in temperature is usually expressed through the approximate relation

$$I_{th} = I_o \, exp(\, T/T_o \,) \tag{2.4}$$

where the parameter T_O is referred to as the characteristic temperature. T_O is not constant: it varies with temperature. however, it serves to express the temperature *sensitivity* of I_{th} at any given temperature. From Eq. (2.4), T_o can be expressed as

$$T_o = \frac{I_{th}}{\left(\frac{\partial I_{th}}{\partial T}\right)} \tag{2.5}$$

Larger values of T_o imply superior temperature stability. InGaAsP/InP lasers operating at λ_o = 1.3μm-1.55μm typically have T_O values between 40-60K at room temperature.

For investigations into the relationship between leakage currents and the temperature sensitivity of lasers, the volume of the laser active region can be minimized to insure relatively large carrier densities at threshold. The

leakage can also be exacerbated by increasing the temperature, by reducing the cavity length, or by reducing the facet reflectivities.[1]

2.6 Implications for EBR design

Because electron leakage is expected to dominate over hole leakage, an EBR will be incorporated into the p-doped InP cladding region only.

The steady state generation of hot electrons by Auger recombinations in the active and separate confinement regions may be sufficient to establish a non-equilibrium electron energy distribution; i.e. there could be enhanced occupancy around some elevated electron energy. However, in light of the rapid intraband relaxation, it will be assumed that the electron distribution is "normal" in the sense that electron state occupancy increases monotonically with decreasing electron energy. Therefore, in order to repel the maximum number of hot electrons from the InP cladding, the finite band of electron energies for which the EBR is highly reflective will be designed to extend contiguously upward from the InP band edge.

---

[1] A laser attains threshold when the rate of stimulated and spontaneous emission at some wavelength λ_0 is sufficient to sustain unity gain for the round trip passage of a photon at that wavelength. By reducing the cavity length or mirror reflectivities, the stimulated and spontaneous rates must be larger (and hence the carrier densities must be larger) to achieve the threshold condition. Larger carrier densities lead to larger leakage currents.

Chapter 3: Waves in Layered Media

"Same equations have same solutions."

- R. P. Feynman

3.1 Introduction

This chapter presents two versatile Transfer Matrix Methods (TMM's) which can be employed for the analysis of waves in layered media.

Section 3.2 develops a transfer matrix method for electrons (TMME), which can be applied to calculate either bound or quasi-bound electron states in arbitrary 1-D potentials, or to calculate the reflection probability for ballistic electrons striking arbitrarily stratified semiconductor media. The TMME was implemented on a computer to design the InGaAsP/InP superlattice electron Bragg reflector (EBR) presented in Chapter 4.

Section 3.3 presents the transfer matrix method for Optics (TMMO). Particular attention is devoted to the application of newly derived exact analytical transfer matrices to mode calculations for waveguides which include continuously graded regions. It is shown that the exact transfer matrices can provide more than an order of magnitude improvement in computational efficiency in the analysis of graded index waveguides when compared to equivalent calculations using the conventional TMMO.

19

3.2 The Transfer Matrix Method for Electrons

3.2.1 Free Electron Transport

de Broglie's hypothesis asserts that a free electron with momentum p_0 will exhibit wave properties consistent with a wavelength, λ_0, and wavenumber, k_0, given by

$$\lambda_0 = h/p_0 \tag{3.1}$$

and

$$k_0 = 2\pi/\lambda_0 = p_0/\hbar, \tag{3.2}$$

where h is Planck's constant and $\hbar = h/(2\pi)$. The momentum and kinetic energy E_0 are related according to

$$E_0 = p_0^2 / (2m_0) = \hbar^2 k_0^2 / (2m_0), \tag{3.3}$$

where m_o is the electron rest mass.

3.2.2 Electron Transport in Semiconductors

The behaviour an electron in a time-dependent potential $V(r,t)$ is governed by Schrödinger's wave equation [Jonsson et al., 1990]

$$\left(\frac{-\hbar^2}{2\,m_o} \nabla \cdot \nabla + V(\mathbf{r},t) \right) \Phi(\mathbf{r},t) = i\hbar \frac{\partial}{\partial t} \Phi(\mathbf{r},t) \tag{3.4}$$

where ∇ represents the vectorial gradient, and $\Phi(\mathbf{r},t)$ is the electron wavefunction.

To simplify the analysis of electron transport in crystals, the potential can be considered static, i.e. $V(r,t) \approx V(r)$. In this case, $\Phi(r,t)$ is separable as [Boer, p. 1210, 1991]

$$\Phi(r,t) = \psi(r)\, s(t), \tag{3.5}$$

where

$$s(t) = e^{-i E t / \hbar} \tag{3.6}$$

and

$$\psi(r) = u(r)\, e^{\pm i \mathbf{k} \cdot \mathbf{r}}. \tag{3.7}$$

In Eqs. (3.6)-(3.7), E is the electron energy, and $u(r)$ is a function having the periodicity of the crystal lattice. The exponential term in Eq. (3.7) imposes a Bloch[1] traveling wave envelope for electron energies corresponding to propagating states (for which the wavevector $\mathbf{k}$ is real), and a spatially decaying envelope for energies at which electron propagation is inhibited by fundamental or higher order Bragg reflection from the crystal potential (for which $\mathbf{k}$ is imaginary).

Within the bands of energy corresponding to propagating states, the net change of electron momentum in response to applied fields is consistent with an *effective* electron mass, m^*. For electron energies near the band extrema, m^* is nearly constant, so that a parabolic E vs. k dispersion relation (analogous to that of a free electron, § 3.2.1) is recovered, in which the Bloch wavevector, k, replaces k_0, and m^* replaces m_o as the apparent electron mass. The E vs. k relationship departs increasingly from parabolicity as the electron energy increases relative to the band extremum. For conduction band

---

[1] $u(r)$ is typically referred to as the Bloch *function*. However, it is the electron wave envelope which is central to this thesis; for brevity it will be referred to as the Bloch wave.

electrons, the nonparabolicity can be approximated by ascribing to the electron an *energy dependent* effective mass [Nelson *et al.*, 1990]

$$m^*(E) \approx m_{be}^* \left(1 + 2 \frac{E}{E_g} \left(1 - \frac{m_{be}^*}{m_o} \right)^2 \right), \tag{3.8}$$

where m_{be}^* is the effective mass at the band edge, and E_g is the band gap.

3.2.3 The Envelope Function Approximation

In most analyses of semiconductor nanostructures, the envelope function approximation (EFA) [Bastard, 1981 and 1982] is invoked. In the EFA, the band structure, the electron effective mass, and the electron Bloch envelope function description are retained, but phenomena explicitly related to the rapid variation of the crystal potential within the unit cell are discarded. Then, in Eq. (3.7), $u(r)$ can be replaced by a constant[2]. By substituting Eqs. (3.7) into Eq. (3.4) and dividing by Eq. (3.6), the time *independent* single particle Schrödinger equation is obtained. For media in which the relevant variation of V occurs along a single direction (say, x), the wave equation is [Jonsson *et al.*, 1990]

$$\left(\frac{-\hbar^2}{2} \frac{d}{dx} \frac{1}{m^*(x)} \frac{d}{dx} + V(x) \right) \psi(x) = E \, \psi(x). \tag{3.9}$$

The form of the differential operator in Eq. (3.9) guarantees that all eigenfunction solutions satisfy continuity of both amplitude and probability flux throughout media characterized by a *continuously* varying profile of $V(x)$ and $m(x)$ [e.g. see Henderson *et al.*, 1992], or at an abrupt interface between

---

[2]This approximation is valid only when the underlying crystal symmetry is maintained throughout the structure.

media with disparate values of V and/or m^*, where these boundary conditions are

$$\psi_a = \psi_b, \qquad \text{(amplitude)},$$

$$\frac{1}{m_a^*}\frac{d\,\psi_a}{dx} = \frac{1}{m_b^*}\frac{d\,\psi_b}{dx}, \qquad \text{(flux)}$$

(3.10)

where the subscripts a and b denote the left and right side of the interface.

It is important to note that in the EFA, only the Bloch wave and its wavelength (and *not* the de Broglie wavelength of § 3.2.1) are considered in the design of an electron Bragg reflector.

3.2.4 Transfer Matrix Analysis of Piece-Wise Homogeneous Media

Consider the arbitrary structure shown in Fig. 3.1(a), which consists of a stack of j homogeneous layers bounded by semi-infinite media. This description is appropriate for a stack of hetero-epitaxial layers with sharp boundaries. Media with *continuous* profiles of m^* or V can be approximated by a dense stack of thin layers rendering a piece-wise constant "staircase" representation of the smooth m^* and V profiles.

The functional form of $\psi(r)$ within the nth layer is given by superpositions of the two linearly independent solutions of Eq. (3.9),

$$\psi(x) = A_n\,e^{+i\,k_n\,x} + B_n\,e^{-i\,k_n\,x},$$

$$k_n = \frac{\sqrt{2\,m_n^*(E)\,(E - V_n)}}{\hbar},$$

(3.11)

where A_n and B_n are undetermined coefficients, and V_n and $m_n^*(E)$ are the potential and effective mass in the nth layer, respectively. The problem of determining physically meaningful wavefunctions for the entire structure

consists of determining an appropriate value for A and B in each layer. If the coefficients A and B are known or specified in *one* of the layers, then the values of A and B can be calculated for *all* the remaining layers by the successive application of the boundary conditions given by Eq. (3.10).
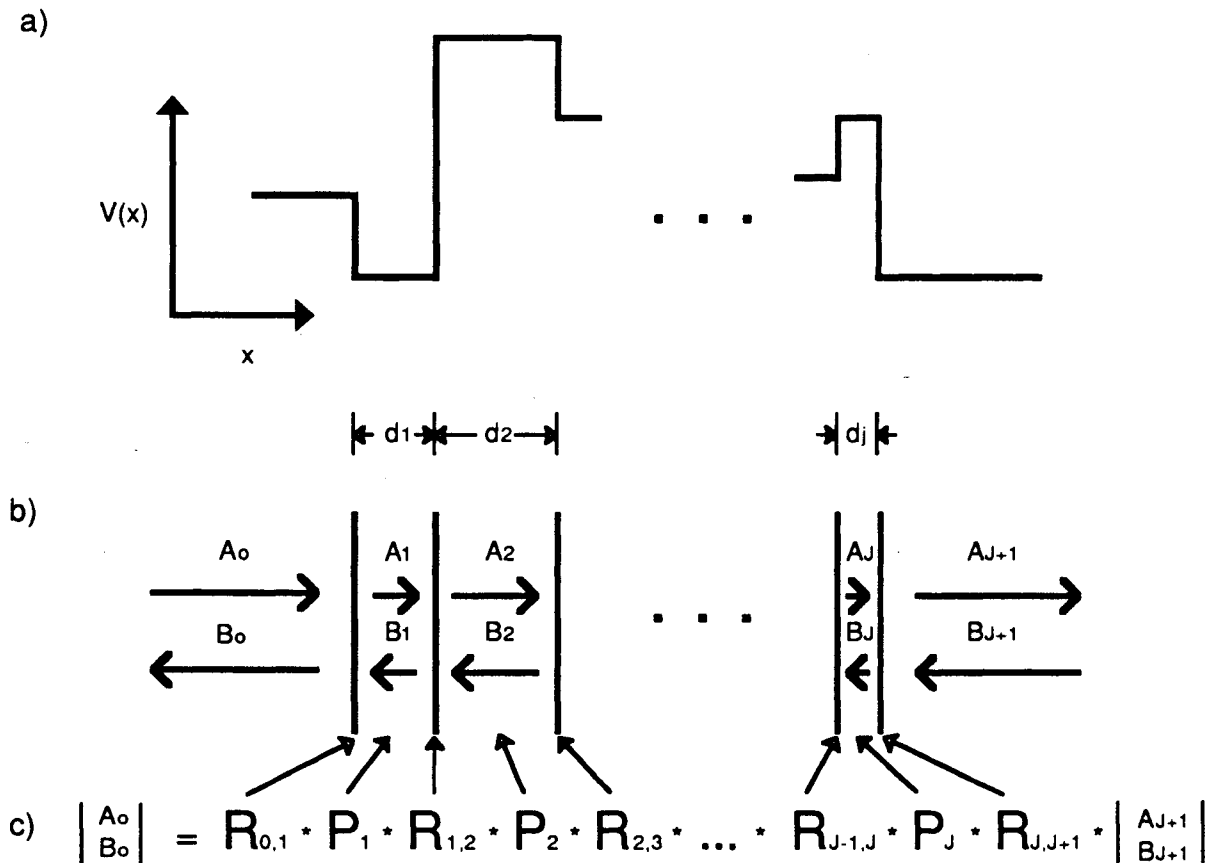
Figure 3.1: Mapping of a semiconductor potential energy profile into the product of transfer matrices. (a) Piece-wise constant V(x) profile consisting of j layers of thickness d_j bound by semi-infinite media. (b) In each layer, the wavefunction consists of right and left traveling waves with amplitudes A_j and B_j, respectively. (c) The structure can be mapped to the sequential product of transfer matrices R and P which represent the change in wave amplitudes at layer interfaces and the phase advance between interfaces, respectively.

The task of successively applying the boundary conditions can be cast in matrix form. The procedure involves the use of two basic 2 x 2 transfer matrices.

The first type of transfer matrix accounts for reflection and transmission at abrupt interfaces. Specifically, the coefficients A and B on both sides of the interface separating medium n and n+1 are related by [Gaylord et al., 1989]

$$\begin{bmatrix} A_n \\ B_n \end{bmatrix} = \frac{1}{t_{n,n+1}} \begin{bmatrix} 1 & r_{n,n+1} \\ r_{n,n+1} & 1 \end{bmatrix} \cdot \begin{bmatrix} A_{n+1} \\ B_{n+1} \end{bmatrix}$$

$$\equiv \mathbf{R}_{n,n+1} \cdot \begin{bmatrix} A_{n+1} \\ B_{n+1} \end{bmatrix},$$

(3.12)

where[3] [Zebda et al., 1992]

$$r_{n,n+1} = \frac{Z_n - Z_{n+1}}{Z_n + Z_{n+1}},$$

(3.13)

$$t_{n,n+1} = \frac{2 Z_n}{Z_n + Z_{n+1}},$$

(3.14)

and

$$Z_n = \sqrt{(E - V_n)/m_n^*}.$$

(3.15)

is the characteristic impedance of the nth layer.

The second type of transfer matrix relates A and B at the left interface of the nth layer to their value at the right interface within the same layer. By inspection of Eq. (3.11), this matrix is

---

[3]The boundary conditions in Eq. (3.10) are implicit in the reflection and transmission formulas (Eqs. (3.13) and (3.14)) which relate the wave amplitudes on both sides of the interface.

$$\begin{bmatrix} A_n^- \\ B_n^- \end{bmatrix} = \begin{bmatrix} e^{-ik_nd_n} & 0 \\ 0 & e^{+ik_nd_n} \end{bmatrix} \cdot \begin{bmatrix} A_n^+ \\ B_n^+ \end{bmatrix}$$

(3.16)

$$\equiv \mathbf{P}_n \cdot \begin{bmatrix} A_n^+ \\ B_n^+ \end{bmatrix},$$

where d_n is the layer thickness.

The value of A and B in any two non-adjacent layers are related by the transfer matrices which represent the intervening interfaces and layers. It follows that the coefficients at the left interface of the structure are related to the coefficients at the far right interface by the sequential product of the transfer matrices for all intermediate interfaces and layers, i.e.

$$\begin{bmatrix} A_0 \\ B_0 \end{bmatrix} = \mathbf{R}_{0,1} \cdot \mathbf{P}_1 \cdot \mathbf{R}_{1,2} \cdot \mathbf{P}_2 \cdot \ldots$$

$$\ldots \cdot \mathbf{R}_{j-1,j} \cdot \mathbf{P}_j \cdot \mathbf{R}_{j,j+1} \cdot \begin{bmatrix} A_{j+1} \\ B_{j+1} \end{bmatrix},$$

(3.17)

or

$$\begin{bmatrix} A_0 \\ B_0 \end{bmatrix} = \mathbf{T}_T \cdot \begin{bmatrix} A_{j+1} \\ B_{j+1} \end{bmatrix},$$

(3.18)

where $\mathbf{T}_T$ is the product of all the 2 x 2 matrices. Each element of $\mathbf{T}_T$ is a function of the electron energy E. Equation (3.18) can be used to predict the reflection and transmission (§ 3.2.5) and the bound or quasi-bound states (§ 3.2.6) of electrons in stratified semiconductor media.
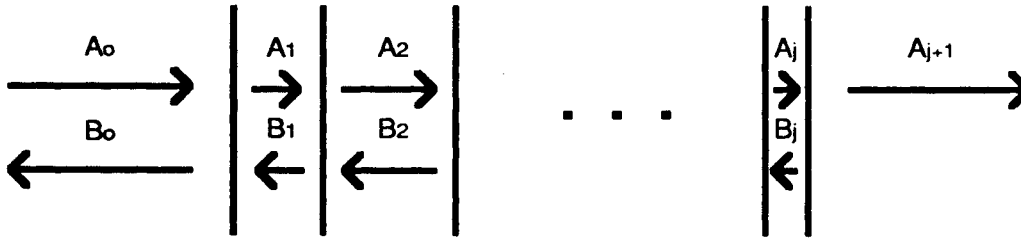
Figure 3.2: Electron reflection from a multiple layer stack. The wavefunction in the incident medium consists of an incoming and outgoing (reflected) wave. The medium on the far right contains only an outgoing (transmitted) wave.

3.2.5 Quantum Mechanical Reflection and Transmission

The TMME can be applied to compute the reflection and transmission probabilities of an electron which is incident upon a multiple layer stack. In the incident medium, the electron wavefunction is comprised of both an incoming and outgoing (reflected) wave, whereas only an outgoing (transmitted) wave is present in the final medium (see Fig. 3.2). The matrix relation becomes

$$\begin{bmatrix} A_0 \\ B_0 \end{bmatrix} = \mathbf{T}_T \cdot \begin{bmatrix} A_{j+1} \\ 0 \end{bmatrix}. \tag{3.19}$$

Eq. (3.19) can be expanded in terms of the elements $\{t_{ij}\}$ of $\mathbf{T}_T$. The reflectivity of the stack is given by ratio of the reflected wave amplitude (B_0) divided by the incident wave amplitude (A_0), multiplied by its complex conjugate; the term A_{j+1} cancels and the result is

$$R(E) = \left| \frac{B_0}{A_0} \right|^2 = \left| \frac{t_{21}(E)}{t_{11}(E)} \right|^2. \tag{3.20}$$

Applying conservation of probability, the transmissivity is

$$T(E) = 1 - R(E). \tag{3.22}$$
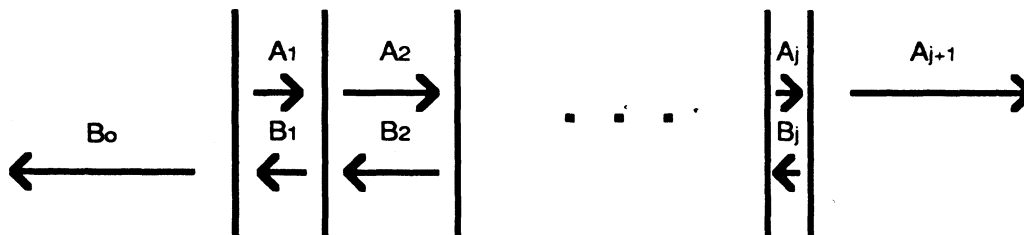
Figure 3.3: Bound or quasi-bound electron states within a multiple-layer structure. The bounding media only contain outgoing waves. For bound states, these waves are exponentially decaying with increase distance away from the structure. For quasi-bound states, one or both of the outgoing waves may be sinusoidal, carrying a finite probability current away from the confining structure.

3.2.6 Calculation of Bound or Quasi-Bound States

For electron states bound within a confining structure, the wavefunction in the two outer media consists of a single wave "propagating" evanescently *away* from the confining structure (see Fig. 3.3). For this case, the matrix relation is

$$
\begin{vmatrix} 0 \\ B_0 \end{vmatrix} = \mathbf{T}_T \cdot \begin{vmatrix} A_{j+1} \\ 0 \end{vmatrix},
\tag{3.22}
$$

This relation is only true when

$$
t_{11}(E) = 0.
\tag{3.23}
$$

Equation (3.23) is the eigenvalue condition for the discrete values of electron energy, E_n, which correspond to bound states.

The confining structure may also support "quasi-bound" states at electron energies *exceeding* the potential energy of one or both of the

bounding media. Once again, each outer medium must contain a single outward propagating wave; however, this wave is a *sinusoidal traveling wave* in the bounding medium (or media) where the state energy exceeds the potential. Sinusoidal waves carry probability current, and consequently an electron in a quasi-bound state is expected to escape from the confining structure after a finite time.

The matrix relation for quasi-bound states and the energy eigenvalue equation are given by Eqs. (3.22) and (3.23), presented above for bound states. However, unlike bound states, the quasi-bound state energy eigenvalues are complex. The imaginary part of the energy eigenvalue dictates the "decay" of the state through Eq. (3.6); the expected $1/e$ lifetime is

$$\tau = \frac{\hbar}{Im\{ E \}}. \tag{3.24}$$

3.2.7 More Advanced Transfer Matrix Methods for Electron Waves

Transfer matrix methods using Airy basis functions have been derived for applications to structures described by piece-wise *linear* variations of V(x) [Lui *et al.*, 1986; Hutchings, 1989; Glytsis *et al.*, 1989]. A TMME with a basis consisting of parabolic cylinder functions was employed [Hung *et al.* 1992] to analyze electron tunneling in piece-wise homogeneous media under the influence of an in-plane magnetic field. An expansion in terms of exponentially weighted Kummer functions like that derived in this thesis (§ 3.3.4) would generalize Hung's analysis to media with a potential profile consisting of any combination of piece-wise constant, linear, or parabolic segments. Additional details on the TMME for piece-wise homogeneous media can be found in Gaylord *et al.*, 1989.

3.3 The Transfer Matrix Method for Optics

3.3.1 Introduction

The propagation of electromagnetic energy in stratified media has been investigated for over a century. The mathematical treatment of the reflection and transmission of light by multiple-layer coatings was first considered in detail by Lord Rayleigh in 1912, and was later cast into matrix form by Herpin [1947] and Abeles [1950]. The first application of transfer matrices to calculate the modes of multiple layer waveguides is attributed to Brekhovskikh [1960]. More recently, the transfer matrix technique for analyzing multiple-layer optical waveguides has been extended to include bi-refringent media [Vassel, 1977; Walpita, 1985].

The basic transfer matrix method for optics (TMMO) can be used to determine the optical properties of any waveguide, coating, or grating which can be described as a finite stack of homogeneous planar layers. This m-layer description is appropriate for a broad class of technologically important devices which can be fabricated by Molecular Beam Epitaxy (MBE) or Metal Organic Chemical Vapour Deposition (MOCVD), including edge-emitting and surface-emitting semiconductor lasers. Like the TMME, the TMMO involves the transfer of wave amplitudes through a structure by 2 x 2 matrices. With appropriate boundary conditions, the TMMO yields reflection and transmission spectra, or the properties of guided or leaky waveguide modes (which are analogous to bound and quasi-bound electron states, respectively).

In the application of the basic TMMO to graded-index waveguides [Walpita, 1985; M. Adams p.169, 1981], the graded regions are approximated by a dense stack of thin layers rendering a piece-wise constant "staircase" representation of the smooth profile of the dielectric constant (see Fig. 3.2).

However, there are a number of functional forms of the continuous variation of the dielectric constant for which an exact analytical 2 x 2 transfer matrix can be derived, particularly for transverse-electric (TE) polarized light[4]. In many cases of practical interest, these exact transfer matrices will provide a compact and computationally efficient alternative to the approximation of graded regions by a large number of thin homogeneous layers.

In this section, newly derived exact traveling wave and tangential field transfer matrices are presented for the description of TE polarized light in media with an arbitrary linear, exponential, or parabolic profile of the complex dielectric constant. These matrices are of particular interest for mode calculations in unstrained or compressively strained graded index multiple quantum well lasers (or the components which these lasers illuminate), where TE oscillation prevails due to quantum mechanical selection rules [Asada, 1984; Chong et al., 1989]. In addition to mode calculations, these matrices may be used for the design or analysis of graded-index thin films with absorption or gain, including periodic structures such as surface emitting distributed feedback semiconductor lasers in which the interfaces between epitaxial layers are graded to reduce electrical resistance [Zhou et al., 1991].

For brevity, only mode calculations will be discussed here.

---

[4](i.e. where the electric field lies *parallel* to the plane of stratification).

3.3.2 Waveguide Modes

Figure 3.4 illustrates a non-magnetic ($\mu=1$) dielectric planar waveguide consisting of m homogeneous layers of thickness d_i ($i=1,...,m$) and total thickness $W = \Sigma d_i$, bounded by semi-infinite media. The guided optical modes of this structure are electromagnetic wave excitations that propagate along the z direction and are spatially localized (i.e. square-integrable) in the x direction. For guided modes in structures bound by homogeneous, lossless media, the fields in the bounding media decay exponentially with increasing distance from the guide.

In each waveguide layer, the local modal fields consist of superposition of the solutions to Maxwell's wave equation in that layer. In a homogeneous layer the solutions are plane waves, whose wave-vector can be projected into two components; one parallel ($k_o n_z$) and one perpendicular ($k_o n_x$) to the plane of stratification (see Fig. 3.4). The components satisfy $k_o^2 n_x^2 + k_o^2 n_z^2 = k_o^2 n^2$, where n is the refractive index of the layer.

Consider the parallel component ($k_o \, n_z$). The continuity of tangential field amplitudes implies that this component must be identical throughout the waveguide; the term $k_o \, n_z$, will therefore dictate the modal phase advance along the direction of propagation according to

$$\mathcal{E}_y(x,y,z) = \mathcal{E}_y(x,y) \, e^{i \, k_o n_z z} , \qquad\qquad (3.25)$$

where n_z is the mode index.

The procedure for determining guided modes consists of trying n_z values which correspond to decaying fields in medium 0, and transferring the field amplitudes through all remaining layers ($1,2,...,m+1$) while maintaining
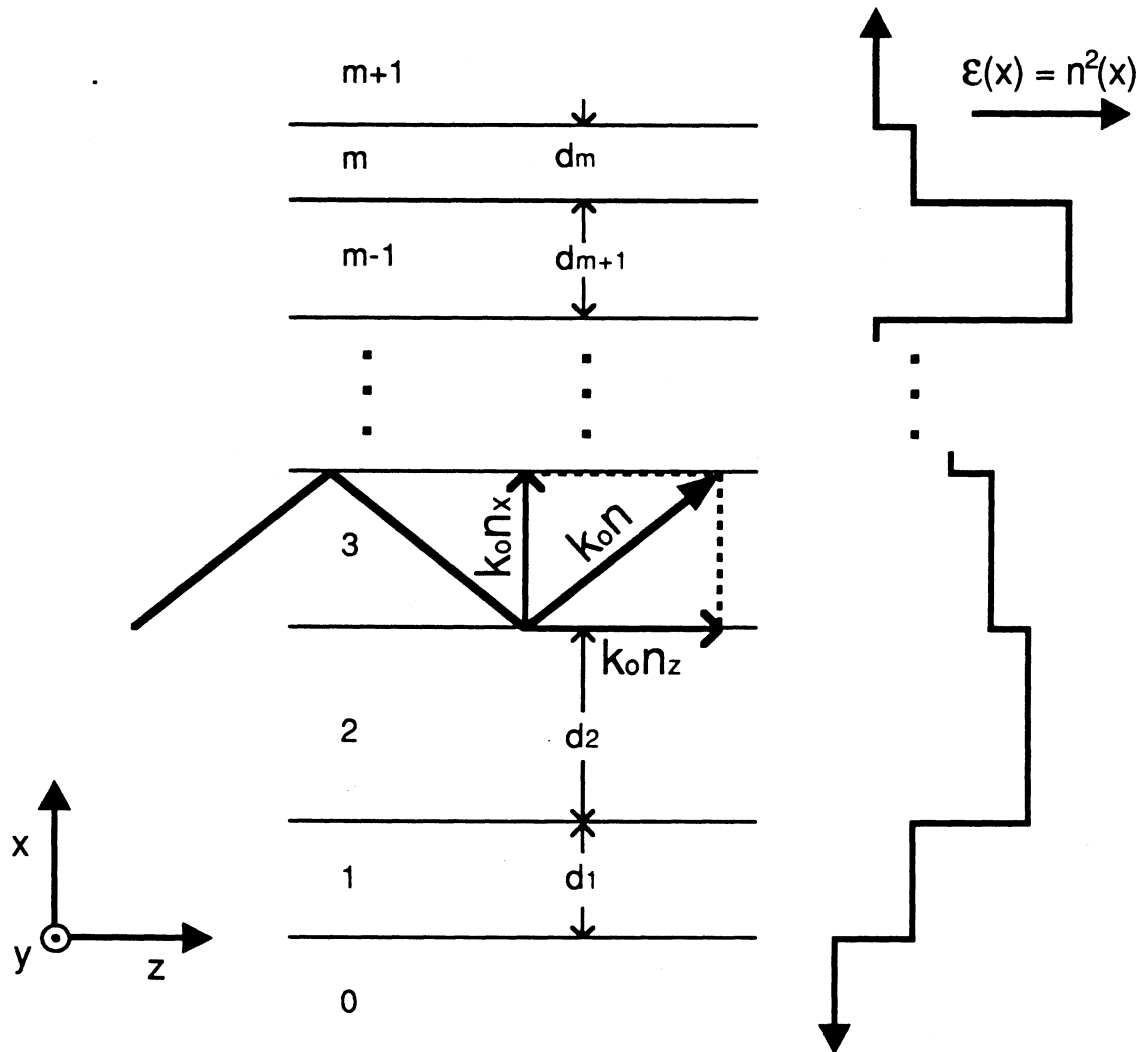
Figure 3.4: Waveguide consisting of m homogeneous layers bounded by semi-infinite media. In each layer, the mode will consist of plane waves. The z component of the wave-vector must be a constant throughout the waveguide to satisfy tangential E and H field continuity.

the constancy of $k_o n_z$. If the fields in medium m+1 are found to be purely decaying, then n_z is a valid mode index. As with the TMME, the transfer of field amplitudes is easily accomplished by the multiplication of 2 x 2 matrices. In fact, the TMME presented in § 3.2 can be directly converted to the TMMO by simply replacing the Bloch wave-vector by the optical wavevector, and the

expressions for electron reflection and transmission (Eqs (3.13) and (3.14)) by the expressions for Fresnel reflection and transmission[5] [Gaylord *et al.*, 1989]. The formal equivalence of the two methods underlies the universality of wave phenomena in physics[6], and supports the analogies drawn between the modes of optical waveguides and the states of electrons confined in quantum wells.

The TMMO for piece-wise homogeneous planar waveguides has been described elsewhere [e.g., Walpita, 1984]. The remainder of this section presents the analysis of graded-index waveguides using exact transfer matrices newly derived by the author. The analysis employs both traveling wave matrices (analogous to those presented for the TMME) and equivalent matrices which translate the value of the tangential electric and magnetic fields.

3.3.3 General Form of Tangential Field and Traveling Wave Transfer Matrices for TE Polarized Electromagnetic Waves

Maxwell's wave equation for the amplitude of the transverse electric field, $\mathcal{E}(x) \equiv (0, \mathcal{E}_y(x), 0)$ in one layer of the waveguide may be written as

$$\frac{\partial^2}{\partial x^2} \mathcal{E}(x) + k_o^2 (\varepsilon(x) - n_z^2) \, \mathcal{E}(x) = 0, \tag{3.26}$$

for $0 \leq x \leq d$. For this equation, $k_o = 2\pi/\lambda_o$, λ_o is the vacuum wavelength, $\varepsilon(x) \equiv \varepsilon_r(x) + i \, \varepsilon_i(x)$ is the profile of the complex dielectric constant in the layer, and n_z is the complex mode index.

---

[5]However, in optical waveguides, rather than searching for eigenvalues of the wave-vector component *normal* to the interfaces (as is done in the search for electron Bloch wave eigenstates in the TMME), it is customary (and equivalent) to search for eigenvalues of the component *parallel* to the direction of propagation, $k_o \, n_z$.

[6]Similar transfer matrix methods exist for the treatment of acoustical waves

From any two independent non-trivial analytic solutions ξ_1, ξ_2 of Eq. (3.26), a 2 x 2 matrix **M** can be derived which relates the tangential electric ($\mathcal{E}$) and magnetic ($\mathcal{H}$) field amplitudes at the layer boundaries $x=0$ and $x=d$ through the relation

$$\begin{bmatrix} \mathcal{E}(0) \\ \mathcal{H}(0) \end{bmatrix} = \mathbf{M} \cdot \begin{bmatrix} \mathcal{E}(d) \\ \mathcal{H}(d) \end{bmatrix} \tag{3.27}$$

The matrix **M** can be expressed as

$$\mathbf{M} = \mathbf{S}^{-1}(0) \cdot \mathbf{S}(d), \tag{3.28}$$

with

$$\mathbf{S}(x) = \begin{bmatrix} \xi_1'/(ik_o) & -\xi_1 \\ \xi_2'/(ik_o) & -\xi_2 \end{bmatrix}, \tag{3.29}$$

where the prime denotes $\partial/\partial x$.

In some investigations [e.g. Schlereth *et al.*, 1990; Ghatak *et al.*, 1987; Hulse *et al.*, 1992] the net amplitude of the transverse electric field is resolved into the sum of a forward- and a reverse-traveling wave,

$$\mathcal{E} = E^+ + E^-. \tag{3.30}$$

For this case,

$$\begin{bmatrix} E^+(0) \\ E^-(0) \end{bmatrix} = \mathbf{T}_\mathrm{T} \cdot \begin{bmatrix} E^+(d) \\ E^-(d) \end{bmatrix}, \tag{3.31}$$

where the traveling wave transfer matrix **T** can be obtained from

$$\mathbf{T} = \mathbf{J}_0^{-1} \cdot \mathbf{M} \cdot \mathbf{J}_\mathrm{d}, \tag{3.32}$$

with

$$\mathbf{J_i} = \begin{bmatrix} 1 & 1 \\ p_i & -p_i \end{bmatrix},$$ (3.33)

where $p_i = \pm \sqrt{n_i^2 - n_z^2}$ is positive (negative) for net modal gain (loss), and n_0 and n_d are the refractive index at $x=0$ and $x=d$, respectively.

The representation by traveling waves (i.e. using matrices of the form given by $\mathbf{T}$) is rigorously equivalent to an analysis of the tangential electric and magnetic fields using $\mathbf{M}$ matrices.

3.3.4 Wave Equation Solutions for Homogeneous and Graded Media

To apply the transfer matrix method to graded-index waveguides, two independent solutions of Maxwell's wave equation (Eq. (3.26)) for each graded region are required. For the trivial case

$$\varepsilon(x) = \text{a constant} = n^2,$$ (3.34a)

two solutions are

$$\xi_1 = cos(\, q\, x\,),$$
$$\xi_2 = sin(\, q\, x\,),$$
$$q = k_o(\, n^2 - n_z^2\,)^{1/2}.$$ (3.34b)

and Eq. (3.28) yields the familiar transfer matrix of a homogeneous film. For the linear variation [D. Adams *et al.*, 1992],

$$\varepsilon(x) = a\, x + b$$ (3.35a)

the solutions are

$$\xi_1 = Ai(\,\zeta\,),$$

$$\xi_2 = Bi(\,\zeta\,),$$

$$\zeta = -(\,k_o^2\,a\,)^{1/3}\,(x + (\,b - n_z^2\,)/a\,) \qquad (3.35b)$$

where Ai and Bi denote the A- and B-Airy functions. For an exponential variation

$$\varepsilon(x) = a\,e^{\,b\,x} + c,\ (a,\,b \neq 0)\,, \qquad (3.36a)$$

two independent solutions and their derivatives are given by

$$\xi_i = C_\rho(\,v\,),$$

$$\xi_i' = v'\,\left(C_{\rho\text{-}1}(\,v\,) - \rho\,\xi_i\,/\,v\right),$$

$$v = 2\,k_o\,\sqrt{a}\,e^{bx/2}/\,b,\ \ \rho = 2\,k_o\,\sqrt{n_z^2 - c}\,/b \qquad (3.36b)$$

where, for $i = 1\ (\,2\,)$, C_ρ denotes the Bessel functions J (Y) of order ρ. For a general quadratic variation described by

$$\varepsilon(x) = a\,x^2 + b\,x + c,\ (\,a \neq 0\,), \qquad (3.37a)$$

the solutions can be expressed as

$$\xi_1 = e^{-v/2}\,M(\,u;\,\tfrac{1}{2};\,v\,),$$

$$\xi_2 = w\,e^{-v/2}\,M(\,u+\tfrac{1}{4};\,\tfrac{3}{2};\,v\,),$$

$$\xi_1' = \sigma w\,\left(2\,u\,e^{-v/2}\,M(\,u+1;\,\tfrac{3}{2};\,v\,) - \xi_1/2\,\right)$$

$$\xi_2' = \sigma\left(\,(\,4u+2\,)\,v\,e^{-v/2}M(\,u+\tfrac{3}{2};\,\tfrac{5}{2};\,v\,)/3 - (\,v-1\,)\xi_2\,/w\,\right), \qquad (3.37b)$$

where

$$v = w^2/2,\ \ w = \sigma\,x - 2\,bk_o^2/\sigma^3,\ \ \sigma = (\,-4\,a\,k_o^2\,)^{1/4},$$

$$u = 1/4 + k_o^2[\,n_z^2 - c - b/(4\sigma^4)\,]^2/(\,2\sigma^2\,), \qquad (3.37c)$$

and $M(p; q; z)$ is Kummer's hypergeometric function [e.g. see Abromowitz *et al.*, Chap. 13, 1964].

3.3.6 Application to Mode Index Calculations

The wave amplitudes on the two sides of the waveguide are related by the sequential product of the transfer matrices representing all the layers,

$$\begin{bmatrix} \mathcal{E}(0) \\ \mathcal{H}(0) \end{bmatrix} = \mathbf{M}_1 \cdot \mathbf{M}_2 \cdot \ldots \cdot \mathbf{M}_m \cdot \begin{bmatrix} \mathcal{E}(W) \\ \mathcal{H}(W) \end{bmatrix}$$

$$\equiv \mathbf{M}_T \cdot \begin{bmatrix} \mathcal{E}(W) \\ \mathcal{H}(W) \end{bmatrix}. \tag{3.38}$$

Equivalently,

$$\begin{bmatrix} E^+(0) \\ E^-(0) \end{bmatrix} = \mathbf{J}_0^{-1} \cdot \mathbf{M}_T \cdot \mathbf{J}_{m+1} \cdot \begin{bmatrix} E^+(W) \\ E^-(W) \end{bmatrix}$$

$$\equiv \mathbf{T}_T \cdot \begin{bmatrix} E^+(W) \\ E^-(W) \end{bmatrix}, \tag{3.39}$$

For guided modes, the media bounding the waveguide must contain only decaying fields. This requirement yields an eigenvalue equation for n_z which can be formulated in terms of the elements of either $\mathbf{M}_T$ [Chilwell *et al.*, 1984] or $\mathbf{T}_T$ [Hulse *et al.*, 1992; Schlereth *et al.*, 1990]. The latter is

$$t_{11}(n_z) = 0. \tag{3.40}$$

For leaky modes, or for modes in waveguides with absorption or gain, the eigenvalue equation is identical but the mode indexes are complex. The imaginary part dictates the modal attenuation or gain through Eq. (3.25).

3.3.6 Example Applications

Applications of transfer matrices using Eqs. (3.35)-(3.37) to the calculation of the mode index of graded-index waveguides can improve computational efficiency when compared to calculations of n_z based on a simple piece-wise constant approximation of the $\varepsilon(x)$ profile.

For example, the exact TE mode indices at $\lambda_o = 1.55\mu m$ for the linearly and exponentially graded lossless seven-layer quantum well waveguides illustrated in Fig. 3.5 are, respectively, $n_z = 3.229165$ and $n_z = 3.223067$, where $b=4$ in Eq. (3.36) was used for the latter. To obtain n_z with equivalent accuracy by the staircase method, each graded region must be represented by 81 steps of equal width, requiring much longer computation time.
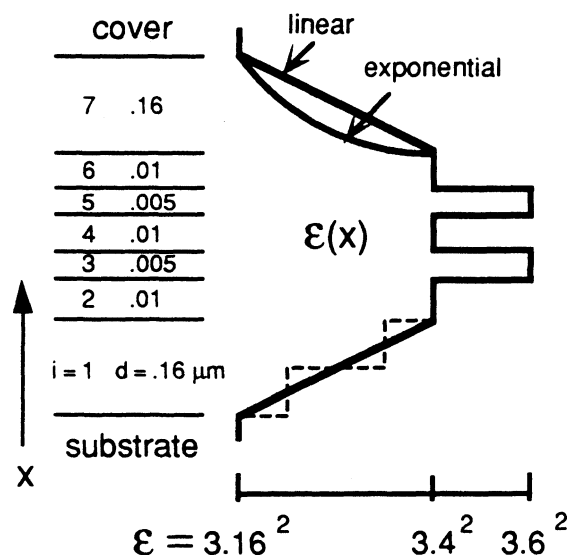
Figure 3.5: Profile of $\varepsilon_r(x)$ for a quantum well waveguide consisting of 7 layers, where layers 1 and 7 are graded linearly or exponentially. The dashed line illustrates the approximation of a linearly graded region by two piece-wise constants segments of equal width.

The efficiency of mode index calculations for waveguides including graded regions with *specific* (i.e., linear, exponential, or parabolic) $\varepsilon(x)$ profiles can be advantageous in many cases of practical interest, particularly for waveguide or laser design. However, it is also important to consider the advantages provided by the exact transfer matrices presented here to the analysis of waveguides with *arbitrary* continuous profiles of $\varepsilon_r(x)$ and $\varepsilon_i(x)$.
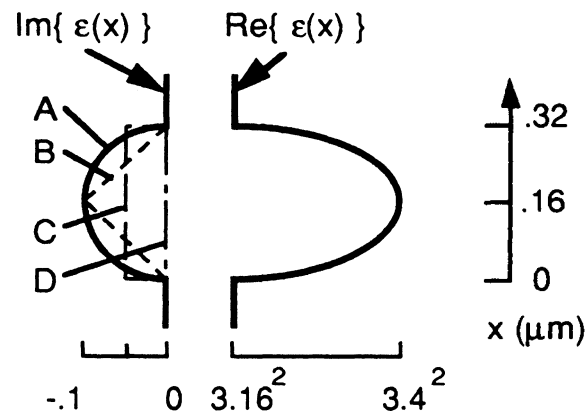
Figure 3.6: Waveguide with a parabolic profile of $\varepsilon_r(x)$ and four possible profiles of $\varepsilon_i(x)$: (A) parabolic, (B) linear, (C) constant, and (D) zero. Re{ n_z } and modal loss for $\lambda_0 = 1.55\mu m$ are, respectively: 3.210792, 1934.302 dB/cm; 3.210832,1473.102 dB/cm; 3.210849, 1369.326 dB/cm; and 3.210893, 0 dB/cm

Figure 3.6 illustrates a waveguide having a parabolic $\varepsilon_r(x)$ profile with four possible $\varepsilon_i(x)$ profiles, i.e. parabolic, linear, constant, and zero. The exact mode index has been calculated for each case by using the transfer matrices given by Eqs. (3.37). For investigative purposes, it can be assumed that case A ($\varepsilon_i(x)$ parabolic) represents an $\varepsilon(x)$ profile for which no exact transfer matrices are available. Figure 3.7 shows the relative error in the calculation

of the modal loss when the continuous profile of $\varepsilon(x)$ in Fig. 3.6 (case A) is approximated by equal-width piece-wise constant and piece-wise linear segments. In the piece-wise constant representation, the value of ε_r (ε_i) in each segment is equal to the mean of the real (imaginary) part of $\varepsilon(x)$ within that segment. The linear segments reproduce the mean of both $\varepsilon_r(x)$ and $\varepsilon_i(x)$ and their first derivative within the segment. It is seen that the representation by piece-wise linear segments provides an improvement in accuracy by *two to three orders of magnitude*.
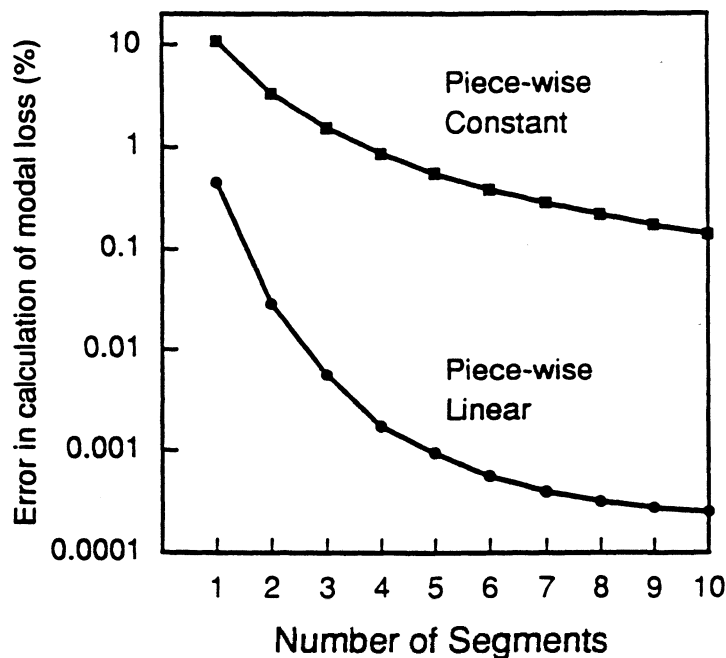
Figure 3.7: Relative error (%) in the calculation of the modal loss vs. the number of equal width segments used to approximate each side of the symmetric complex profile of $\varepsilon(x)$ shown in Fig. 3.6, case A.

On the computer on which calculations for Fig. 3.7 were performed, the evaluation of n_z for a given number of piece-wise linear segments required approximately twice the computation time needed to calculate a value for n_z based on a an identical number of piece-wise constant segments. However, in light of the data in Fig. 3.7, it follows that *for any fixed accuracy target, the use of piece-wise linear segments can provide a net reduction in computation time by at least one order of magnitude.*

The accuracy of calculations employing the exact transfer matrices may be limited by the finite computational accuracy in the evaluation of Airy, Bessel, or Kummer functions for certain limiting cases. Specifically, errors may become appreciable when a in Eqs. (3.35)-(3.37) or b in Eq. (3.36), approaches zero, or for waveguides which are large compared to the light wavelength and/or which are close to cut-off. Transfer matrix mode calculations for the example waveguides were performed in which the computer's Airy, Bessel, and Kummer functions were replaced by routines to evaluate their respective ascending series (e.g. see Eqs. (9.1.2), (9.1.10), (10.4.2), (10.4.3), and (13.3.2) in Abromowitz *et al.*, 1964) to a finite number of terms. It was found that an evaluation to 11 terms yielded a mode index and attenuation which were accurate to at least seven significant digits for all the examples considered here.

The transfer matrices presented here may also be employed in the analysis of distributed Bragg reflectors with loss or gain [D. Adams *et al.*, 1992], or in the computation of the coupling coefficient in distributed feedback lasers with arbitrary grating corrugation profiles [Makino *et al.*, 1991].

Finally, several authors have proposed the use of Cauchy's path integral for the identification and rapid location of the eigenvalues of the

characteristic equation obtained from the TMMO to determine the modes for piece-wise homogeneous planar waveguides [Anemoglannis et al., 1992; Smith *et al.*, 1991; Sun *et al.*, 1991]. These techniques can also be applied to obtain the modes of graded index planar waveguides described by the transfer matrices presented here, because the analyticity of the eigenvalue equation is not eliminated when one or more of these matrices are included in the matrix product.

Chapter 4: Electron Bragg Reflector Design

4.1 Introduction

This chapter describes the design of the InGaAsP/InP electron Bragg reflector (EBR). Several physical and fabrication-related factors that are expected to influence the performance of the EBR are addressed. Section 4.2 details design considerations that arise under the simplifying assumption of electron transport which is coherent (i.e. free of inelastic collisions). Section 4.3 outlines additional design features introduced to provide improved functionality with regard to finite electron coherence.

4.2 Basic EBR Design Considerations Under the Assumption of Coherent Electron Wave Transport

The EBR comprises a stack of InGaAsP wells and InP barriers whose thicknesses are chosen to satisfy the first order Bragg reflection condition for a target electron energy, E_{max}. Bragg reflection at the desired electron energy is achieved by selecting well and InP barrier thicknesses, d_w, and, d_b, which correspond to one quarter of the Bloch wavelength in those layers. The quarter-Bloch-wave thicknesses are defined by [Capasso et al., 1992]

$$k_w\, d_w = \pi/2$$

$$(4.1)$$

$$k_b\, d_b = \pi/2$$

where the wavenumbers k_i {i≡'w' or 'b'} are expressed by [Eq. (3.11)]

$$k_i = \frac{\sqrt{2 \, m_i^* \, (E_{max} - V_i)}}{\hbar} \qquad (4.2)$$

where V_i is the potential, and $m_i^* \equiv m_i^*(E_{max})$ is the electron effective mass.

The peak reflectivity is increased when either the number of layers [Furuya, 1992] or the depth of modulation between alternating layers [Takagi, 1991] is increased. The modulation depth

$$\frac{k_b}{k_w} = \sqrt{\frac{m_b^*(E) \, (E - V_b)}{m_w^*(E) \, (E - V_w)}} \, , \qquad (4.3)$$

is larger when deeper wells are used. However, the maximum allowable depth of these wells is limited by two physical considerations, which are presented next.

4.2.1 Maximum Well Depth

The first constraint on well depth is related to the requirement for *optical* transparency of the EBR (see Fig. 4.1). The energy of optical transitions in the EBR reflector must significantly exceed (typically, by ≥ 80 meV) the energy of the optical transition in the laser active region [Takagi, 1991]. This prevents the absorption of laser radiation by electron-hole pair generation within the EBR.

The threshold energy for optical absorption in the EBR is *lowered* for wells which are deeper. However, if deep wells are employed that are
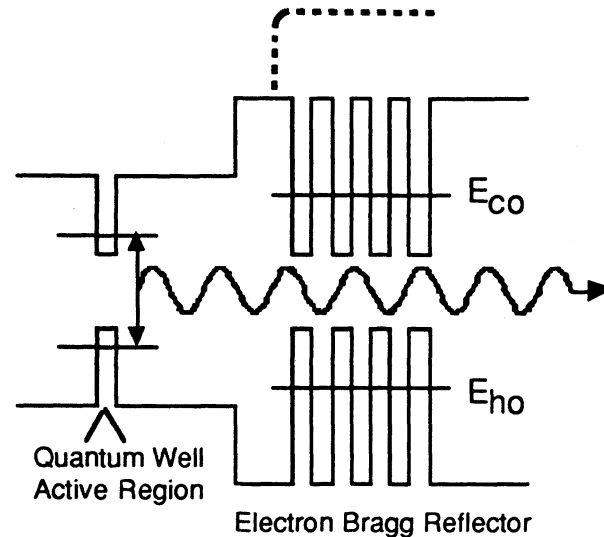
Figure 4.1: EBR optical transparency condition. The active region radiation must not be absorbed by the band to band transitions between the lowest lying electron (E_{eo}) and hole (E_{ho}) states in the multiple quantum barrier.

sufficiently thin, the quantum confinement energy can be large enough to establish a threshold optical absorption energy which exceeds the energy of optical transitions in the laser active region. Therefore, optical transparency in the EBR can be realized with arbitrarily deep wells, if these wells are sufficiently thin.

The second constraint on the maximum well depth arises from the requirement of minimizing the "lowering" of the EBR due to band-bending, (see Fig. 4.2). The band-bending results from the establishment of a flat hole quasi-Fermi level throughout the p-doped region [Takagi et. al., 1991]. The lowering worsens with increasing well depth; however, relatively deep wells can be used in practice if they are sufficiently thin [ibid.]. This is because reducing the well width (increasing the spatial confinement) situates the confined hole energy states nearer to the InP band edge, and reduces the
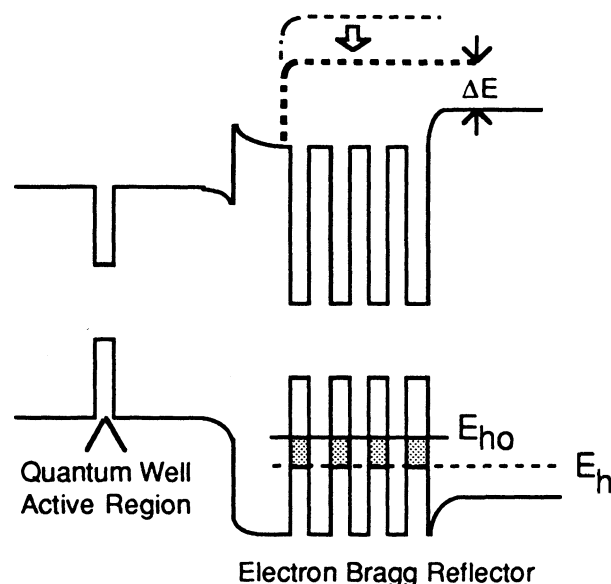
Figure 4.2 EBR lowering due to the establishment of a flat hole Fermi level, E_h, in the p-doped region. E_{ho} designates the lowest-lying valence sub-band.

number of confined hole states lying below the InP band edge. As a result, an EBR incorporating thin wells *represents less of a departure from bulk InP*, and it follows that the aforementioned band bending is reduced[1]. The use of thin quantum wells will thus serve to preserve the full barrier height, ΔE.

The band-bending is also reduced if the EBR quantum wells are strained. The fabrication of quantum wells with bi-axial compressive (tensile) strain in the plane which lies normal to the direction of crystal growth is realized by the epitaxial deposition of a semiconductor alloy whose lattice constant is larger (smaller) than the lattice constant of the substrate. A discussion of the influence of strain on the band structure of quantum wells lies beyond the scope of this thesis; however, it will suffice to note that the

---

[1] In the (trivial) limit of *zero* well width for all quantum wells in the EBR, the EBR structure is reduced to bulk InP, and there is no band-bending whatsoever.

presence of strain in the quantum well drastically reduces the density of confined hole states [Zory ed., Chap. 8, 1993]. Thus the incorporation of strain in the quantum wells of the EBR serves to minimize the band bending (and thereby retain the barrier height, ΔE) for reasons similar to those which motivate the utilization of quantum wells that are thin.

4.2.2 Chirped Grating

In addition to the benefits of a large modulation depth or period number (§ 4.2 and Eq. (4.3)), the bandwidth ΔE of the EBR can be increased by "chirping" the grating [Iga, 1986]. Chirping consists of either gradually increasing or decreasing the period or duty cycle throughout the grating. The reflectivity spectrum of a chirped grating is generally more broadband than a standard grating, because several values of electron wavelength correspond to a first-order Bragg reflection condition for some region within the grating.

In addition to bandwidth improvement, chirping also makes the performance of the EBR less sensitive to systematic or random errors in the layer thicknesses, and less sensitive to the assumptions made (during its design) regarding the numerical values for the relevant semiconductor material parameters (§ 4.4.1). Finally, chirping can be exploited to provide a mechanism that enables the grating to "reflect" electrons which have suffered inelastic collisions within the EBR (§ 4.3.2).

4.3 Design Considerations Arising from the Finite Electron Coherence Length

Coherent electron wave devices rely on the wave nature of conduction electrons; consequently, their performance is optimal for electron transport which is free of inelastic (i.e. Bloch wavelength altering) collisions. The coherence length of an electron is limited by the frequency and severity of inelastic scattering events.

4.3.1 Electron Scattering in III-V Compounds

Any deviation from the periodic potential of a semiconductor can act as a scattering centre. In III-V compounds, electron scattering is expected to be dominated by native or impurity defects, by alloy disorder (due to the pseudo-random distribution of the group III and group V atoms in the ternary and quaternary layers), and by lattice vibrations or phonons [Regianni, pp. 63-76, 1974; Boer, p. 791, 1990]. The relative importance of these mechanisms depends strongly on temperature and on material composition and quality.

Phonon-induced scattering is categorized as optical or acoustic, and subcategorized as transverse or longitudinal, according to the phonon branch and mode responsible for the scattering. Phonon-induced crystal deformations scatter electrons by causing a modulation in the conduction band potential, by establishing piezoelectric fields, or by exciting electromagnetic dipole radiation by the relative movement of cations and anions in longitudinal optical vibration modes. Theoretical and experimental work suggests that the latter, also known as polar optical phonon scattering, is the dominant inelastic process limiting the mobility of electrons in III-V compounds at room temperature and above [Wang, p.228-229, 1989]. The

limit on the coherence length of electrons due to phonons is expected to impose an upper temperature limit on the functionality of coherent electron devices.

Electron coherence lengths have been inferred for high purity MBE-grown AlGaAs/GaAs superlattices by counting the number of resolvable photoluminescence (PL) peaks[2] [Mendez *et al.*, 1990]. The observed coherence length decreased monotonically from 935 Å at T=5K to 495 Å at T=297K. The 495 Å room temperature coherence length determined for GaAs/AlGaAs has been cited [e.g. Takagi, 1991] to justify the length of EBRs which have been proposed or experimentally investigated for InGaAlP visible lasers. However, to the author's knowledge, the coherence length in InGaAlP has not been independently determined by either theory or experiment.

There is no experimental data of the type reported by Mendez *et al.*, [1990] for InGaAsP/InP superlattices [Sleight, 1993]. Krishna *et al.* [1988a and 1988b] have theoretically investigated the mean free path[3] (MFP) of electrons limited by alloy scattering, polar optical scattering, and acoustic mode scattering in several III-V compounds using a band structure obtained by the coherent potential approximation. Krishna *et al.* found that MFPs in the (100) crystal direction increased with electron energy. In InP, the MFP rises from ~150 Å at the conduction band edge to ~480 Å at 200 meV for T=300K. By comparison, the MFP for electrons in $In_{0.5}Ga_{0.5}As$ at T=300K is

---

[2]Recall that an ideal N-period superlattice will manifest N-fold splitting of the ground state. When fewer than N peaks are resolved, this indicates that scattering prevents electrons from interacting coherently with the entire superlattice. The mean coherence length is assumed to be (# of resolvable peaks) x (length of one period in the superlattice).

[3]The mean free path of an electron is defined as the mean distance traveled before any momentum and/or direction altering collision takes place. Therefore, the mean free path will be interrupted by both inelastic and elastic collisions. However, the *coherence length* is interrupted only by inelastic (wavelength altering) collisions. Therefore the coherence length invariably *exceeds* the mean free path.

larger (~210 Å at the band edge; ~1000 Å at electron energies ~200 meV), because the reductions in the MFP due to the presence of alloy scattering are offset by reduced phonon scattering[4] attributable to the smaller electron effective mass ($m^* = 0.041\ m_0$) in the ternary (*c.f.* $m^* = .077\ m_0$ for InP).

In the absence experimental or theoretical data for the full range of quaternary InGaAsP/InP compositions, it would appear reasonable to impose an upper limit on the practical length of the EBR at ~500 Å.

4.3.2 EBR Length

In order to minimize impairments to the performance of a coherent electron device due to scattering phenomena, the device should be as compact as possible. This reduces the probability that an inelastic scattering event will occur when electrons are interacting with the device. Compactness for the EBR is achieved by employing thin and deep wells, which, fortuitously, is commensurate with previous design considerations (§ 4.2.1).

4.3.3 Chirping

As noted in § 4.2.2, chirping simultaneously increases the EBR bandwidth and relaxes fabrication tolerances. Moreover, scattering-related performance impairments can be reduced by exploiting chirping. Specifically, chirping is employed for the first time to provide a mechanism for the return of inelastically scattered hot electrons toward the active region.

Figure 4.3 illustrates that the scattered electron return mechanism is achieved by the placement of the EBR directly adjacent to the separate

---

[4] Manifested through a reduction in the magnitude of the scattering matrix elements.
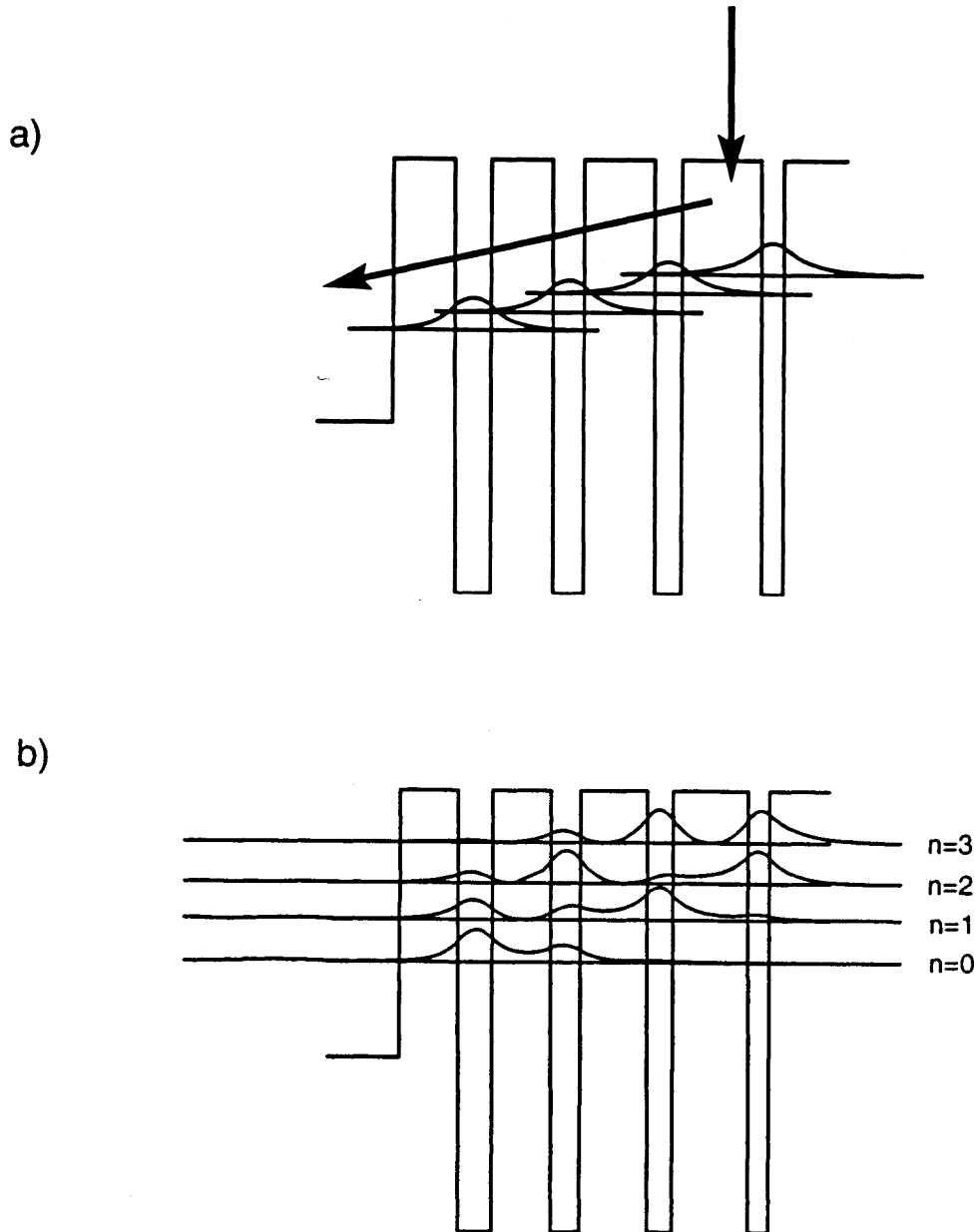
Figure 4.3: Mechanism for the recovery of inelastically scattered electrons: (a) Basic successive relaxation concept; (b) Actual, quasi-bound electron state probability distributions. Note the migration toward the separate confinement region with decreasing electron energy. All four states have lifetimes of ~.5 ps to 1 ps within the wells, after which the electron is expected to have escaped to the left. There are no bound states.

confinement region, with the quantum well thickness decreasing with increasing depth into the InP cladding. As illustrated in Fig. 4.3(a), the electron return process can be understood as a successive relaxation of the electron energy, which results in a cascading of the particle down toward the separate confinement region. This rudimentary picture is substantiated in Fig. 4.3(b), which shows the evolution of the calculated probability distribution $|\psi(x)|^2$ when the particle energy is decreased. Since all four electron states are quasi-bound (see § 3.2.6), it is expected that the electrons in these states will escape into the active region after a brief time. The calculated state 1/e lifetimes (using Eq. (3.24)) range from ~.54 ps to 1.01 ps.

It is natural to speculate that the electrons traveling back toward the separate confinement region may relax from their quasi-bound states into low energy *bound* electron states within the EBR, where they would presumably remain trapped until they recombine with a hole. However, electron-hole recombination in the EBR is minimized by relying upon an eigenstate exclusion phenomenon which has not been previously exploited. The EBR design in fact "cuts off" *all bound electron states* in a manner analogous to the cut-off of all guided optical modes in asymmetric optical guides. This represents the identification and the first fabrication of a multiple-quantum well design that is expected to achieve this "cut-off" phenomenon. The cutoff condition is manifest in the absence of zero crossings in the eigenvalue equation for real valued eigen-energies spanning the well depth.

Thus, the EBR supports only the short-lived (~.5 to 1 ps) quasi-bound modes which accommodate the transport of electrons back into the separate confinement region. The absence of a truly bound (long lifetime) eigenstate for electrons is expected to drastically reduce the rate of electron-hole recombination in the EBR.

4.4 Nominal EBR Design

The EBR was designed by using the transfer matrix method presented in Chapter 3. The layer sequence is enumerated in Table 1. It consists of four 1.5% compressively strained wells which decrease in thickness with increasing depth into the upper InP cladding. For ease of fabrication, and to preclude the requirement for additional calibration growths, the EBR wells have the alloy composition of the active region. Because the wells are thinner than the active region quantum well and because they are bound by InP, the condition of optical transparency (section 4.2.1) is amply fulfilled.

Table 4.1. Nominal EBR Design.

Layer Number	$In_{(1-x)}Ga_x$ x	$As_yP_{(1-y)}$ y	$\Delta a/a$	Band Gap Energy (eV)	Thickness (monolayers)
-	.254	.540	0	0.992	-
1	0	0	0	1.35	40 A (14)
2	.154	.803	-1.52 %	0.71	23 A (8)
3	0	0	0	1.35	40 A (14)
4	.154	.803	-1.52%	0.71	20 A (7)
5	0	0	0	1.35	46 A (16)
6	.154	.803	-1.52%	0.71	17 A (6)
7	0	0	0	1.35	51 A (18)
8	.154	.803	-1.52%	0.71	14 A (5)
-	0	0	0	1.35	-

4.4.1 Insensitivity of EBR Performance to Material and Fabrication Parameters

Figure 4.4(a) shows the probability of electron reflection, R, as a function of electron energy, E, above the InP conduction band edge for the nominal design. The calculation is based on the TMME using Eq. (3.20), and includes conduction band non-parabolicity through Eq. (3.5). The dashed

curve represents the reflectivity assuming parabolic bands. The disparity suggests that calculations of EBR reflectivity bandwidth based on parabolic bands [e.g. Iga, 1986; Takagi *et al.*, 1991; Furuya *et al.*, 1992] may be overly optimistic.

Figure 4.4(b) shows the R vs. E curves when the band edge effective mass in all layers is increased or decreased by 8%. Figure 4.4(c) illustrates the influence of different relative partitionings of the heterojunction band offsets between the conduction and valence bands.

The influence of thickness errors are revealed in Fig. 4.5. Figure 4.5(a) and 4.5(b) show R vs. E under the assumption of a systematic +1 or -1 monolayer error and a +10% or -10% offset in the layer thicknesses (rounded to an integral number of monolayers), respectively. Figure 4.5(c) represents the calculation of R vs. E for ten cases in which the layer thicknesses have all been randomly modified by uncorrelated errors of up to ±2 monolayers.

The calculations for Figs. 4.3 and 4.4 assess the electron reflection spectrum under the influence of independent EBR uncertainties or errors. For a combination of two or more uncertainties or errors (e.g. incorrect band offsets combined with uncorrelated layer thickness fluctuations) the bandwidth may be reduced significantly. It is also important to recognize that, although theoretical models suggest that lasers operate with nearly flat-bands above threshold [e.g. Lee *et al.*, 1993], finite band curvatures (including the deleterious EBR-sagging; see § 4.2.1) will affect EBR performance.
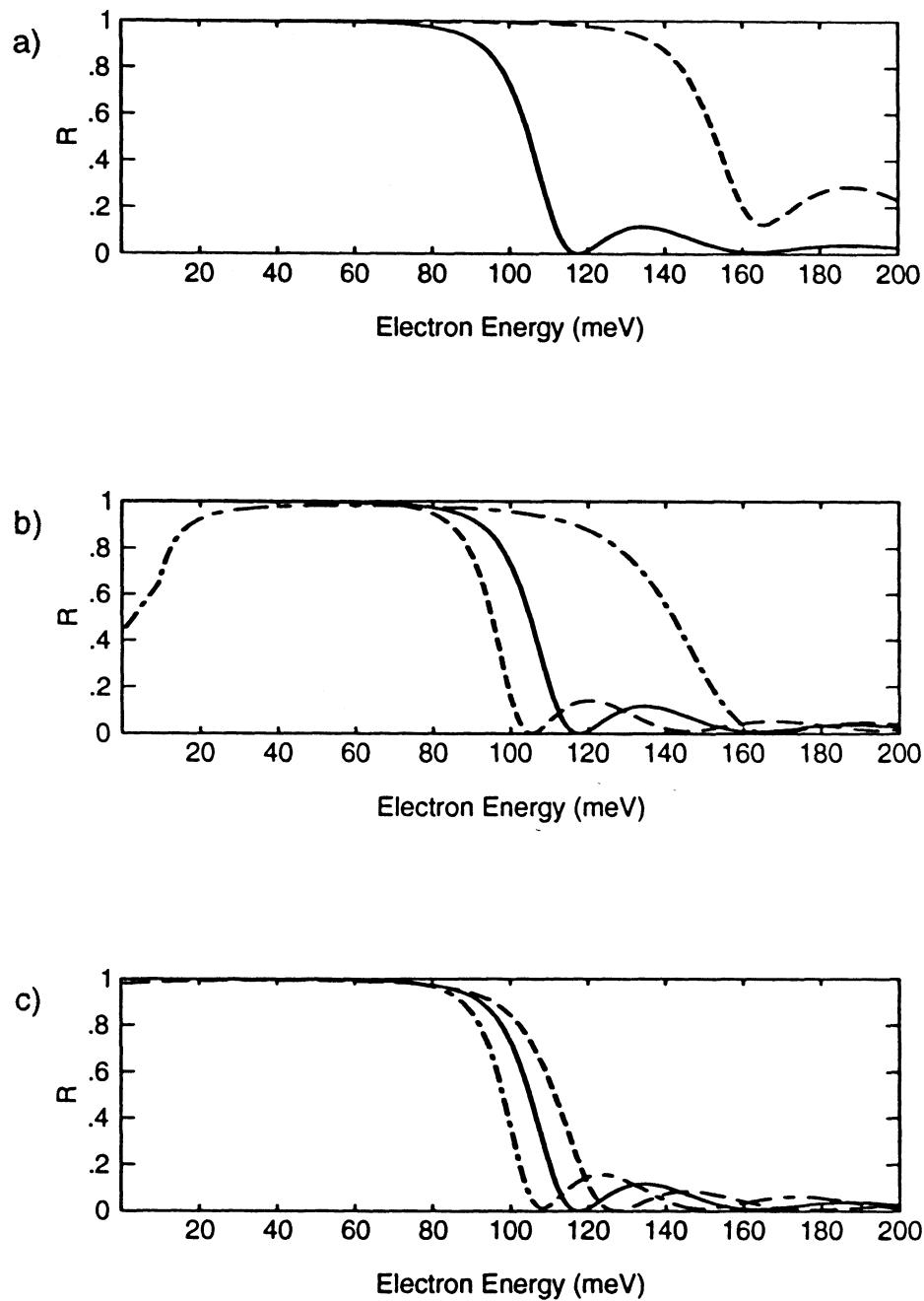
Figure 4.4: EBR reflectivity vs. electron energy; influence of material parameters. Solid line is for nominal material parameter values. Other curves shown are for (a) parabolic bands (dashed); (b) 8% increase (dashed) or decrease (dot-dashed) in the band-edge effective mass; and (c) heterojunction band discontinuity partitioning between conduction and valence bands in the ratio 33:67 % (dashed) and 45%:55% (dot-dashed); nominal value is 39%:61% [Forrest *et al.*, 1984].
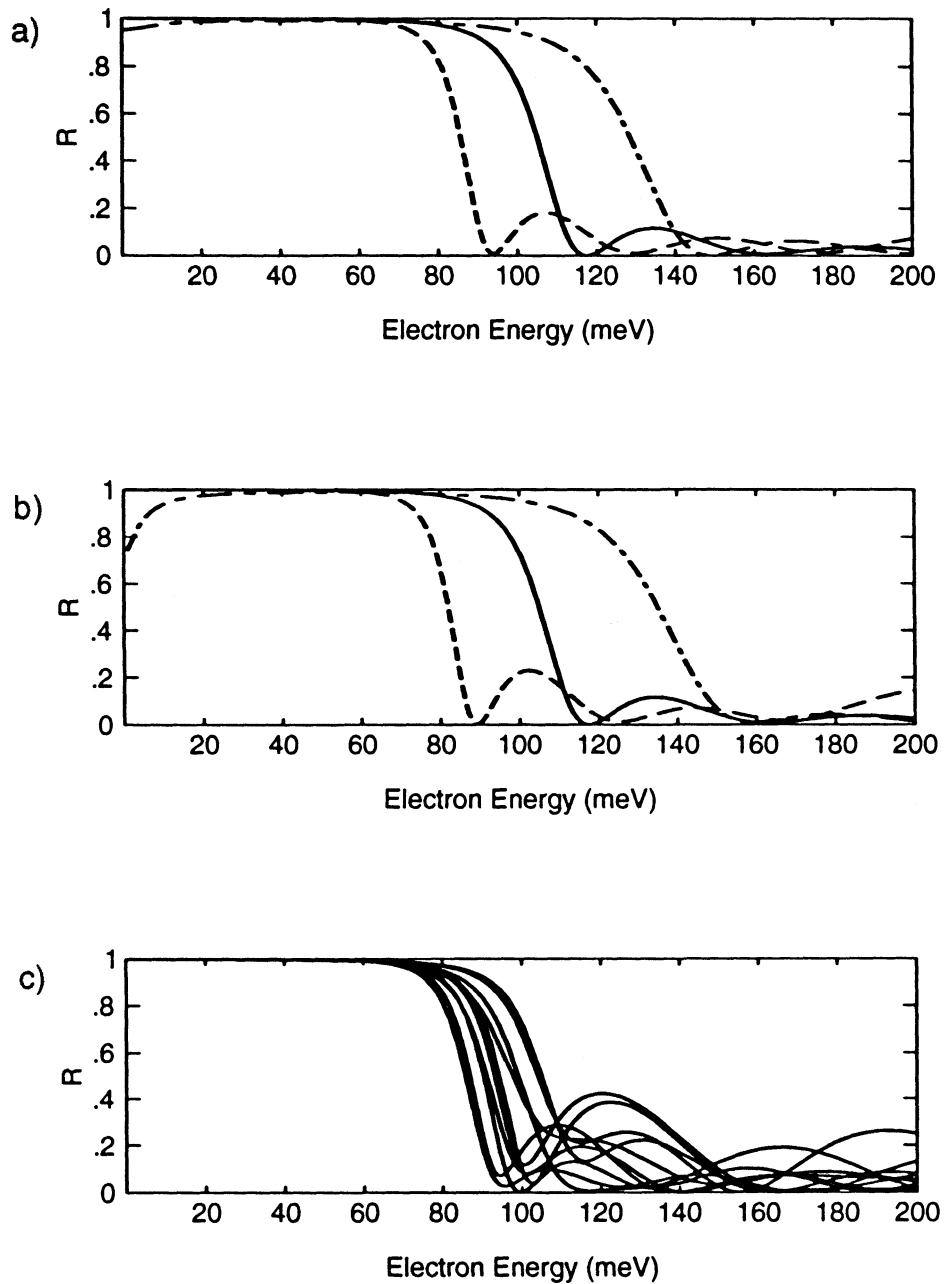
Figure 4.5: EBR reflectivity vs. electron energy: influence of errors in the layer thicknesses. Solid line in (a) and (b) is for the correct layer thicknesses. Other curves correspond to (a) systematic offset of +1 (dashed) or -1 (dot-dashed) monolayers for all layers; b) systematic 10% increase (dashed) or decrease (dot-dashed) in thickness of all layers; and (c) uncorrolated random fluctuation of ±2 monolayers for all layers (10 cases).

Chapter 5: Laser Fabrication

5.1 Introduction

To explore the advantages provided by an EBR, two ridge waveguide lasers (one with a EBR, and one without) were fabricated. In this chapter, the specific laser designs and their fabrication are briefly described, and the mounted laser assembly is presented.

5.2 Layer Growth Sequence

The epitaxial layer growth sequence for the control laser and the EBR-equipped laser are represented in Figs. 5.1 and 5.2, respectively.

The active region (layer #3 in both designs) is a single 55 Å wide $In_{.154}Ga_{.846}As_{.803}P_{.197}$ quantum well. The alloy composition of the well corresponds to an equilibrium lattice constant of 5.993 Å (according to Vegard's law [e.g. see Adachi, 1982]), or ~1.52% larger than the lattice constant of the surrounding alloy, which is lattice matched to InP. The quantum well is expected to accommodate the lattice mismatch elastically through bi-axial compressive strain.

The total optical transition energy in the well (~.8 eV, giving λ~1.55μm) is the sum of the confinement energies of the lowest lying

Composition   Thickness   Doping

Layer #17	InGaAs	0.2 μm	Zn: 1E19	P Contact Layer
Layer #16	InP	1.2 μm	Zn: 1E18	
Layer #15	InP	.20 μm	Zn: 4E17	
Layer #14	1.3Q Etch Stop	50 Å	Zn: 4E17	
Layer #13	InP	225 Å	undoped	
Layer #4	1.25 Q	1700 Å	Si: 4E17	
Layer #3	1.5% Strained Q	55 Å	Si: 4E17	Active Region
Layer #2	1.25Q	1700 Å	Si: 4E17	Separate Confinement Layers
Layer #1	InP buffer	1.5 μm	Si: 2E18	
Substrate	InP		n+	

Figure 5.1: Layer growth sequence for the single quantum well (control) laser. 1.3Q refers to a quaternary layer with a band gap corresponding to 1.3 μm optical emission for bulk material.

Figure 5.2: Layer growth sequence for the electron Bragg reflector equipped single quantum well laser. 1.25Q and 1.3Q refer to quaternary layers corresponding to 1.25 and 1.3 μm optical emission (see Table 4.1 for actual alloy compositions). The layers in the EBR indicate the target number of monolayers (ml) adjacent to the specification in Angstroms.

electron and hole states (~0.06 eV and 0.03 eV, respectively.[1]), and the band gap energy (~.71 eV), which is increased relative to its unstrained value of[2] ~.64 eV by the hydrostatic component[3] of the strain.

The two 1700 Å or 1650 Å wide, larger band gap (~.992 eV) $In_{.154}Ga_{.846}As_{.803}P_{.197}$ layers (#2 and #4 for both designs) adjacent to the active region define the separate confinement region. This region has a dual purpose of confining the optical power and the injected electrons and holes (§ 2.2) in the vicinity of the laser active region.

The separate confinement region is Silicon doped (n-type) to $4 \times 10^{17}/cm^3$. Both structures have undoped regions which are ~250 Å wide between the n- and p-doped regions. The Zn (p-type dopant) is expected to diffuse across these undoped regions during growth and processing. As a result, the p-n junction in both devices is expected to be located approximately where the profile of Si terminates (see § 5.5).

During laser operation, hole transport to the active region is expected to be achieved by diffusion across the n-type separate confinement layer from the anisotype heterojunction (at the interface of layers #4 and #5 in both designs). Because the mobility of holes is ~1/10 the mobility of electrons [e.g. see Hayes et al., 1982], the increase in threshold due to lateral hole current spreading in the active region is expected to be reduced in comparison to the converse case of electron injection into a p-type separate confinement region.

---

[1]Calculated from Eq. (3.23).

[2]See Appendix A.

[3]Bi-axial strain can be modeled as the superposition of a hydrostatic and a uni-axial strain. The former induces an increase (decrease) in the band gap for compressive (tensile) strain. Also see Appendix A.

The two structures were designed to achieve identical (~3%) relative confinement of the optical mode within the laser active region.

5.3 Device Fabrication, Selection, and Assembly

The laser structures were grown onto sulfur (n-type) doped ~5 cm diameter Sumitomo substrates in a Metal-Organic-Chemical-Vapor-Deposition (MOCVD) reactor at the Advanced Technology Laboratory of Bell-Northern Research (BNR) in Ottawa. The wafers were then subjected to a ridge-waveguide laser process which yielded ~2 μm wide ridges with blanket p-side and n-side metal contacts.

Figure 5.3 provides a brief summary of the ridge waveguide fabrication process. After cleaning the grown wafer surface and coating it with SiO_2, the ridge and mesa topology was realized in the SiO_2 by photolithography. The ridges and mesas were then defined by a combination of reactive ion etching and wet chemical etching down to the InGaAsP etch-stop layer. Next, the remaining SiO_2 was removed and a new blanket SiO_2/SiN_x dielectric coating was deposited. Photoresist was then patterned to expose only the ridges, where the SiO_2/SiN_x was removed to expose the p-contact layer. Blanket Ti/Pt/Au was then evaporated onto the p-side. The wafer was then thinned and polished down to a thickness of ~150 μm, after which a blanket evaporation of Ni/Ge/Au was applied to the n-side.

a) Patterning of SiO₂ by photolithography

SiO₂
P-contact layer
Etch-stop layer
Laser active area
(white areas = InP)
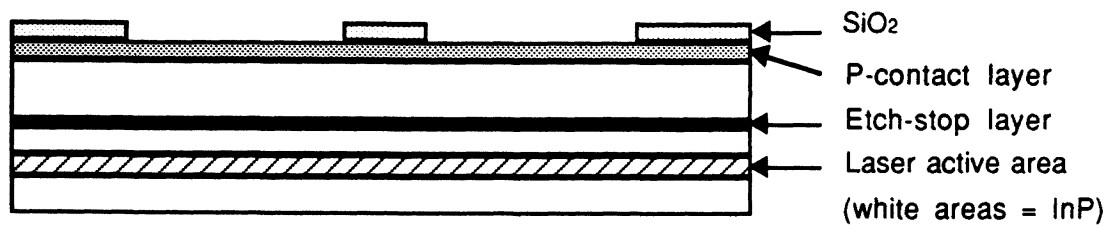
b) Reactive Ion Etching, wet etching, removal of SiO₂

Mesa   Ridge ← 2 μm   Mesa
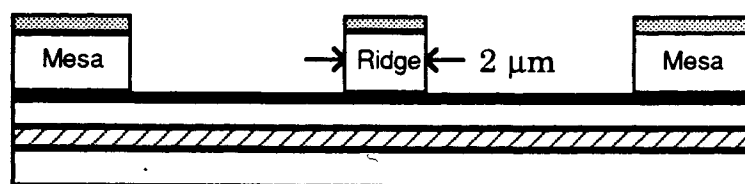
c) Blanket SiO₂/SiNx, via to ridge by photolithography and wet etch.

Ridge via

SiO₂/SiNx
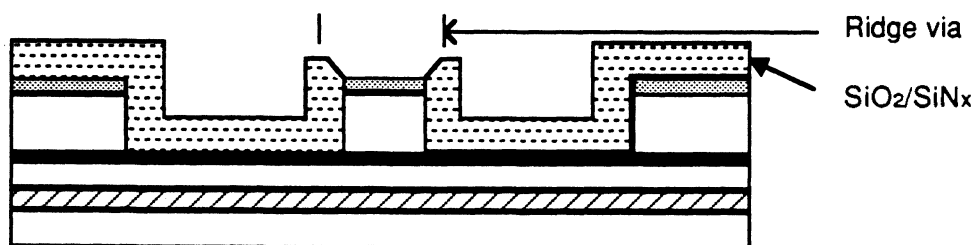
d) Deposition of p metal contact, substrate lap and polish, n metal contact

P metal (Ti/Pt/Au)

N metal (Ni/Ge/Au)
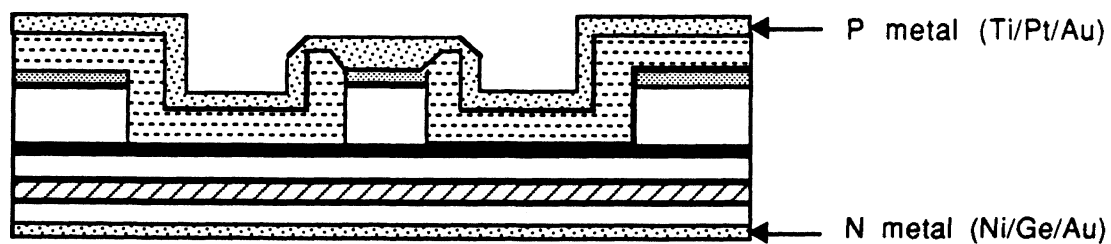
Figure 5.3: Summary of ridge-waveguide laser fabrication.

The thicknesses of the dielectric and metal layers deposited in the fabrication process were designed to result in minimal stress in the laser active region. However, high sensitivity degree-of-polarization (DOP) photoluminescence has revealed circular bands of tensile strain on the order of ~0.1% emanating from the apexes in the metal at the base of the ridges and mesas [Cassidy et al., 1993].

Approximately 100 control lasers and EBR-equipped lasers were cleaved from the wafers into 1500μm lengths. The ten control and ten EBR-equipped lasers which exhibited the highest differential quantum efficiency[4] among their respective lots were selected.

The lasers were bonded with the ridge-side up onto gold-plated SiC heat sinks (using 80% Au/20% Sn solder), which were in turn soldered to Au plated copper blocks. The copper blocks were cemented to a ceramic sub-carrier with Au bonding pads. The complete mounted-laser configuration is detailed in Figure 5.4.

Laser (1500 x 381 x 150 μm)

SiC Heat Sink
(1.5 x 1.5 x .4 mm)

Au wire
(25 μm diameter)

Au plated
Cu block
(6.35 x 3.3 x .84 mm)

Au Bond pad

Ceramic
Substrate
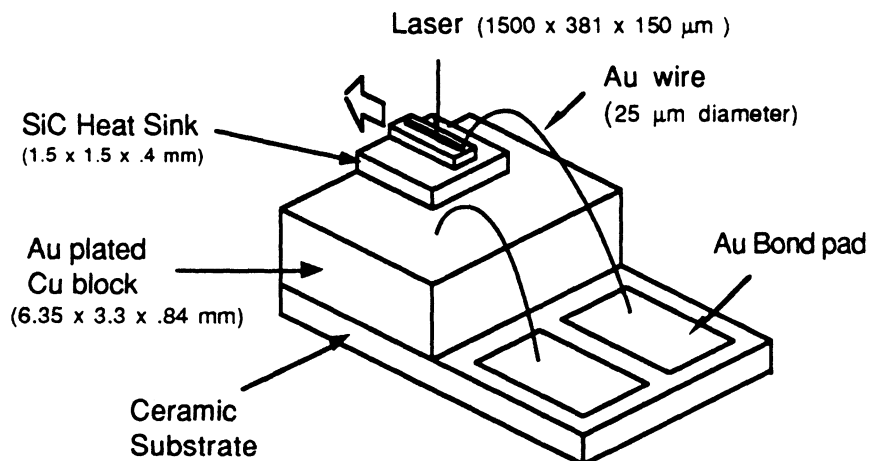
Figure 5.4: Mounted laser assembly.

[4]Under pulsed operation (0.1% duty cycle, 300 ns pulses) at room temperature.

5.4 Process Diagnostics

A compressive strain of 1.3% to 1.5% was estimated for the quantum wells in both laser structures on the basis of the x-ray double crystal diffraction analyses of the relevant calibration growths.

A profile of the zinc and silicon concentrations in the EBR-equipped laser was obtained by Secondary-Ion-Mass-Spectroscopy (SIMS) and is shown in Figure 5.5. These profiles were measured from a sample which had been etched down to the etch-stop layer. The enhanced Si signal near the surface was deemed by the operator to be an artifact caused by the detection of negatively ionized surface impurities whose molecular mass is comparable to the atomic mass of the Si 28 isotope. Typically there is very little diffusion of Si during fabrication. It will be assumed in this thesis that the Si dopant profile matches the growth request.

In contrast, Zn is detected by the collection of positively charged ions, and the relative yield for unwanted positively-charged surface impurities is comparatively small. Therefore, the measured Zn trace is assumed to be accurate, which implies that the zinc has diffused during fabrication. An inspection the Zn concentration relative to the gallium trace indicates that the quantum barrier region has become p-type, and that the p-n junction is located at or near the interface between the quantum barrier and the separate confinement region (i.e., at the interface between layers 4 and 5 in Fig. 5.2).
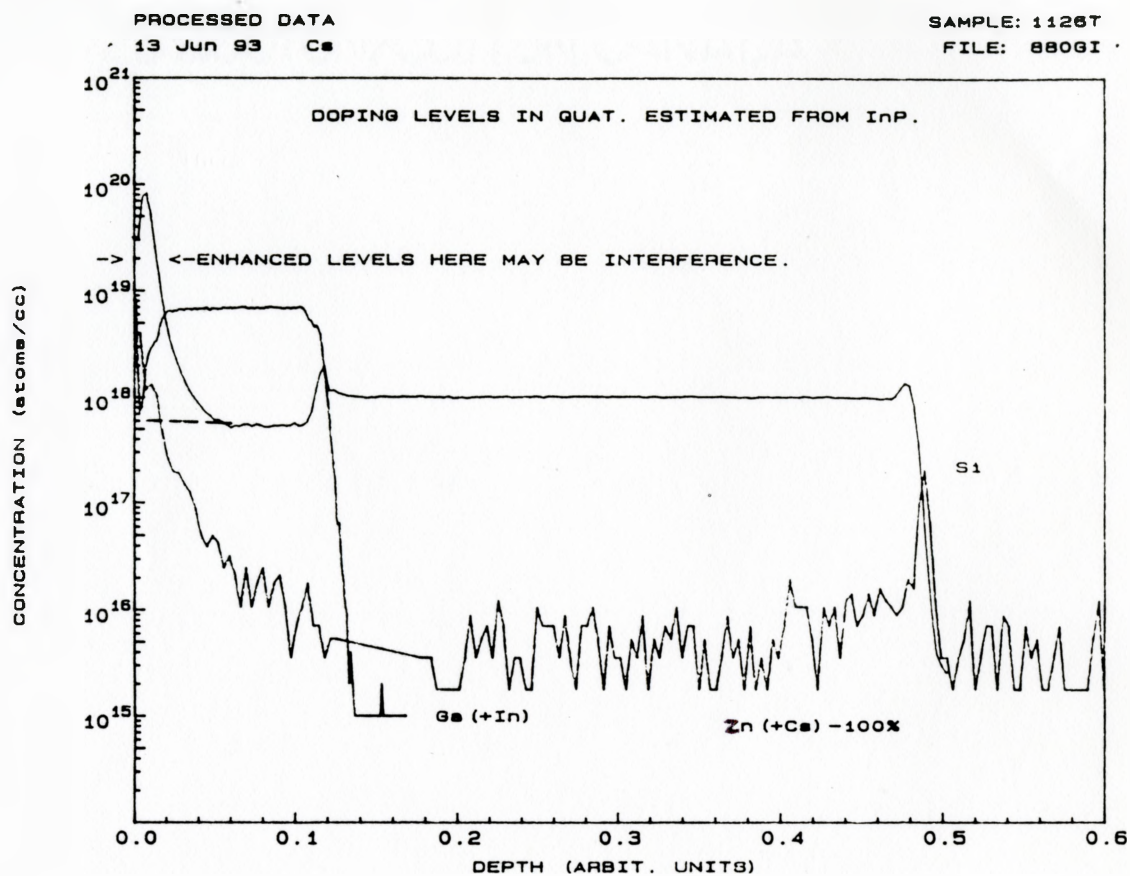
Figure 5.5: SIMS profile of the concentration of zinc and silicon, and the relative concentration of gallium. The dashed line illustrates the assumed profile of silicon (see text). This profile was obtained from a Cameca 4F SIMS spectrometer.

Chapter 6: Experimental Apparatus and Procedures

6.1 Introduction

The experiments which were performed for this thesis were designed to quantify the temperature dependence of laser threshold current (I_{th}), the electro-luminescence (EL) spectra, and the relative external differential quantum efficiency, between $T=\sim 19$ K and $T=320$ K. A comparison of the temperature dependence of the output characteristics for EBR-equipped and control lasers will be presented and interpreted in Chapter 7.

In this chapter, the experimental apparatus and procedures which were used for data acquisition are described. Unless otherwise indicated, all electronic equipment were remotely configured (through an IEEE-488 bus) by an 80286 processor based computer. *In-situ* operational data (i.e. laser drive current, temperature, etc.), and data from electronic or optical detection equipment, were collected automatically through the data bus and stored into ASCII files. Several software routines based on the IEEE-488 interface protocols were written or modified to drive equipment configuration, data acquisition, and data storage. Computer control was necessary in light of the repetitive nature of the measurements and the inexorable delays between measurements, which were due to the wait time for laser temperature stabilization.
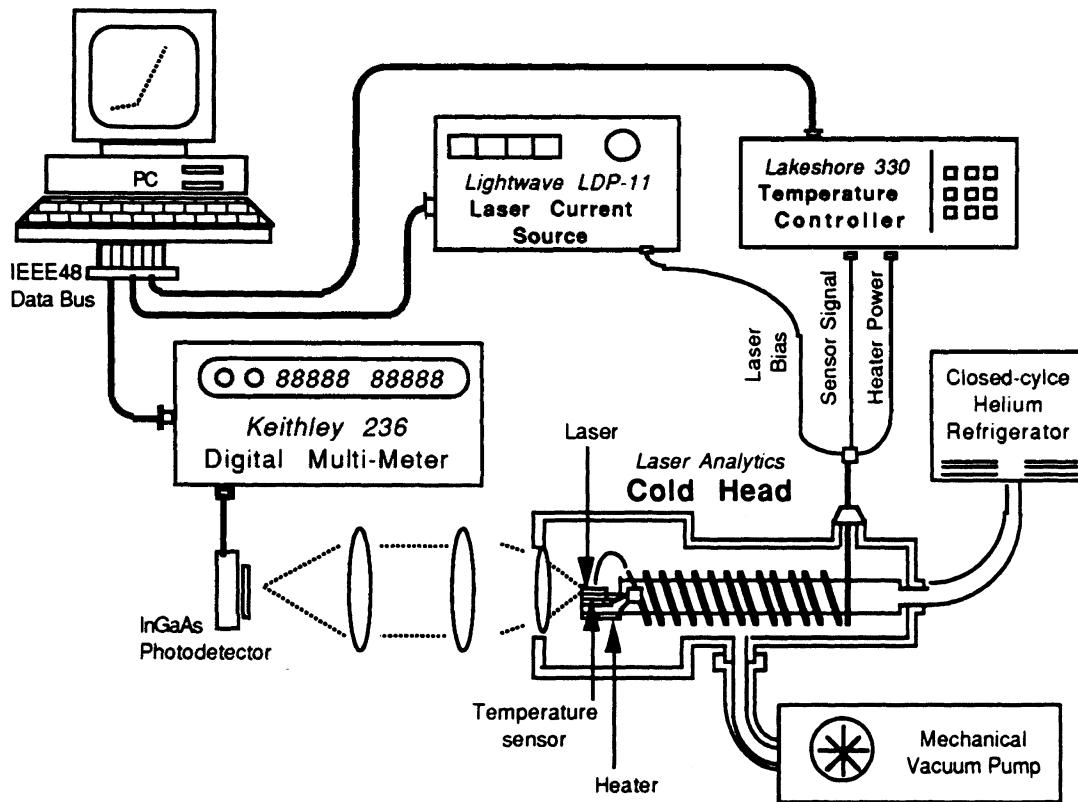
Figure 6.1: Experimental set-up for acquisition of the laser light vs. current as a function of temperature

6.2 Experimental Setup

Figures 6.1 and 6.2 illustrate the experimental set-up for the acquisition of the temperature dependence of the light vs. current data and the EL spectra, respectively.

The main functional components were: 1) the laser temperature control unit, which includes the cold-head and the temperature controller; 2) the laser current source and optical measurement apparatus.
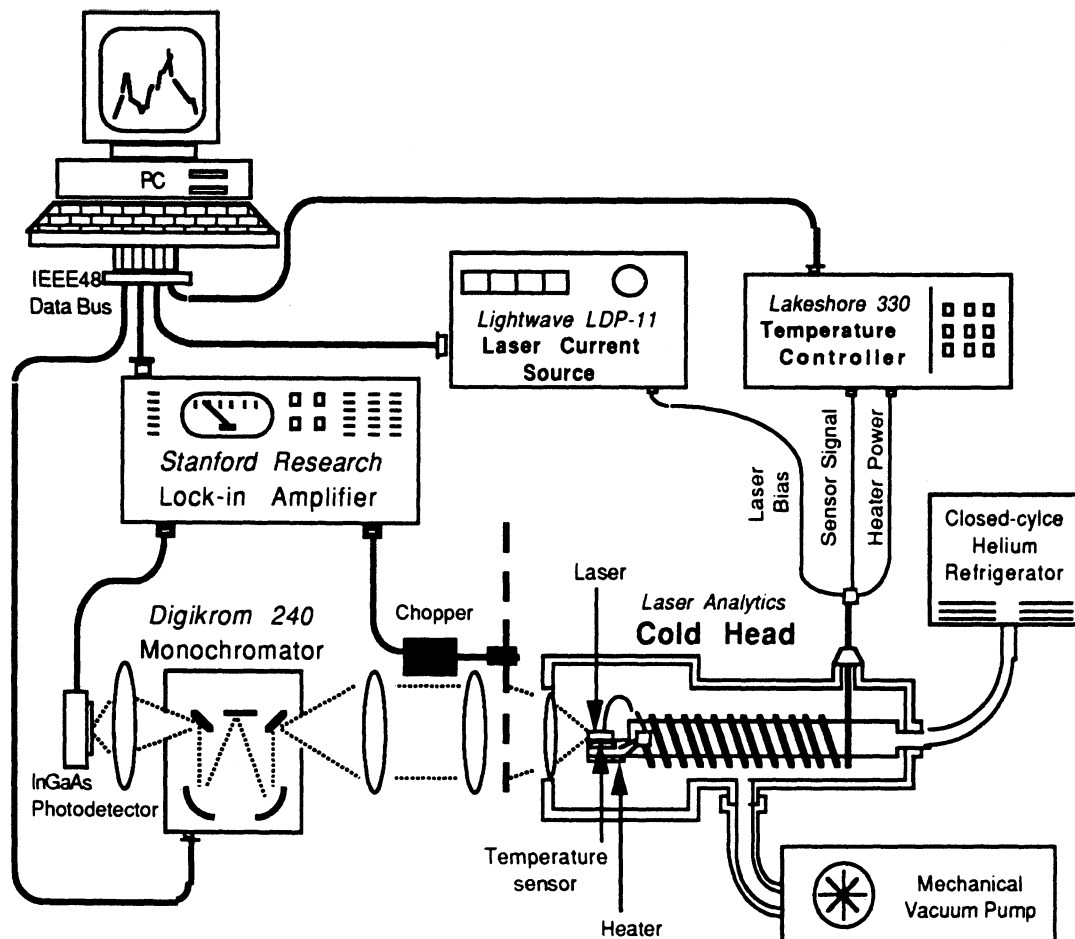
Figure 6.2: Experimental set-up for the acquisition of laser electroluminescence spectra as a function of temperature and bias current.

6.3 Sample Temperature Control

The main requirement for the investigation was the control of the temperature of the lasers throughout their operational range, the bulk of which lies below room temperature.

The control of laser temperature was achieved by placing the mounted laser assembly into the chamber of a Laser Analytics closed-cycle helium-circulating cold-head. A low volatility thermally conducting

compound was applied to the base of the ceramic sub-carrier to ensure good thermal conductivity between the cold head sample platform and the laser assembly. After an evacuation ($\leq$ 60 mTorr) of the chamber to avoid atmospheric condensations, the cold-head sample platform was refrigerated continuously, attaining a minimum temperature of ~19 K. The Lakeshore Model 330 autotuning temperature controller could then establish and stabilize the temperature of the sample platform to any desired temperature >19K by providing the appropriate current to a resistive heater located in the cold head platform. The heater current supplied by the Lakeshore 330 was determined by a feedback loop based on a silicon diode temperature sensor situated within the cold-head sample platform. Measurements of laser output were not initiated until the Lakeshore achieved the target temperature with a stability better than ±0.1 K for a period of eight minutes.

The temperature control algorithm in the Lakeshore 330 is based on the characteristic response data of the silicon diode sensor, which was supplied by the manufacturer and loaded into the memory of the Lakeshore 330. The response curve is claimed by the manufacturer to be provide *absolute* temperature estimates which are accurate to within ±1 K in the range 10 - 300K. However, the *difference* between two temperature readings is expected to be more accurate, and the temperature reproducibility (i.e. the ability to achieve the same sample temperature in separate investigations) is expected to be excellent ($\leq$ ±0.1K).

It is emphasized that both the excellent temperature repeatability and the accurate assessment of *differences* between temperatures are the two most important requirements for the comparison of the temperature dependence of the operating characteristics of the two laser structures.

6.4 Laser Current Source

Laser driving current was provided by a high precision ILX Lightwave Technologies model LDP3811 laser diode pulser. The LDP3811 could be programmed to drive the laser with a continuous current, or with pulses of constant current having a specified time duration and duty-cycle.

A measurement of I_{th} vs. T in an EBR-equipped laser sample was obtained for both continuous and pulsed current operation (500 ns pulses at a duty cycle of 0.1%)[1] to estimate the relative heating in the laser active region under continuous operation. The displacement between the pulsed and DC I_{th} vs. T curves along the temperature axis suggests that the temperature of the active region under continuous current injection is approximately 10K warmer than its temperature under low-duty-cycle pulsed operation. This finding is consistent with the theoretical model advanced by Martin *et al.* [1992] and with experiments performed by Evans [1992]. All other measurements of the laser characteristics were performed with continuous current injection.

6.5 Optical Measurement

For the measurement of the light power vs. current, the light emanating through the cold-head window was manually focused onto a broad area (radius=2000μm) EG&G InGaAs p-i-n photodiode. Manual alignment was rapid and repeatable, and the signal strength was sufficient

---

[1] The detected voltage was fed into a Stanford systems SR250 gated integrator-boxcar averager to convert the pulsed signal to a DC output, which was required by the Keithley 236 digital multi-meter.

at unity voltage gain to preclude the requirement for lock-in based detection and amplification.

For the measurement of the electroluminescence spectra, the laser light was passed through a Digikrom 240 monochromater prior to detection. The Digikrom 240 incorporates a Crzeny-Turner rotating grating configuration, where the grating is ruled for peak efficiency at $\lambda=1.55\mu m$.

The weak signal detected by the InGaAs photodiode during the acquisition of spectra required amplification by lock-in detection. The InGaAs detector voltage was input to a Stanford Research Systems SR510 lock-in amplifier, with a phase reference provided by a mechanical chopper placed adjacent to the cold-head window. The phase and gain setting for the SR510 were automatically adjusted *in-situ* for peak signal strength.

6.6 Leakage Measurement

The magnitude of the leakage current is assessed by light detected between $\lambda=.90$ and $.97\mu m$, which is attributable to electron-hole recombination in the InP cladding. At room temperature, the leakage signal can be very weak, even for a laser biased at several times threshold. Therefore, low noise and high sensitivity optical detection was required.

Leakage measurements were conducted on an independent experimental setup designed by J. Evans and T. Vetter. The setup was based on an optical bench to provide vibrational isolation, but was otherwise very similar to the EL spectra set-up shown in Fig. 6.2. The main differences were in the method of optical detection and temperature control.

High sensitivity optical detection was provided by a reverse-biased EG&G Silicon avalanche photodiode configured with a transistor and

resistor network to achieve a voltage gain of $\sim 10^6$. Spectral selection was provided by a Thermo Jarrel Ash MonoSpec/50 monochromater. The detector signal was amplified by a Stanford Research Systems SR550 preamplifier before it was input to a SR510 lock-in amplifier.

Temperature control was achieved by Peltier thermo-electric coolers driven by an ILX Lightwave Systems model LDC-3722 laser diode controller. The sample was placed onto an open platform which was in thermal contact with the Peltier coolers. The exposed sample platform accommodated a lens configuration which collected laser light with greater efficiency than the light collection from a laser within the cold head chamber. However, the absence of environmental isolation of the sample limited the lower temperature to the dew point, which was typically 10° below room temperature.

It was not possible to measure accurate leakage spectra from lasers refrigerated within the cold head due to the smaller leakage signals at low temperatures (§ 2.2) combined with the limited light collection efficiency and noise penalty due to vibration caused by the compressor for the closed-cycle Helium refrigerator.

6.7 Data Acquisition

For each laser under investigation, the EL spectra were collected at 40K increments from T=20K to T=260K, and at T=280 K. Light vs. current data was collected at 5 K increments from T=20K to T=300K. Leakage measurements were conducted at room temperature. The data is presented and analyzed in Chapter 7.

Chapter 7: Experimental Results for EBR-Equipped and Control Lasers

7.1 Introduction

In this chapter, the temperature dependence of the threshold current, differential quantum efficiency, and electroluminescence spectra for the EBR-equipped and control lasers are described. The data presented reveal unusual performance characteristics for the EBR-equipped lasers *which are not attributed to a reduction in hot electron leakage*. The peculiarities are collectively interpreted by a physical model. The proposed physical model is then substantiated by numerical simulations.

7.2 Experimental Results

7.2.1 Threshold Current vs. Temperature

The control lasers achieved CW operation up to $T \approx 330$ K. By comparison, the maximum temperature for CW operation for the EBR-equipped lasers was ~310 K. Moreover, the threshold currents (I_{th}) for the EBR-equipped lasers were larger than I_{th} for control lasers by at least 2 mA at all temperatures, and the efficiency was inferior. However, the EBR-equipped lasers revealed an unexpected threshold current temperature dependence, and superior threshold current temperature stability over a

a)

b)
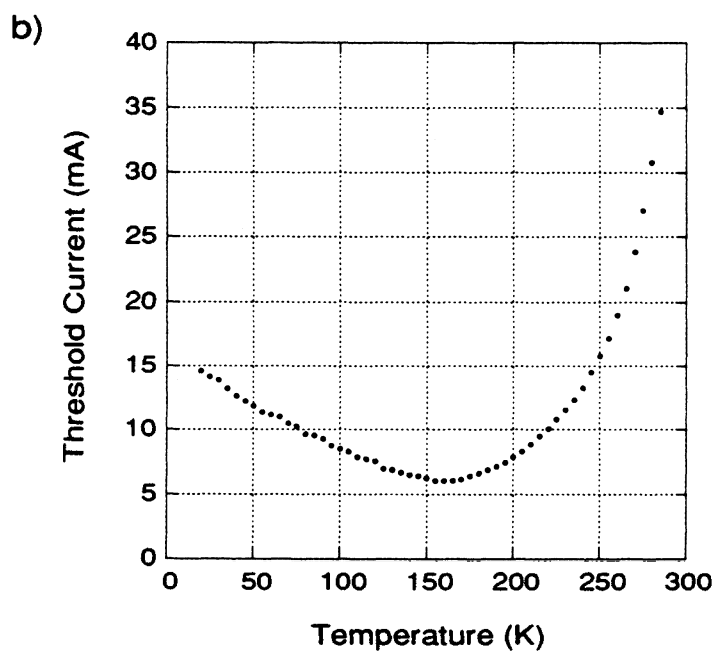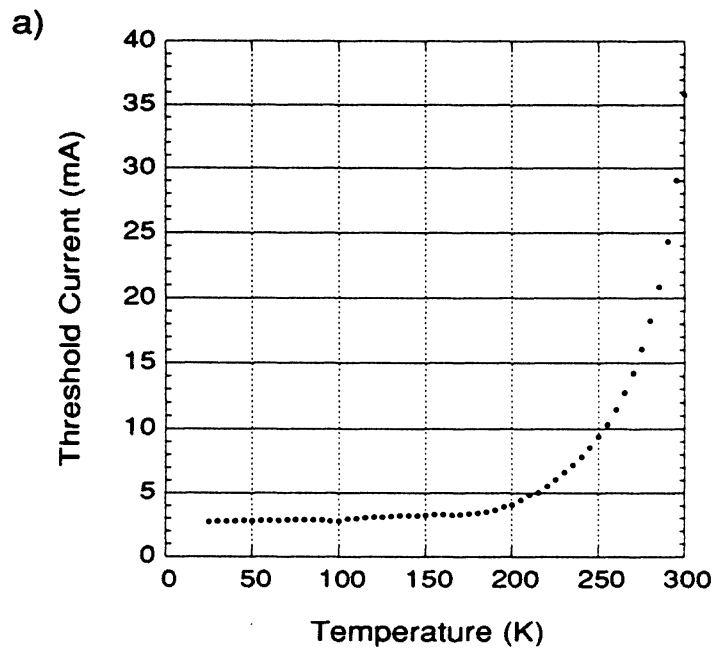
Figure 7.1: CW threshold current as a function of temperature for (a) a control laser and (b) the EBR-equipped laser.

70 K window in the operational temperature range. Plots of I_{th} vs. laser temperature (T) for a control laser and an EBR-equipped laser are shown in Fig. 7.1 (previous page).

It is seen that the control laser exhibits an approximately exponential increase of I_{th} with temperature. This is consistent with previous findings for bulk and quantum well lasers (e.g. see Agrawal et al., p.128 and p.402, 1986, and § 2.5, Eq. (2.4)). In contrast, the EBR-equipped laser exhibits a remarkable departure from the normal functional dependence of I_{th} upon temperature; I_{th} initially *decreases* monotonically with increasing temperature, until it reaches its minimum at $T \approx 170K$ ($\equiv T_{min}$), where it is less than half the value of I_{th} at $T \approx 20K$. The threshold then rises in the normal (approximately exponential) manner for $T > 170K$. All EBR-equipped lasers manifested an anomalous I_{th} vs. T behaviour similar to that depicted in Fig. 7.1(b), attaining threshold minima between $T=150K$ and $T=200K$.

The relative temperature sensitivity of the threshold current for the control laser and EBR-equipped laser are revealed in the plot of their characteristic temperature, T_o, (§ 2.5) in Fig 7.2. For the control laser, T_o is always positive, reflecting the continuous increase in I_{th} with temperature. For the EBR-equipped laser, the decrease of I_{th} from T=20K to T=170K ($\equiv T_{min}$) is reflected in a *negative* value of T_O over that temperature range. At T_{min}, T_O is infinite (because $\partial I_{th} / \partial T = 0$), and for $T > T_{min}$, T_O is positive. The shaded band in Fig. 7.2 designates the 70 K temperature window where the threshold current is more stable for the EBR-equipped laser than for the control laser.
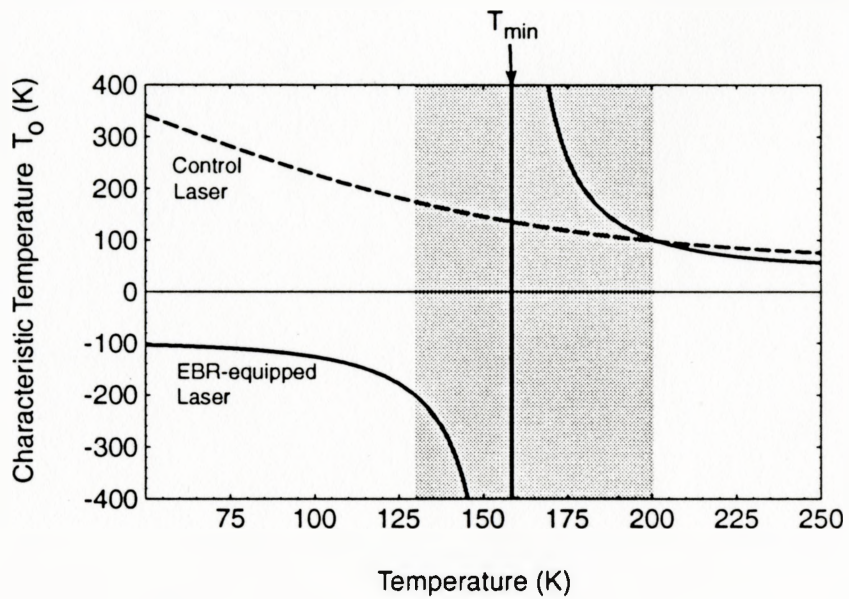
Figure 7.2: T_O vs. temperature for an EBR-equipped laser and a control laser from T=50K to T=250K. The data was obtained by applying Eq. (2.5) to an analytical fit to the I_{th} vs. T data presented in Fig. 7.1. The analytical fit is described in Appendix A.1.

7.2.2 Differential Quantum Efficiency

The differential quantum efficiency (DQE) is the efficiency with which the above-threshold current generates output optical power, and it is therefore proportional to the slope of the light vs. current curve[1] at a given current. The DQE in EBR-equipped lasers exhibited an unusual dependence on injection current at low temperatures.

Figure 7.3 shows three light vs. current (L vs. I) curves, and three corresponding dL/dI vs. I curves. Figure 7.3(a) illustrates a fictitious ideal case, featuring a sharp threshold and a constant external DQE for $I > I_{th}$. Figure 7.3(b) shows L vs. I and dL/dI vs. I data measured from an EBR-equipped laser at 290K. The L vs. I curve is sub-linear, and this is reflected in the "sagging" of the dL/dI curve for $I > I_{th}$. This progressive decrease in efficiency is a familiar consequence of active region heating in semiconductor lasers.

In contrast, the curves for the *same* EBR-equipped laser at $T \sim 30$ K (see Fig. 7.3(c)) reveal that the DQE *improves* continuously as the current is increased. This behaviour is partly attributable to active region heating in a laser which is operating in a "negative T_o" regime (i.e. in a regime where heating *improves* the laser performance). A second mechanism which is believed to be responsible for the improvement in DQE with increasing current will be described following the presentation of the physical model in § 7.3.

---

[1]If the photo-detector response is nearly flat.
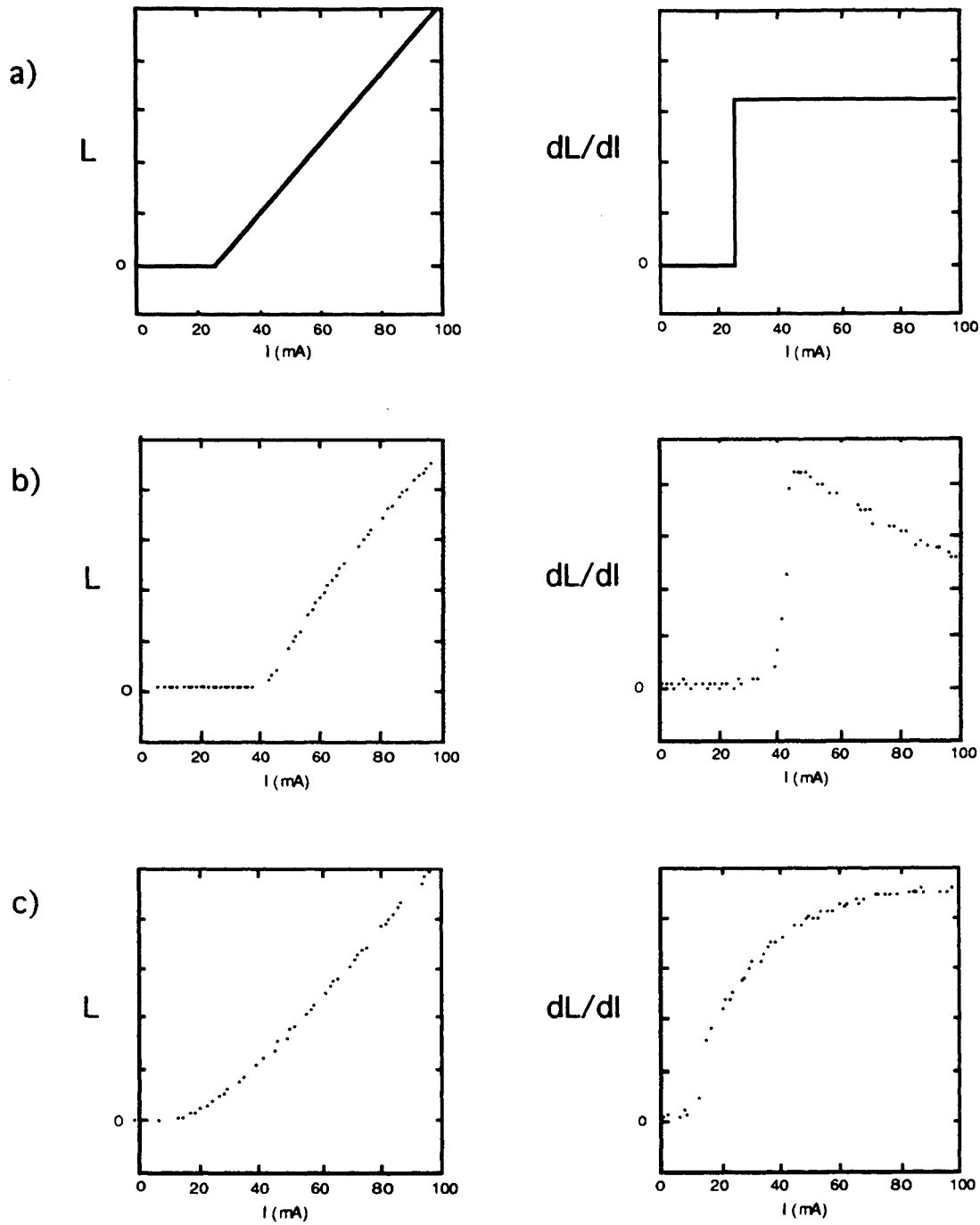
Figure 7.3: *L* vs. *I* and *dL/dI* vs. *I* for an EBR-equipped laser in the normal and anomalous temperature regimes. Curve (a) ideal case; (b) at *T*=290 K, and (c) at *T*=30K. Case (b) shows the "sagging" of laser efficiency with increasing bias due to active region heating; In contrast, case (c) shows an improvement in laser efficiency with increasing bias; this is partly attributable to active region heating in the "negative T_0" regime. Also, see § 7.3.2.

7.2.3 Electroluminescence at $\lambda \sim .9\mu$m Due to Current Leakage Into the InP

The EBR was designed to stabilize laser performance with respect to changes in temperature by inhibiting the Auger-recombination- and thermally-induced leakage of electrons out of the active or separate confinement regions. However, the anomalous behaviour of the threshold current and DQE reported in this work is *not* anticipated to be a basic consequence of increased electron confinement, and no such observations have been reported in the context of the influence of EBRs on laser performance.

Measurements of leakage current at T=285 K and T=305 K (by the integration of the electroluminescence (EL) spectra around $\lambda \sim .9$ μm (§ 6.6)) suggest that leakage is slightly *higher* in the EBR-equipped laser than in the control laser for a given injection current (see Fig. 7.4). Although this result does not bode well for the given EBR design, it remains possible that the EBR is inhibiting hot electron leakage at room temperature, despite the higher threshold current for the EBR-equipped lasers[2]. In any case, the regime of greatest interest lies not at room temperature but in the range of temperatures at or below T_{min}, ($\sim$170 K), where radiative emission from the InP ($\lambda \sim .8-.9\mu$) was not detectable.

It will be recalled that the EBR was designed on the basis of several material parameters that vary with temperature, including the band gaps, the effective masses, and the lattice constants [e.g. see Adachi, 1982]. It can

---

[2]A simple interpretation attributes the larger I_{th} in the EBR-equipped laser to larger leakage currents. However, if the larger Ith in the EBR-equipped laser is due to other mechanisms (e.g. more inter-valence band absorption in the EBR-equipped laser than in the control laser), then the required steady state electron density at threshold is larger, and this implies more hot electron escape *attempts* from the EBR-equipped laser than for the control laser.

be speculated that at $T = T_{min}$ the relevant material parameters collectively establish the most effective reflector for the given design. However this scenario is unlikely, because it ultimately implies that leakage into the InP represents a substantial fraction of the threshold current at T=170K. In fact, the reduction in I_{th} from T=20K to T=170K exceeds the reduction anticipated theoretically from the *complete* elimination of the leakage current for the EBR-equipped laser structure at *room* temperature[3].

In summary, then, available experimental data suggests that electron reflection from the EBR does *not* constitute the principal cause of the anomalous temperature dependence of the threshold current and DQE.
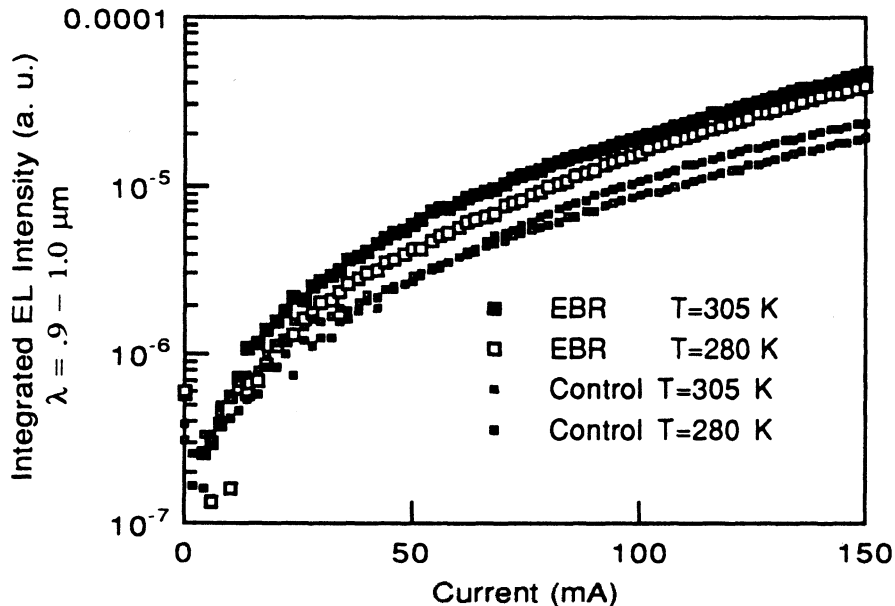
Figure 7.4: Integrated EL intensity from λ=.9 to 1.0μm vs. injection current for a EBR-equipped laser and a control laser at T=285 K and T=305 K. The data suggest that leakage into the InP in the EBR-equipped laser is higher.

---

[3] On the basis of 2-D simulations using the device simulator LUMIN developed by Dr. Z. M. Li at NRC [e.g. see Li *et al.*, 1992].

7.2.4 Long Wavelength (λ = 1.1-1.6μm) Electroluminescence

Although short wavelength (~λ = .8 - .9 μm) EL spectra corresponding to leakage currents in the InP were inconclusive, more substantive insights into the anomalous I_{th} vs T and DQE behaviour for the EBR-equipped lasers are discernible from EL spectra collected from these lasers at longer (λ = 1.1-1.6 μm) wavelengths.

In the control lasers, a single Gaussian lobe developped at the lasing wavelength at all temperatures, while EL spectra for EBR-equipped lasers showed a strongly temperature- and current-dependent three-lobed structure. It is of particular interest to compare the EL spectra of an EBR-equipped laser at low temperature (T~20K) with spectra obtained at T_{min} (170 K) to explore the reasons for the anomalous decrease in the threshold current over that temperature range.

Figures 7.5(a) and 7.5(b) show the dependence upon current of EL spectra obtained from an EBR-equipped laser at T=25K and T=180K (~T_{min}), respectively. The low current (sub-threshold) spectra at T=25K reveal that radiative emission from a lobe centered at ~1.3μm is initially dominant over the long wavelength emission peaked at 1.42μm; however the latter eventually dominates and develops into laser action at I~15 mA (6th trace in Fig. 7.5(a)). In contrast, the spectra shown for the *same* EBR-equipped laser at T=180K (Fig. 7.5(b)) reveals that the long wavelength emission lobe invariably dominates over the shorter wavelength (1.27-1.29μm) lobe. Similarly, it can also be seen that the *shortest* wavelength lobe in Fig. 7.5(a) (which shifts from ~1.25μm to ~1.15μm with injection current) is more prominent at low temperature (T=25K) than at high temperature (T=180K).

a)

b)
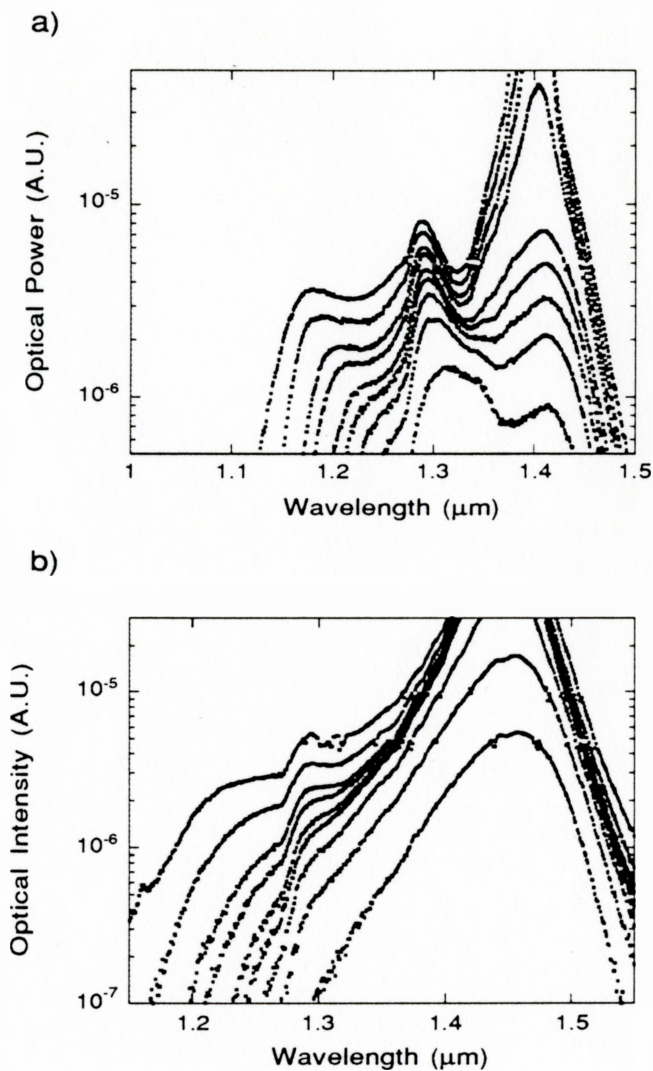
Figure 7.5: EI spectra from an EBR equipped laser at (a) T=25K and (b) T=180K for I=2, 4, 6, 8, 10, 15, 20, 40, and 100mA. At T=25K, lasing threshold occurs at ~15 mA (the 6th trace, counting from the bottom), whereas at T=180K the threshold is ~6 mA (3rd trace from bottom).

It can be concluded that the threshold current in the EBR-equipped laser is larger at T=25K than at T=180K because of enhanced recombination currents at lower temperatures. The relative magnitude of these recombination currents diminish substantially at higher temperatures.

7.3 Basic Physical Model of Anomalous Behaviour

The anomalous I_{th} vs. T and DQE behaviour can be explained by a relatively simple physical model based on a consideration of the temperature dependence of the hole population in the quantum wells of the EBR. The model explains the experimental data without recourse to unsubstantiated arguments concerning reductions in electron leakage currents into the InP due to the EBR.

In this initial discussion it will be assumed for simplicity that the EBR structure may be represented by a *single* quantum well with some appropriate width and depth, as shown in Fig. 7.6(a). Holes are being considered, so the band diagram here delineates the *valence* band edge as a function of position. Hole energy is defined to increase in the downward direction. The well is bound by a potential barrier with height V_{InP} on the right and by a lower barrier of height V_{SC} on the left.

It may be assumed that the holes, which are injected into the EBR quantum wells from the p-type InP, will relax rapidly (<60 fs, [Asada, (Zory Ed., p.117), 1993]) and establish a thermal equilibrium at the lattice temperature. In this situation, the distribution of occupied hole states in the EBR can be described by Fermi-Dirac statistics.

For the laser to attain threshold, there must be a sufficient steady-

85

(a) Simplified Hole Band Diagram

EBR

Separate
Confinement
Region

V_{SC}

V_{InP} p - InP

Valence Band

(b) Low Temperature

EBR

Fermi Level

3 k T

Hole Current

(c) High Temperature

EBR

Fermi Level

3 k T

Hole Current

(d) Total Threshold Current

Separate
Confinement
Region
Current
J_{SC}

Recombination
Current J_R

Total Injected
Current

J

Total

J_{SC}

J_R
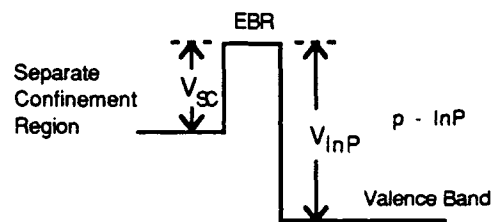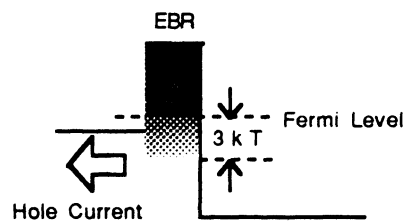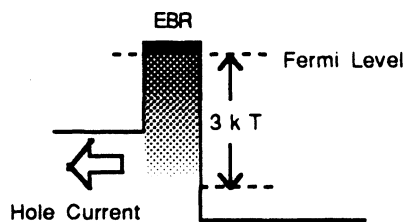
T
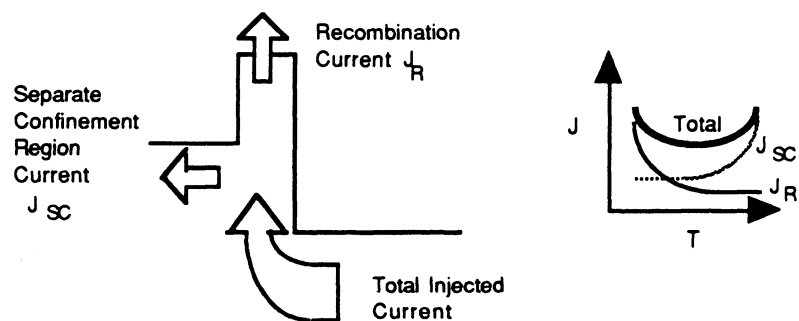
Figure 7.6: Explanation of the anomalous behaviour of the threshold current as a function of temperature.

state current, J_{SC}, of holes which are emitted from the EBR into the separate confinement layer, where they can then diffuse toward the active region. The required hole current density is achieved only when there is a sufficient number of holes in the EBR that have energies *exceeding* the barrier height V_{SC}. When the laser is very cold, the distribution of hole energies will be clustered very near the hole Fermi-level energy; therefore, the Fermi level must be situated very near V_{SC} to supply the required outgoing current (J_{SC}) to the laser active region. This situation is depicted in Fig. 7.6(b). In contrast, at much higher lattice temperatures (say T=170K), the distribution of thermally populated hole states extends well beyond the hole Fermi-level. Therefore, it is possible to establish the required outgoing current (J_{SC}) when the hole Fermi-level is relatively far removed from V_{SC}. This situation is depicted in Fig. 7.6(c).

It can be concluded that the EBR is relatively 'full' of holes when the laser attains threshold at very low temperatures, and is less full when threshold is attained at more elevated temperatures. Correspondingly, there is a significant (up to several mA) current, J_R, which is due to the radiative and non-radiative recombination of electrons and holes in the EBR at low temperatures, and this current will tend to *decrease* as the temperature increases. The temperature dependence of the recombination current is evident in the EL spectra shown in Fig. 7.5.

The *total* current at threshold, J_{th}, is given, of course, by the sum of both the EBR recombination current, J_R, and the current injected into the separate confinement region, J_{SC}. Unlike the recombination current J_R, the current J_{SC} is expected to *increase* with increasing temperature, because the latter will be approximately proportional to the active region threshold current density, which can be roughly expressed as $J_o \exp(T/T_o)$. The sum

of J_{SC} and J_R therefore manifests the anomalous threshold current temperature dependence illustrated in Fig. 7.6(d) at right. This anomalous behaviour features a temperature range over which the total (threshold) current J_{th} *decreases* with increasing temperature (i.e. a "negative T_o" region), followed by the "normal" exponential increase in J_{th} with T.

The several mA recombination current, J_R, in the EBR is larger than one might anticipate from the arguments forwarded in § 4.3.2, where it was noted that no bound electron states exist within the EBR. The substantial recombination can be explained by band bending (induced by the large hole density) in the vicinity of the EBR, which results in the formation of a triangular well for electrons at the edge of the separate confinement region as illustrated in Fig. 7.7. The wavefunction of the electrons in the triangular
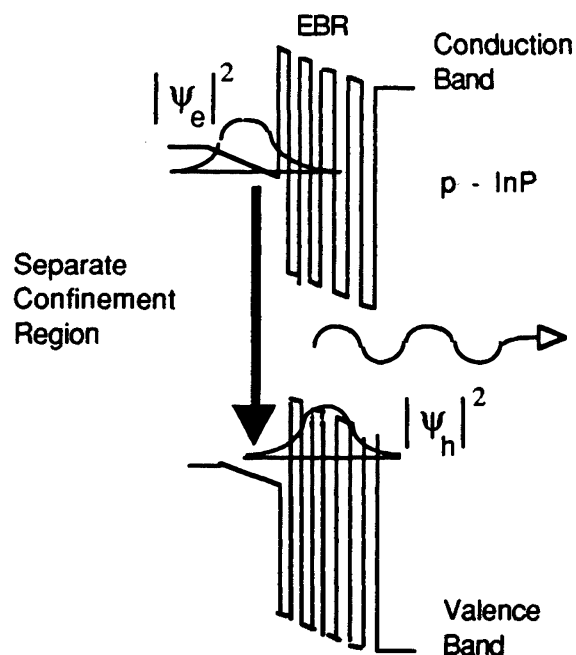
Figure 7.7: Formation of triangular well quantum well for electrons near the interface between the separate confinement region and the EBR. The wavefunction of the electrons and holes are spatially offset.

well extends evanescently into the EBR, resulting in a non-negligible recombination current. A numerical analysis to be presented later (§ 7.4) provides evidence to support the claim in § 4.3.2 that no bound electron states exist within the EBR. The lobe that shifts from 1.25μm-1.15μm in Fig. 7.5(a) may be due to recombination involving either a higher energy EBR valence sub-band, or a higher energy electron state in the triangular well.

In summary, the EBR-equipped lasers demonstrate anomalous I_{th} vs. T behaviour (Fig. 7.1) and superior temperature stability (Fig. 7.2) because the EBR wells provide a hole trap which causes a recombination current whose temperature dependence is complementary to the temperature dependence of the active region recombination current at threshold. The superior temperature stability in the EBR-equipped lasers is achieved at the expense of quantum efficiency and a larger total threshold current.

7.3.1 Supporting Spectral Evidence

The interpretation presented in § 7.3 is consistent with the observed evolution of EL spectra with injected current (Fig. 7.5), which reveal the relative magnitude of the recombination currents in the active region and the EBR. Specifically, in Fig. 7.5(a) (7.5(b)) the lobe peaked at 1.29μm (1.28 μm) is attributed to recombination occuring in the EBR, while the lobe peaked at 1.42μm (1.47μm) corresponds to radiative recombination in quantum well active region.

The (sub-threshold) spectra at $T=25K$ reveal that substantial current is lost to recombination in the EBR. At $T=180K$, the thermally induced escape of holes from the EBR is more efficient than at $T=25K$, and, as a result, the hole population and the recombination current in the EBR are

reduced. Correspondingly, the sub-threshold spectra for T=180K in Fig. 7.5(b) illustrate that recombination in the active region (1.47μm) invariably dominates over recombination in the EBR.

A more explicit elucidation of the model proposed in § 7.3 is provided in Fig. 7.8, which shows the ratio (EL from EBR)/(EL from active region) as a function of temperature, at I =.7 I_{th}. The data clearly illustrate that the relative magnitude of the recombination current in the EBR decreases as the temperature increases. The data points in Fig. 7.8(b) were obtained by separation of the EL spectrum like that which is illustrated graphically in Fig. 7.8(a)[4].

7.3.2 Explanation of the Anomalous DQE

The proposed physical model provides an explanation for the anomalous improvement in the DQE with increasing injection current for the EBR-equipped lasers at low temperature (see Fig. 7.3(c)).

As noted earlier, this behaviour is a partly a consequence of active region heating in a laser which is operating in a "negative T_o" regime. However, the anomalous improvement in efficiency with injection current at T=30K can also be attributed to photon-assisted escape of holes from the EBR.

As the optical intensity in the active region increases, there will be an associated increase in the number of holes in the EBR which are promoted to excited energy levels by inter-valence band absorption. This excitation mechanism has the same effect as an additional thermal excitation of the

---

[4]The emission from the active region of the EBR-equipped laser is assumed to describe a Gaussian, which is consistent with the profiles of the active region emission in the uncomplicated EL spectra obtained from control lasers.

a)
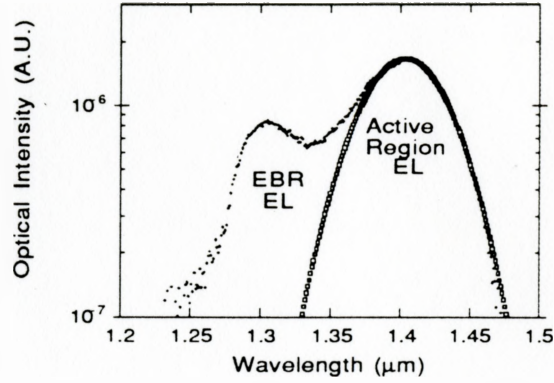
b)
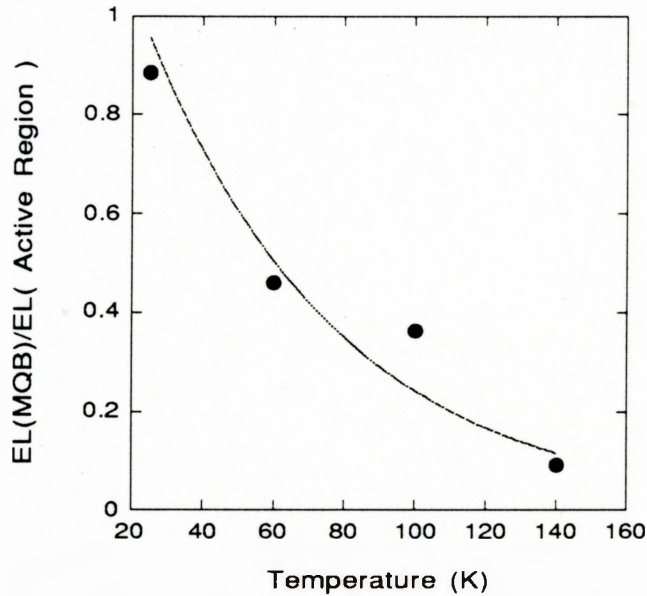
Figure 7.8: Relative fraction of EBR recombination current as a function of laser temperature at 70% threshold current. (a) Graphical example of separation of EBR radiation from active region radiation. The EL from the active region appears to be well described by a Gaussian (This is confirmed by the uncomplicated spectra obtained for the control lasers). (b) Ratio of EL from the EBR divided by the EL from the active region at 70% threshold current.

EBR hole population. This extra hole population "heating" is expected to provide an improvement in laser efficiency by a process which is identical to the one outlined in the basic physical model (§ 7.3) to explain the reduction in the threshold current with increasing temperature.

7.4 Mathematical model

7.4.1 Overview

The physical interpretation described in § 7.3 has also been assessed by a quantitative analysis. This section describes the formulation of a 1-D mathematical model which reproduces the negative-T_o behaviour by using realistic material parameters and well-known closed-form expressions for carrier kinetics. It will be shown that the model provides an excellent fit to the experimental data.

The basis for the 1-D model is given by the band diagram shown in Fig. 7.9, which represents the EBR-equipped laser biased at threshold. The values of various constants (band gaps, effective masses, etc.) are assumed to be equal to their room temperature values (See Appendix A, Adachi [1982], and Madelung [1991]). The lowest lying valence sub-bands in the active region and the EBR were calculated using Eq. (3.23).

Figure 7.9 indicates recombination currents by white arrows, i.e.:

i) J_a, the current density injected into the active region at threshold;

ii) J_s, the current which is due to the recombination of holes
with electrons in the separate confinement region[5]; and,

iii) J_R, the current due to electron-hole recombination in the EBR.

---

[5]The sum of J_a and J_s corresponds to the current J_{SC} which was used in the simple physical model.

Figure 7.9: Band diagram of the EBR-equipped laser biased at threshold, showing the effective masses, the band offsets, and the lowest lying conduction (E_{cw},E_c) and valence (E_{vw}, E_{v0}) sub-bands in the active region and the EBR, respectively. The hydrostatic shift of the conduction and valence band in the quantum well are labeled in italics.

The two black arrows indicate where the transport of charge is primarily achieved by tunneling processes; specifically:

i) T_h represents hole tunneling from the outermost well of the EBR into the separate confinement region.

ii) T_e is the electron tunneling current which penetrates into the EBR from the separate confinement region.

The largest contribution to T_e is assumed to result from the penetration into the EBR of the wavefunction of electrons within the triangular well (not shown; see Fig 7.7) formed at the interface between the EBR and the separate confinement region.

With the exception of the tunneling process designated in Fig. 7.9 by T_h, hole transport is assumed to proceed by diffusion [Lee et al., 1993].

7.4.2 Current Balance

In reference to Fig. 7.9, the temperature dependent threshold current density for a EBR-equipped laser is given by

$$J_{th,EBR} = J_a + J_s + J_R \tag{7.1}$$

while the threshold current density for a control laser is simply

$$J_{th,control} = J_a + J_s. \tag{7.2}$$

The control and EBR-equipped laser were designed to be identical in every respect (e.g., active region volume, cavity length, doping profile, mirror reflectivity) except for the EBR. Therefore, it can be postulated that

the current J_a which must be injected into the active region at threshold is approximately equal for both lasers[6],

$$J_{a,EBR} \approx J_{a,control}. \tag{7.3}$$

It follows that the recombination currents during the diffusion of holes across the identically Si-doped separate confinement region should also be approximately equal;

$$J_{s,EBR} \approx J_{s,control}. \tag{7.4}$$

Using Eqs. (7.3) and (7.4), Eq. (7.1) can be rewritten as

$$J_{th,EBR} \approx J_{th,control} + J_R \tag{7.5}$$

where $J_{th,control}$ is given by the experimentally recorded threshold current for the control laser as a function of temperature (see Appendix A.1).

The assumptions made with Eqs. (7.3)-(7.5) result in a considerable simplification of the quantitative analysis, because they eliminate the requirement of calculating the gain in the strained quantum well active region as a function of carrier density and temperature. With these assumptions, the task of modeling I_{th} vs. T for the EBR-equipped laser has been reduced to the determination of the recombination current J_R as a function of temperature

7.4.3 Recombination Current in the EBR

Assuming that charge neutrality is established overall in the region which includes both the EBR and the triangular well for electrons, then the

---

[6]Eq. (7.3) more properly represents the lower limit for Ja,EBR since the EBR-equipped laser is expected to experience larger optical losses due to intervalence band absorption of holes in the EBR wells.

total excess electron and hole populations are equal in this region. Assuming further that the carrier *densities* n and p localized (respectively) in the triangular well and the outermost EBR well are approximately equal, then the recombination current J_R can be expressed by the approximate relation [Agrawal *et al.*, p. 122, 1986]

$$J_R = d \left(f_1 B p^2 + f_2 C p^3 \right). \tag{7.6}$$

In Eq. (7.6), d is the width of the outermost well, and the first and second terms in the parentheses account for radiative and Auger recombination processes[7], respectively. The pre-factors f_i in Eq. (7.6) are phenomenological fractions which account for the expected *reductions* in the radiative and Auger recombinations due to the spatial displacement of the electron population from the hole population. The f_i therefore represent wavefunction overlap factors; for simplicity they will be considered equal

$$f_1 = f_2 = f. \tag{7.7}$$

The overlap factor f will be employed as the fitting parameter in this model.

The hole density p in the outermost EBR well (which dictates the recombination current through Eq. (7.6)) consists of the sum of the densities below (p_w) and above (p_{wo}) the barrier energy V_{SC}, i.e.

$$p = \int_{E_{h0}}^{V_{SC}} \rho_{2D}(E)\, F(E)\, dE + \int_{V_{SC}}^{\infty} \rho_{3D}(E)\, F(E)\, dE$$

$$= p_w + p_{wo} \tag{7.8}$$

---

[7]A term proportional to p accounting for recombination mediated by traps and bulk or interface defects has been omitted for simplicity. This term is relevant only at low carrier densities [e.g. see Englemann *et al.*, (Zory, Ed., p.161), 1993].

where $F(E)$ is the Fermi-Dirac function, ρ_{2D} is the density of hole states corresponding to propagation in the plane of the well, and ρ_{3D} is the bulk density of hole states. The densities p_w and p_{wo} are expressed as

$$p_w = \frac{m_{h\parallel}^*}{\pi \hbar^2} \left(\Delta + k T \ln \left(\frac{1 + e^{(E_{fh}-\Delta)/kT}}{1 + e^{\Delta/kT}} \right) \right)$$ (7.9)

and

$$p_{wo} = 4\sqrt{2} \left(\frac{kT\, m_h^*\, \pi}{h^2} \right)^{\frac{3}{2}} e^{(H-\Delta)/kT} \left(1 - \frac{2}{\sqrt{\pi}}\, \Gamma_{3/2}\left(\frac{H}{kT} \right) \right)$$

$$\Gamma_n(z) = \int_0^z t^{n-1} e^{-t}\, dt$$ (7.10)

where $m_{h\parallel}^*$ is the effective heavy hole mass in the plane of the wells, $\Delta = V_{SC}\text{-}E_{fh}$, and $H = V_{SC}\text{-}E_{h0}$, where E_{fh} is the hole quasi-Fermi-level[8], and E_{fh} is the energy of the lowest-lying valence sub-band in the outer-most EBR well.[9]

The density of holes in the outermost EBR quantum well with energies exceeding V_{sc} (i.e. p_{wo}) dictates the current density which emanates from the EBR toward the active region. In this model, it is assumed that these holes enter the separate confinement region by efficiently tunneling through the thin (40 Å) InP barrier[10] separating the EBR and the separate confinement region. At threshold, the hole current must be equal to $J_{th,control}$. Assuming purely diffusive hole transport, and that the active region acts as a perfect hole sink, p_{wo} can be expressed as

---

[8]Equations (7.8) and (7.9) incorporate the following assumptions: 1) the heavy hole band is parabolic, 2) only the lowest lying hole sub-band is appreciably populated, 3) at $E > V_{SC}$ the hole population is distributed according to the 3-D density of states, and 4) Boltzmann statistics are applicable for $E > V_{SC}$.

[9]There is a four-fold degeneracy of the hole sub-bands due to coupling between the four quantum wells in the EBR. However, calculations performed using the TMME (Chapter 3) reveal that this coupling is weak. It is therefore appropriate to consider the wells and their eigenstates uncoupled.

[10]The emission of holes from the outermost EBR-quantum well into the separate confinement region can therefore be regarded as a thermally-assisted tunneling process [e.g. see Takasaki, 1992].

$$p_{wo} = \frac{L_p \ tanh(W/L_p) \ J_{th,control}}{q \ D_p}$$ (7.11)

where: q is the electronic charge; W is the width of the separate confinement layer; and D_p and L_p are the hole diffusivity and diffusion length in the separate confinement region. With Eq. (7.11) it is assumed that the hole density just inside the separate confinement region is equal to p_{wo}.

For any given temperature, the hole Fermi level E_{fh} must be chosen so that Eqs. (7.10) and (7.11) are both satisfied; E_{fh} then specifies p through Eqs. (7.9) and (7.8), which yields the magnitude of the recombination current through Eq. (7.6).

7.4.4 Comparison of Experiment and Theory

Figure 7.10 illustrates the excellent agreement obtained between calculated and experimentally measured I_{th} vs. T data between T=70K and T=230K for an EBR-equipped laser. The overlap factor f for the theoretical curve is .572, suggesting that recombination is reduced in comparison to the case of spatially coincident carrier populations (for which the overlap factor would be ~1). Although this supports to the claim of § 4.3.2 that the EBR does *not* support bound electron states, the support must be deemed marginal in light of the simplicity of the model and the uncertainty among several key physical parameters (e.g., effective masses, band offsets, and the Auger and radiative recombination coefficients). However, upon reviewing the assumptions made during the derivation of the model, it can be deduced that the majority tend to *underestimate* the hole population in the EBR[11].

---

[11]e.g. parabolic hole bands, a 3-D density of hole states for E>V$_{SC}$, appreciable hole population in only the lowest energy EBR valence sub-band, efficient hole escape through the 40 Å InP barrier, the active region is perfect hole sink, *etc.*

For assumptions yielding *larger* hole populations in the EBR, a *smaller* value of f would be obtained[12].

For instance, by maintaining all the existing model assumptions and increasing the effective hole mass from .381 m_0[13] to .85 m_0 (resulting in a larger density of hole states and hence *larger* number of holes in the EBR wells), the value obtained for f is reduced by more than an order of magnitude, to .05611. This provides more credible evidence for the claim in § 4.3.2 that the EBR supports no confined electron states.
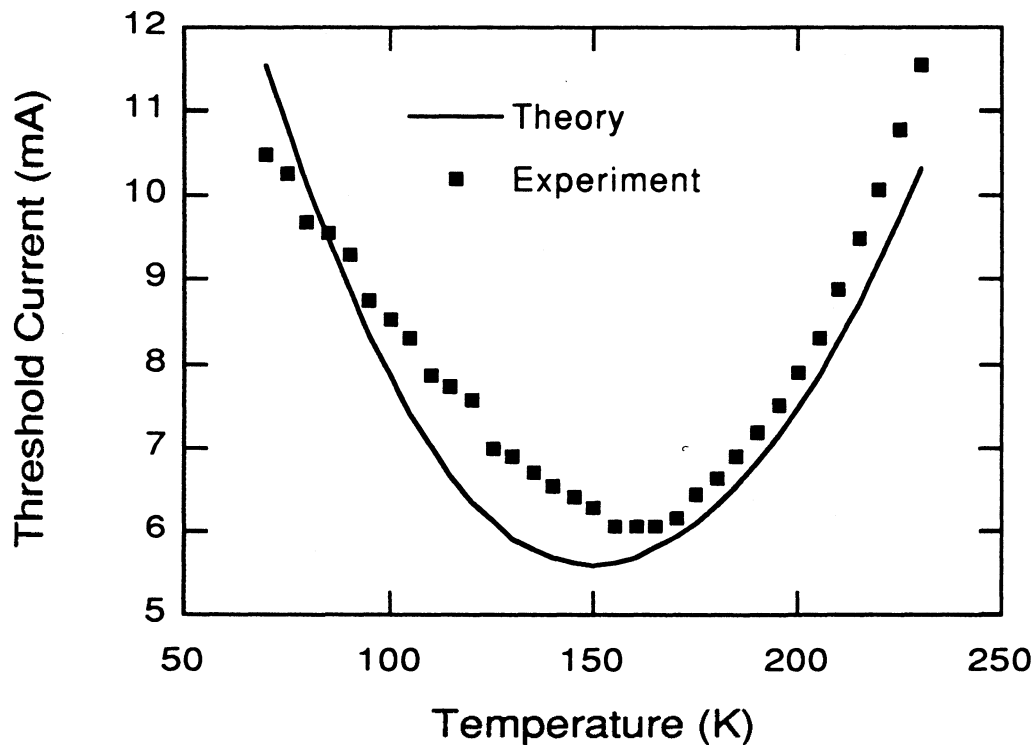
Figure 7.10 : Theoretical and experimental I_{th} vs. T data for an EBR-equipped laser. The fit between the theoretical and experimental data was optimized by setting the overlap factor f equal to 0.572.

---

[12]because the EBR recombination current is proportional to the product of the hole population and the overlap factor.

[13]the theoretical value obtained from the Luttinger parameters. See appendix A.5.

7.4.5 Comparison of Experiment to Theory using Temperature-Dependent Recombination Coefficients

The fit between the experimental and theoretical I_{th} vs. T data is improved when the radiative and Auger recombination coefficients are given a temperature dependence. The radiative recombination coefficient is given the 1/T functional dependence derived by Matsusue *et al.* [1987] for non-degenerate excess carrier populations in quantum wells, whereas the Auger recombination coefficient is ascribed an exponential temperature dependence which has been extracted by the author from theoretical data presented in Agrawal *et al.* [1986] for an excess carrier density of 10^{18} in 1.3μm InGaAsP (see Appendix A.3). The improved fit is shown in Fig. 7.10.
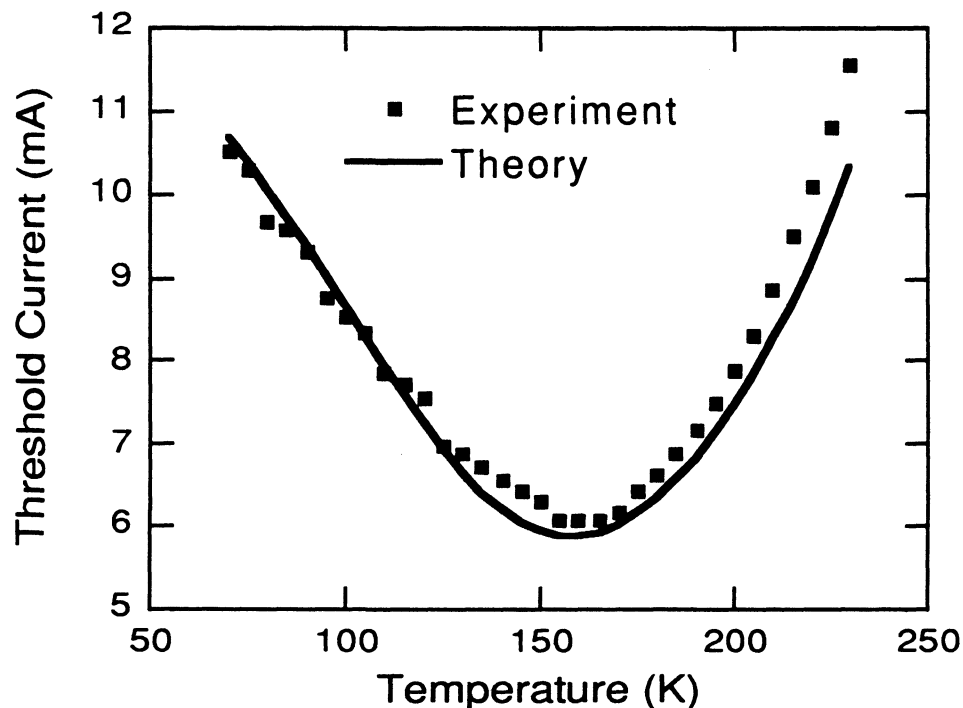
Figure 7.11: Theoretical and experimental I_{th} vs. T data for an EBR-equipped laser, using temperature dependent radiative and Auger recombination coefficients. The fit between the theoretical and experimental data was optimized by setting the overlap factor f equal to .568 and m_{hh}=.85 m_0.

7.4.6 Improved Threshold Current Temperature Stability at 300 K.

Finally, it is of interest to consider laser designs yielding an improved temperature stability of I_{th} around T=300K by the mechanism which was discovered to be responsible for the improved temperature stability of I_{th} between T=130-220K in EBR-equipped lasers. The goal is to introduce a hole trap which causes a temperature-dependent recombination current which is complementary to the temperature-dependent active region (threshold) recombination current around T=300K.

Figure 7.11 shows a laser design including a lattice-matched 34 Å wide InGaAs quantum well located between the InP cladding and (1.1 eV) InGaAsP separate confinement region. This quantum well is transparent to the active region radiation, and provides the required hole trap.

The threshold current temperature dependence of the proposed laser has been calculated using the mathematical model presented in § 7.4, using f=1 (since the quantum well supports a confined electron state), and $m_{hh}^* =$ .45 m_0 for $In_{.47}Ga_{.53}As$. The current injected into the separate confinement region at threshold is assumed to be equal to the experimentally measured threshold current for the control laser (see Appendix A.1). The characteristic temperature, T_o, for the proposed laser and a control laser (using Eq. A.1.1) are compared in Fig. 7.13. The proposed laser design exhibits a superior temperature stability for the threshold current; however, it will be recalled that this feature is obtained at the expense of *larger* threshold currents and inferior quantum efficiency.
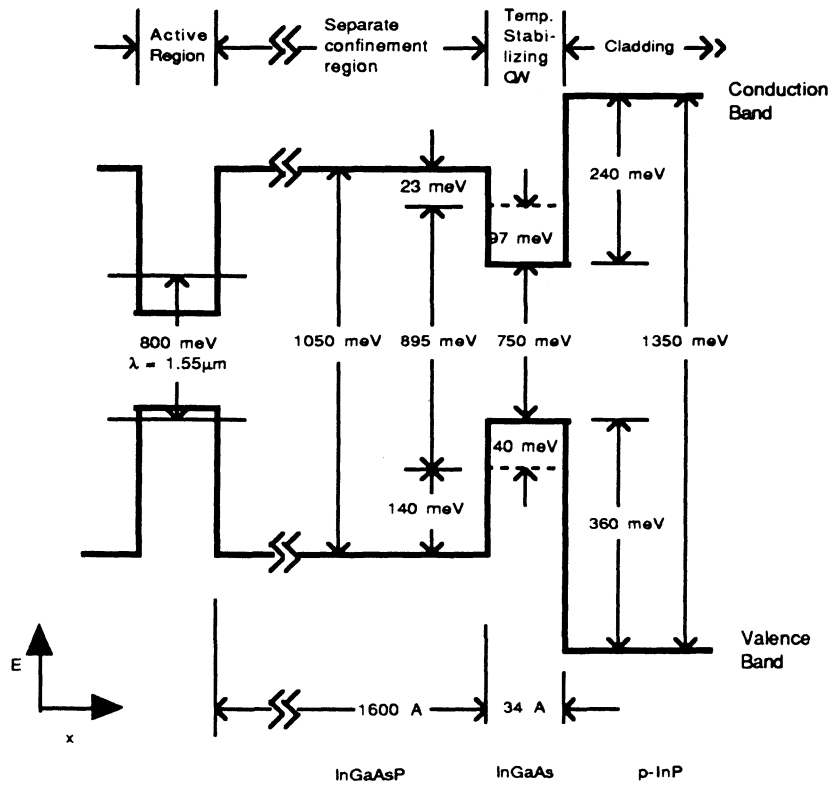
Figure 7.12: Design for laser with superior temperature stability at T=300K.
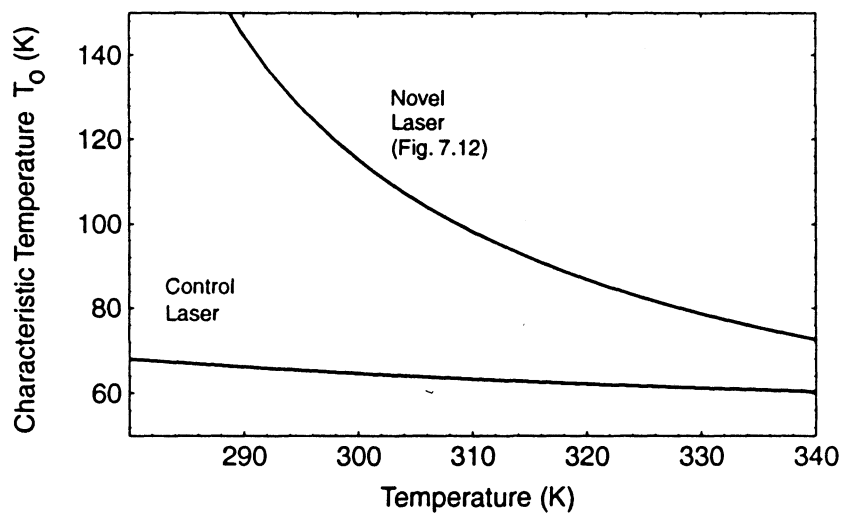
Figure 7.13: Comparison of T_O vs. T obtained from I_{th} vs. T data calculated for the laser design proposed in Fig. 7.12, and I_{th} vs. T data for a control laser. The control laser threshold current was calculated using Eq. (A.1.1).

Chapter 8: Summary and Conclusions

8.1 Waves in Layered Media

Transfer matrices were presented for the analysis of TE polarized light propagating within media described by piece-wise linear, parabolic, and exponential variations of the complex dielectric constant. More than an order of magnitude improvement in efficiency was realized for the computation of the complex mode index of graded index planar optical waveguides by using these exact matrices. This suggests that similar improvements can be expected in the application of equivalent transfer matrices to the calculation of the energy levels of electrons in arbitrarily graded quantum wells, e.g., resulting from ion-bombardment-induced disordering or growth transients.

8.2 EBR Design

An EBR was implemented in an InGaAsP/InP laser for the first time. To improve the quantum mechanical reflection bandwidth and relax fabrication tolerances, the EBR layer thicknesses were varied systematically (i.e. "chirped"), with its quantum wells decreasing in thickness with increasing depth into the p-type InP cladding. By the placement of the chirped EBR adjacent to the separate confinement region, a return path was provided for electrons that have scattered inelastically within the EBR. Moreover, the EBR structure was designed to support no bound electron states, so that the recombination of electrons with holes in

the EBR would be minimal. To the author's knowledge, the EBR-equipped laser fabricated for this work represents the first attempt to exploit electron state exclusion from a quantum well structure.

Under the assumption that the majority of the hydrostatic shift induced by strain affects the conduction band (e.g. see § A.5.2), then it follows that the use of tensile (rather than compressive) strain would provide deeper conduction band wells (yielding larger EBR reflectivity bandwidths) with reduced penalties due to EBR lowering caused by band-bending.

8.3 Performance of EBR-Equipped Lasers

The EBR-equipped lasers exhibited an anomalous DQE current dependence at low temperatures, and an anomalous threshold current temperature dependence, featuring a "negative-T_o" regime (in which the threshold current *decreased* with increasing temperature), attaining a minimum in threshold between T=150 K and T=200 K. These lasers had a threshold current temperature stability superior to that of control lasers within a ~70K window around the minimum threshold temperature.

The anomalous temperature dependence of the threshold current has been attributed to the temperature dependence of the hole escape efficiency from the EBR quantum wells. This interpretation is substantiated by electroluminescence spectra, differential quantum efficiency data, and a mathematical model. The mathematical model provided evidence supporting the assertion that no bound electron states exist within the EBR conduction band wells.

Enhanced hot electron containment within the separate confinement or active region due to the EBR is not confirmed by available data. Spatially resolved electroluminescence investigations are recommended. The magnitude of the extraneous recombination currents in the present EBR-equipped laser design are believed to exceed any potential reductions in leakage currents at any temperature within the operational temperature range for these lasers.

The mathematical model presented in § 7.4 suggests that the mechanism which causes the anomalous temperature dependence of the threshold current can be exploited to provide superior temperature stability in semiconductor lasers at $T=300$ K or above. However, there will be an associated penalty in the threshold current and in the external differential quantum efficiency.

Appendix A: Supplementary Equations

A.1 Experimental Threshold Current Temperature Dependence

It was found that the experimentally measured threshold current for the EBR-equipped and control laser between T = 50K and T = 250K are accurately described by the function,

$$I_{th} = \alpha_1 e^{\beta_1 T} + \alpha_2 e^{\beta_2 T} \tag{A.1.1}$$

where α_1 = +.106549, β_1 = +.017937, α_2 = +2.59842, and β_2 = +.00153085 for the control laser, and α_1 = +21.518, β_1 = -.01023, α_2 = +0.0764, and β_2 = +.020924 for the EBR-equipped laser.

A.2 Hole Transport across the Separate Confinement Region

Minority hole transport is described by the diffusion length, L_p, and coefficient, D_p, given by

$$L_p = \sqrt{D_p \tau}, \tag{A.2.1}$$

$$D_p = \frac{kT}{eV} \mu_p, \tag{A.2.2}$$

where τ is the hole (minority) carrier lifetime in the n-doped separate confinement region, and μ_p is the temperature-dependent hole mobility, which is assumed to obey[1]

$$\mu_p = \left(\alpha T^3 + \beta T^2 + \gamma T^1 + \delta\right)/1000, \tag{A.2.3}$$

where $\alpha = -7063 / 518400$, $\beta = 2501 / 1080$, $\gamma = 5 / 36$, and $\delta = 229 / 10368000$.

The minority hole lifetime, τ, in Eq. (A.2.1) is given by

$$\frac{1}{\tau} = \frac{1}{\tau_{Rad}} + \frac{1}{\tau_{Auger}} + \frac{1}{\tau_{defects}}, \tag{A.2.4}$$

where the defect-mediated, radiative, and Auger recombination lifetimes can be expressed as

$$\frac{1}{\tau_{defects}} = A, \tag{A.2.5}$$

$$\frac{1}{\tau_{Rad}} = B\,\bar{p}, \tag{A.2.6}$$

$$\frac{1}{\tau_{Auger}} = C\,\bar{p}^2, \tag{A.2.7}$$

where $\bar{p}$ is a representative mean of the hole density in the separate confinement region (Recall that the hole density will vary across the separate confinement region; it is assumed to decrease from its maximum value adjacent to the EBR to zero at the hole sink provided by the quantum well active region). In the model, it is assumed that

---

[1]Fit obtained by the author to data reported in [Hayes et al., 1982].

$$p = 2/3 \ p_{wo}. \hspace{4cm} \text{(A.2.8)}$$

A.3 Temperature-Dependence of Recombination Coefficients A, B, and C.

The coefficient A, which dictates the rate of defect and impurity mediated recombinations, is assumed to be independent of temperature.

Matsusue *et al.* [1987] found that the radiative recombination coefficient for non-degenerate carrier populations in a quantum well is accurately described by

$$B(T) = B_{@300K}/T \hspace{4cm} \text{(A.3.1)}$$

between T~80K and 300K. Although Eq. (A.3.2) is not strictly valid for degenerate carrier densities, it is used for simplicity.

The temperate dependence of the Auger recombination lifetime presented in Agrawal *et al.* [p.115, 1986] for an excess carrier density $n = p = 10^{18} \ cm^{-3}$ in ~.9 eV band gap ($\lambda = 1.3 \ \mu m$) InGaAsP is approximately described by[1]

$$C(T) = C_{@300K} \ 30^{((T/200 - 3/2))}. \hspace{3cm} \text{(A.3.2)}$$

This form is used to account for the temperature dependence of Auger recombination in the outermost EBR quantum well, since the band gap (~1.0 eV) and the carrier densities are comparable to those for which the data in [*ibid.*] was derived.

The values used for the coefficients are: $A=10^{10}$ s, $B=1.5 \ 10^{16}$ s/m^6,

---

[1]Fit by author.

and C = 10^{-41} s/m^9 when C is fixed, and C$_{@300K}$ = 10^{-40} s/m^9 when Eq. (A.3.2) is used. These values are quoted from measurements reported for 1.3µm wavelength emission LEDs and lasers [see Agrawal, p.121-122, 1986].

A.4 Relations used for lattice-matched $In_{1-x}Ga_xAs_yP_{1-y}$

Mole fractions: $x = .1894\, y/(.4184 - 0.013\, y)$ (A.4.1)

Band gap: $Eg = 1.35 - .738\, y + .138\, y^2$ (eV)   (A.4.2)

Electron effective mass: $m^* = (.077 - 0.050\, y + 0.14\, y^2)\, m_0$ (A.4.3)

Lattice constant: $a_o = 5.8688\, \text{Å}$ (1 monolayer = $a_o /2$)   (A.4.4)

A.5 Relations used for strained $In_{1-x}Ga_xAs_yP_{1-y}$

A.5.1 The Hole Effective Mass

The anisotropic hole effective masses at the valence band edge in lattice matched or strained materials can be described by simple expressions involving the Luttinger parameters, γ_1, γ_2, and γ_3 [O'Reilly, 1990], according to

$$m_{hh}^* \langle 001 \rangle = 1/(\gamma_1 - 2\, \gamma_2)$$
$$m_{hh}^* \langle 111 \rangle = 1/(\gamma_1 - 2\, \gamma_3)$$
$$m_{lh}^* \langle 001 \rangle = 1/(\gamma_1 + 2\, \gamma_2)$$
$$m_{lh}^* \langle 111 \rangle = 1/(\gamma_1 + 2\, \gamma_3)$$

    (A.5.1.1)

where the angled brackets designate the crystal directions.

For compressively strained layers, the degeneracy of the light and heavy hole bands is removed, with the heavy hole band moving to lower energy. The in-plane effective hole mass is then given by

$$m^*_{hhS} = 1/(\gamma_1 + \gamma_2),$$

(A.5.1.2)

whereas the heavy-hole mass in the direction normal to the layers is unaltered. The Luttinger parameters for an arbitrary InGaAsP alloy can be extrapolated using Eq. A.5.2.1 from the values listed in Table A.1 for the constituent binaries.

Table A1: Luttinger Parameters

	InAs	InP	GaAs	GaP
γ_1	19.67	5.04	6.80	4.20
γ_2	8.37	1.56	2.40	0.98
γ_3	9.29	1.73	1.00	1.66

A.5.2 Band Gap for Strained $In_{1-x}Ga_xAs_yP_{1-y}$

The band gap of a material for an arbitrary InGaAsP alloy composition may be calculated using either:

i) an extrapolation from the constituent binaries

$$Eg(x,y) = (1-x)y\ InAs + (1-x)(1-y)\ InP + x\ y\ GaAs + x\ (1-y)\ GaP$$

(A.5.2.1)

where $InAs = 0.36\ eV$, $InP = 1.35\ eV$, $GaAs = 1.42\ eV$, $GaP = 2.74\ eV$, or

ii) an extrapolation from the ternaries

$$Eg(x,y) = \frac{1}{x\,(1\text{-}x) + y(1\text{-}y)} \Big(\, x\ (1\text{-}x)\ (\,(1\text{-}y)\ (InGaP + y\,InGaAs\,) +$$

$$+ y\,(1\text{-}y)(1\text{-}x)((1\text{-}x)\ InAsP + x\,GaAsP)\,\Big) \tag{A.5.2.2}$$

where

$$InGaP\ (x) = 1.35 + .643\,x + .786\,x^2 \tag{A.5.2.3}$$

$$InGaAs(x) = 0.36 + .505\,x + .555\,x^2 \tag{A.5.2.4}$$

$$InAsP\ (y) = 1.35 - 1.083\,y + .091\,y^2 \tag{A.5.2.5}$$

$$GaAsP(y) = 2.74 - 1.473\,y + .146\,y^2 \tag{A.5.2.6}$$

Although both methods recover the appropriate band gap for any of the constituent binaries, neither produce a very good fit to the experimentally measured variation of the band gap energy reported in the literature for lattice matched $In_{1-x}Ga_xAs_yP_{1-y}$ from y=.7 to y=1. However, it was found that the arithmetic mean of i) and ii) yields a much improved fit. The mean was employed to determine the band gap of .64 eV for the *unstrained* $In_{.846}Ga_{.154}As_{.803}P_{.197}$ alloy quantum wells used in the active region and the EBR.

The quantum wells are strained by ~1.52% within the laser structure, which is lattice matched to InP. The hydrostatic component of the compressive strain induces an increase in the band gap, where 2/3 of this increase is typically assigned to the conduction band [e.g., Chuang, 1991]. It was determined that the hydrostatic band gap shift must be ~70 meV (47 meV conduction/23 meV valence) to recover the experimentally observed (λ~1.55μm) optical emission at low injection currents.

References

Abeles, F., "Recherches sur la propagation des ondes électromagnétiques sinusoïdales dans les milieux stratifiés. Application aux couches minces", Ann. de Physique **12**, pp. 596-640 (1950).

Abramowitz, M., and Stegun, I. A., <u>Handbook of Mathematical Functions</u>, (Ch. 9, 10, and 13.) (Dover, New York, 1964).

Adams, D. M., Makino, T., and Simmons, J. G.,"Exact analytical and approximate analyses of Bragg reflectors with non-rectangular index profiles", Opt. Let. **17**, (24), pp. 1734-1736 (1992)

Adams, M. J., <u>An Introduction to Optical Waveguides</u> (Wiley, Chichester, UK, 1981).

Adachi, S., "Material Parameters in InGaAsP and related binaries", J. Appl. Phys., **53** (12), pp 8775-8792 (1982).

Agrawal, G. P., and Dutta, N. K., <u>Long Wavelength Semiconductor Lasers</u> (Van Nostrand, New York, 1986).

Anderson, K., Bell-Northern Research, Ottawa, *private communication*, 1993.

Anemoglannis, E., and Glytsis, E. N., "Multi-layer waveguides: efficient numerical analysis of general structures", IEEE J. Lightwave Tech. **10** (10), pp. 1344-1351 (1992).

Anthony, P. J., Pawlik, J. R., Swamiinathan, V., and Tsang, W. T.,"Reduced threshold current temperature dependence in double heterostructure lasers due to separate p-n and heterojunctions", IEEE J. Quantum Elec., **19** (6), pp 1030-1034 (1983).

Arimoto, S., Yasuda, M., Shima, A., Kadoiwa, K., Kamizato, T., Watnabe, H., Omura, E., Aiga, M., Ikeda, K, and Mitsui, S., "150 mW fundamental transverse mode operation of 670 nm window laser diode", IEEE J. Quantum Elec., **29** (6), pp 1874-1879 (1989).

Asada, M, and Suematsue, Y., "The effects of loss and nonradiative recombination on the temperature dependence of threshold current in 1.5-1.6 μm GaInAsP/InP lasers", IEEE J. Quan. Elec., **19** (6), pp 917-921 (1983).

Asada, M., Kameyama, A. and Suematsu, Y., "Gain and intervalence band absorption in quantum well lasers", IEEE J. Quantum Elec., **29** (6), pp. 1469-1497 (1984).

Bastard, G., "Superlattice band structure in the envelope-function approximation", Phys. Rev. B, B24 (10), pp. 5693-5697 (1981).

Bastard, G. "Theoretical investigations of superlattice band structure in the envelope function approximation", Phys. Rev., B **25** (12), pp. 7584-7597 (1982).

Beckett, D., and Li, G. P., Bell-Northern Research, Ottawa, *unpublished results*, 1992.

Bellcore Technical Note #TR-NWT-000909, Section 15, "Miscellaneous common requirements", (Dec., 1991)

Brekhovskikh, L. M., Waves in Layered Media: Second Edition,(Academic Press, New York, 1980).

Boer, K. W.,Survey of Semiconductor Physics, (Van Nostrand, New York, 1990).

Capasso, F., Sirtori, C, Faist, J., Sivco, D. L., Chu, S. G., Cho, A.,"Observation of an electronic bound state above a potential well", Nature, **358** (6387), pp. 565-567 (1992).

Casey, H. C., and Panish, M. B. Physics of Semiconductor Laser Devices (John Wiley, Chichester, 1980).

Cassidy, D., and Elenkrig, B., Dept. Eng. Phys., McMaster University, Hamilton, *unpublished results,* 1993.

Chen, T. R., Margalit, S., Koren, K., Yu, L., Chiu, Hasson, A., and Yariv, A., "Carrier leakage and the temperature dependence of InGaAsP lasers", Appl. Phys. Lett., **43**, pp. 217-218 (1983).

Chik, K. D., and Richardson, B. A.,"On the origin of the carrier leakage in GaInAsP/InP double-heterojunction lasers", J. Appl. Phys., **67** (5), pp 2660-2662 (1990).

Chik, K. D., "A theoretical analysis of Auger recombination induced energetic carrier leakage in GaInAsP/InP double heterojunction lasers and light emitting diodes", J. Appl. Phys., **63** (9), pp 4688-4698 (1988).

Chilwell, J., and Hodgkinson, I., "Thin-films field-transfer matrix theory of planar multilayer waveguides and reflection from prism-loaded waveguides", J. Opt. Soc. Am. A, **1** (7), pp. 742-746 (1984).

Chiu, L. C., Yu, K. L., Margalit, S., Chen, T. R., Koren, U., Hasson, A., and Yariv, A., "Field and Hot Carrier Enhanced Leakage in InGaAsP/InP Heterojunctions", IEEE J. Quan. Elec., QE-19 (9), pp. 1335-1338 (1983).

Chuang, S. L., "Efficient band-structure calculations of strained quantum wells", Phys. Rev. B, B43 (12), pp. 9649-9661 (1991).

Chong, T. C., and Fonstad, C. G., "Theoretical gain of strained-layer semiconductor lasers in the large strain regime", IEEE J. Quantum Electron, 25 (2), pp. 171-178 (1989).

Del Alamo, J., and Eugster, C. C., "Quantum field-effect directional coupler", Appl. Phys. Lett., 56 (1), pp. 78-79 (1990).

Dufour, C., and Herpin, A., "Propagation des ondes électromagnétiques dans un milieu stratifié périodique transparent", Rev. D'Optique Theor. et Instr., 32 (6), pp. 6-331 (1950).

Evans, J. D., Dept. Eng. Phys., McMaster University, Hamilton, *unpublished results,* 1993.

Evans, J. D., Makino, T., Puetz, N., Simmons, J. G., and Thompson, D. A.,"Strain- induced performance improvements in long-wavelength multiple-quantum-well ridge- waveguide lasers with all quaternary active regions", IEEE Phot. Tech. Lett., 4 (4), pp. 299-301 (1992).

Forrest, S. R., Schmidt, P. H., Wilson, R. D., Kaplan, M. L.,"Relationships between the condcution-band discontinuities and band-gap differences of InGaAsP/InP heterojunctions", Appl. Phys. Lett. 45 (11), pp. 1199-1201 (1984).

Furruya, A., and Hideeenaao T.,"Superposed multiquantum barriers for InGaAlP heterojunctions", IEEE J. Quantum Elec., 28 (10), pp 1977-1982 (1992).

Gaylord, T. K., Glytsis, E. N., and Brennan, K. F.,"Electron-wave quarter-wavelength quantum well impedance transformers between differing energy gap semiconductors", J. App. Phys., 67 (5), pp. 2623-2630. (1990).
Gaylord, T. K., Glytsis, E. N., and Brennan, K. F., "Semiconductor electron-wave slab waveguides", J. App. Phys., 66 (3), pp. 1483-1485 (1989).

Gaylord, T. K., and Brennan, K. F.,"Electron Wave Optics in Semiconductors", J. App. Phys., 65 (2), pp. 814-820. (1989).

Ghatak, A. K., Thyagarajan K., and Shenoy, M. R., "Numerical analysis of planar optical waveguides using matrix approach", IEEE J. of Light. Tech., 5 (5), pp. 660-667 (1987).

Glytsis, E. N., Gaylord, T. K., and Brennan, K. F., "Theory and design of semiconductor electron-wave interference filter/emitters", J. App. Phys., **66** (12), pp. 6158-6167 (1989).

Hamada, H., Hiroyama, R., Honda, S., Shono, M., Yodoshi, K., and Ymamguchi, T., "AlInGaP strained multiple-quantum-well visible laser diodes (l<630nm Band)   with a multiquantum barrier grown on misoriented substrates", IEEE J. Quantum Elec., **29** (6), pp. 1844-1850 (1993).

Hanssmann, S., Burkhard, H. , Dalnof, K. , Schlapp, W., Losch, R., Nickel, H., and Hillmer, H., "Design and realization of InGaAs/GaAs strained layer DFB QW lasers". J. Lightwave Tech. **10** (5), pp. 620-624 (1989).

Haug, A., "Theory of the temperature dependence of the threshold current of an InGaAsP laser", J. Quantum Elec., **21** (6), pp. 716-718, (1985).

Hayes, J. R., England, P., and Harbison, J. P.,"Quantum interference effects in GaAs/GaAlAs bulk potential barriers", Appl. Phys. Lett., **52** (19), pp. 1578-1580 (1988).

Hayes, J. R., Patel, D., Adams, A. R., "The temperature dependence of electron and hole mobilities in GaInAsP alloys", J. of Elec. Mat., **11** (1), pp. 155-189 (1982).

Heiblum, M., et al.,"Direct observation of ballistic transport in GaAs", Phys. Rev. Lett., **55** (20), p. 2200-2202 (1985).

Henderson, G. N., Gaylord, T. K., and Glytsis, E. N., "Electromagnetic analogies to general-Hamiltonian effective-mass electron wave propagation in semiconductors with spatially varying effective mass and potential energy", Phys. Rev. B. **45**, pp. 8404-8407 (1992).

Henry, C. H., Logan, R. A., Temkin, H., and Merritt, F. R., "Absorption, emission, and gain spectra of 1.3 μm InGaAsP quaternary lasers", IEEE J. Quan. Elec., **19** (6), p. 941 (1983).

Herpin, M. A., "Calcul du pouvoir reflecteur d'un systeme stratifie quelconque", C. Rend., Acad. Sci., pp. 182-183 (1947).

Hulse, C. A., and Knoeson, A., "Iterative calculation of complex propagation constant of modes in multilayer planar waveguides", IEEE J. Quan. Elec., **28** (12), pp. 2682-2684 (1992).

Hung, K. M., and Wu, G. Y., "Transfer-matrix theory of the energy levels and electron tunneling in heterostructures under an in-plane magnetic field", Phys. Rev. B. **45,** pp. 3461-3464 (1992).

Hutchings, D.C., "Transfer matrix approach to the analysis of an arbitrary quantum well structure in an electric field", Appl. Phys. Lett., **55** (11), pp. 1082-1084, (1989).

Iga, K., Uenohara, H., and Koyama, F., "Electron reflectance of multiquantum barrier (MQB)", Elec. Let., **22** (19), pp. 1008-1009 (1986).

Itaya, K., Hatakoshi, G., Ishikawa, M., Nishikawa, Y., Saito, S., and Okajima, M., "Remarkable improvement in the temperature characteristics of GaAs lasers using an InGaAlP cladding layer", IEEE J. Quan. Elec., **29** (6), pp. 2068-2073 (1993).

Jonsson, B., and Eng, S. T., "Solving the Schrodinger equation in arbitrary quantum-well potential profiles using the transfer matrix method", IEEE J. Quantum Elec., **26** (11), pp. 2025-2035, (1990).

Kishino K., Kikuchi A., Kaneko Y., and Nomura, I., "Enhanced carrier confinement effect by the multiquantum barrier in 660nm GaInP/AlInP visible lasers", Appl. Phys. Lett. **58** (17), pp.1822-1824 (1991).

Kraus, J. and Deimel, P. P., "Calculation of the propagation constant of optical modes in multiquaantum-well structures", IEEE J. Quantum Elec., **26** (5), pp 824-826 (1990).

Krishnamurthy, S., Berding, M. A., Sher, A., and Chen, A. B., "Ballistic transport in semiconductor alloys", J. Appl. Phys., **63** (9), pp. 4540-4547 (1988).

Krishnamurthy, S., Sher, A., and Chen, A. B., "Materials choice for ballistic transport: Group velocities and mean free paths calculated from realistic band structures", Appl. Phys. Lett., **52** (6), pp. 468-470 (1988).

Lee, J., Vassel, M. O., and Jan, G. J., "Energy-band diagrams of p-i-n heterostructures for single quantum-well lasers", IEEE J. Quantum Elec., **29** (6), pp 1469-1497 (1993).

Levi, A., Hayes, J. R., Platzman, P. M., and Weigmann, W., "Injected hot electron transport in GaAs", Phys. Rev. Lett., **55** (19), pp. 2071-2073 (1985).

Lui, W. W., and Fukuma, M., "Exact solution of the Schrodinger equation across an arbitrary one-dimensional piecewise-linear potential barrier", J. Appl. Phys., **60** (5), pp. 1555-1559 (1986).

Maciejko, R., Champagne, A., and Glinski, J., "The performance of double active region InGaAsP lasers", IEEE J. Quan. Elec., **27** (10), pp. 2238-2247 (1991).

Makino, T. M., and Adams, D. M.,"TE- and TM couplding coefficients in multi-quantum well distributed feedback lasers", IEEE Phot. Tech. Lett. 3 (11), pp. 963-965 (1991)

Madelung, O., *Ed.,*Semiconductors: Group IV Elements and III-V Compounds, (Springer-Verlag, New York, 1991).

Martin, O. J. F., Gian-Luca, B., and Wolf, P.,"Thermal behavior of visible AlGaInP-GaInP ridge laser diodes", IEEE J. Quan. Elec., **28** (11), pp. 2582-2588 (1991).

Matsusue, T., and Sakaki, H. "Radiative recombination coefficient of free carriers in GaAs-AlGaAs quantum wells and its dependence on temperature", Appl. Phys. Lett. **50** (20), pp.1429-1431 (1987).

Mendez, E. E., Agullo-Rueda, F. and Hong, J. M., "Temperature dependence of the electronic coherence of GaAs-GaAlAs superlattices", Appl. Phys. Lett., **56** (25), pp. 2545-2547 (1990).

Nelson, D. F., Miller, R. C., and Kleinman, D. A., "Band nonparabolicity effects in semiconductor quantum wells", Phys. Rev. B, **35** (14), pp. 7770-7773 (1987).

O'Reilly, E. P., "Band structure of InP: Overview" (in Properties of Indium Phosphide   (Inspec, New York, 1991, pp. 93-97).

Pankove, J., Optical Processes in Semiconductors, (Dover, New York, 1971).

Potter, R. C., and Lakhani, A. A., "Observation of electron quantum interference effects due to virtual states in a double barrier heterostructure at room temperature", App. Phys. Lett., 52 (16), pp. 1349-1351 (1988).

Rayleigh, Lord, Proc. Royal Soc., **86** A, pp. 207-221, (1912).

Ramadas, R. M., Garmire E., Ghatak A. K., Thyagarajan, K., and Shenoy, M. R., "Analysis of absorbing and leaky planar waveguides: a novel method", Opt. Let. **14** (7), pp. 376-378 (1989).

Rennie, J., Okajima, M., Watanabe, M., and Hatakoshi G, "High temperature (74°C) operation of 634 nm InGaAlP laser ddiodes utilizing a multiple quantum barrier", IEEE J. Quantum Elec., **29** (6), pp 1857-1862 (1993).

Rennie, J, Conference on Light and Electro-Optics, Anaheim, *Proceedings,* paper CMA2, 1992.

Rezek, E. A., Holonyak, N., Vojak, B. A., Stillman, G. E., Rossi, J. A., Keune, D. L., and Fairing, J. D., "LPE InGaPAs (x~0.12, z~0.26) DH laser with multiple thin-layer (<500 Å) active region", Appl. Phys. Lett., **31** (4), pp. 288-290 (1977).

Reggiani, L., *Ed.*, Hot-Electron Transport in Semiconductors,(Springer-Verlag, New York,1985).

Schlereth, K. H., and Tacke M., "The complex propogation constant of multi-layer waveguides: an algorithm for a personal computer", IEEE J. Quantum Elec. **26** (4), pp. 627-630 (1990).

Shono, M., Honda, S., Ikegami, T., Bessyo, Y., Hiroyama, R., Kase H., Yodoshi K., Yamaguchi, T., and Niina, T., "High-power operation of 630nm-band tensile strained MQW AlGaInP laser diodes with a multiquantum barrier", Elec. Lett., **29** (11), pp. 1010-1011 (1993).

Sirtori, C., Capasso, F., Faist, J., Sivco, D., Chu, S., and Cho, A., "Quantum wells with localized states at energies above the barrier height: A Fabry-Perot electron filter", Appl. Phys. Lett., **61** (8), pp. 898-900 (1992).

Sleight, J.W., Dept. of Elec. Eng., Yale University, New Haven, *private communication,* 1993.

Smith, R. E., Houde-Walter, S. N., and Forbes, G. W., "Numerical determination of planar waveguide modes using the analyticity of the dispersion relation", Opt. Let. **16** (17), pp. 1316-1318 (1991).

Sun, L., and Marhic, E, "Numerical study of attenuation in multi-layer nfrared waveguides by the circle-chain convergence method", J. Opt. Soc. Am. A **8** (2), pp. 478-483 (1991).

Sze, S. M.,Physics of Semiconductor Devices, (John Wiley and Sons, New York, 1981).

Takagi, T., Koyama F., and Iga, K.,"Design and phtoluminescence study on a multiquantum barrier", IEEE J. Quantum Elec., **27** (6), pp 1511-1518. (1991)

Takasaki, B. W., Relaxation of optically generated carriers in strained InGaAsP multiple quantum well laser structures, Master's Thesis, McMaster University, Hamilton, 1992.

Takeda, Y., Littlejohn, M. A., and Trew, R. J., "Effects of two longitudinal optical-phonon modes on electron distribution in GaInAsP", Appl. Phys. Lett., **40** (9), pp. 836-838 (1982).

Thijs, P. J. A., Tiemeijer, L. F., Kuindersma, P. I., Binsma, J. J. M., and VanDongen T.,"High performance 1.5µm wavelength InGaAs/InGaAsP strained quantum well lasers and amplifiers", IEEE J. Quant. Elec. 27 (6), pp. 1426-1439 (1991).

Tsubaki, K., and Yasuhiro, T., "Coherence length in quantum interference devices having periodic potential", App. Phys. Lett., 53(10), pp. 859-861 (1988).

Vassel, M. O., "Structure of optical guided modes in planar multilayers of optically anisotropic materials", J. Opt. Soc. Am., 64 (2), pp. 166-170 (1977).

Wang, J., Yuan, S., Gu, B., and Yang, G., "Guided electron waves in coupled deep quantum wells", Phys. Rev. B, 44 (24), p. 13618 (1991).

Wang, S. W., Fundamentals of semiconductor theory and device physics, Prentice Hall, Englewood Cliffs, 1989].

Walpita, L. M., "Solutions for planar optical waveguide equations by selecting zero elements in a characteristic matrix", J. Opt. Soc. Am. A 2, (4), pp. 595-602 (1984).

Yamanishi, M., and Suemunee, I., "Comment on polarization dependent matrix elements in quantum well lasers", Jpn. J. of Appl. Phys., 23 (1), pp. L35-L36 (1980).

Zebda, Y., and Kan'an, A. M., "Resonant tunneling current calculations using the transmission matrix method", J. Appl. Phys., 72 (2), pp. 559-563 (1992).

Zhou, P., Cheng, J., Schaus, C., Sun, S., Zheng, K., Armour, E., Hains, C., Hsin, W., Myers, D., and Vawter, G., "Low series resistance high efficiency GaAs/AlGaAs vertical cavity surface emitting lasers with continuously graded mirrors grown by MOCVD", IEEE Phot. Tech. Lett., 3, pp. 591-593 (1991).

Zory, P. S., *Ed.*, Quantum Well Lasers (Academic Press, New York, 1993).